FINITE ELEMENT ANALYSIS OF ELASTOMERIC BEARINGS UNDER COMPRESSION AND SHEAR LOADING

by

Mert Can Aynur

B.S, Mechanical Engineering, Marmara University, 2016

Submitted to the Institute for Graduate Studies in
Science and Engineering in partial fulfillment of
the requirements for the degree of
Master of Science

Graduate Program in Mechanical Engineering

Boğaziçi University

2020

ACKNOWLEDGEMENTS

I would like to thank my supervisor Assoc. Prof. Şebnem Özüpek for her guidance and support throughout my thesis study. I would also like to thank defense jury members Prof. Ayşe Edinçliler and Assist. Prof. Birkan Tunç for the review of my thesis and recommendations.

Finally, I would like to thank my parents Ferzan and Ünal Aynur, and my brother Atakan Aynur for their love.

ABSTRACT

FINITE ELEMENT ANALYSIS OF ELASTOMERIC BEARINGS UNDER COMPRESSION AND SHEAR LOADING

Elastomeric bearings are widely used as isolators for buildings and bridges. Elastomeric bearings may be either stratified structures with repeated parallel layers of rubber and steel or plain rubber. This thesis focuses on computational approaches to evaluate global and local responses of plain rubber bearings and rubber-steel composite bearings which are subjected to either compression load or combination of compression and shear loads.

During the development of the finite element model, accurate representation of the mechanical behavior of elastomer and steel, and geometric nonlinearities were addressed. Hyperelastic and viscoelastic material models for rubber were constructed using a set of test data available in the literature. The steel was represented with an elastoplastic material model.

Using the developed finite element model, the effects of the rubber viscoelasticity, rubber compressibility and the bearing shape factor on the global response, i.e. vertical force, vertical stiffness, horizontal force, and horizontal stiffness, were studied in static analysis. In addition, the effects of magnitude of the applied load and friction on the local response of the bearing were studied in static analysis. For quasi-static analysis, the effects of the applied loading rate and compressibility of rubber on the predictions were determined. Implicit time integration for static analysis and explicit time integration for quasi-static analysis were used.

The computational approaches presented in this thesis may be applied to the analysis of most isolators for buildings and bridges. Future studies may take into account cyclic shear loads along with compression load.

ÖZET

ELASTOMERİK İZOLATÖRLERİN SONLU ELEMAN ANALİZLERİ

Elastomer mesnetler yaygın olarak bina ve köprülerin deprem yalıtımında kullanılır. Elastomer yalıtıcılar kauçuk ve çelik tabakalarından oluşabileceği gibi yalın kauçuktan da oluşabilir. Bu tezde, sonlu elemanlar yöntemi kullanılarak yalın kauçuk yalıtıcıların ve kauçuk-çelik kompozit yalıtıcıların global ve lokal davranışlarının belirlenmesi çalışılmıştır.

Sonlu elemanlar modeli oluşturulurken, kauçuk ve çeliğin mekanik davranışlarının doğru modellenmesi dikkate alınmış ve doğrusal olmayan geometrik davranışa uygun formülasyon kullanılmıştır. Kauçuk için literatürdeki deney verileri kullanılarak hiperelastik ve viskoelastik malzeme modelleri oluşturulmuştur. Çelik ise elastik-plastik malzeme modeli ile temsil edilmiştir.

Oluşturulan sonlu elemanlar modeli kullanılarak, kauçuk viskoelastisitesi, kauçuk sıkıştırılabilirliği ve şekil faktörünün yalıtıcının global davranışı, örneğin düşey kuvvet, düşey rijitlik, yatay kuvvet, yatay rijitlik, üzerine etkileri statik analizlerle çalışılmıştır. Ek olarak, uygulanan yük miktarı ve sürtünmenin yalıtıcının lokal davranışı üzerine etkileri statik analizlerle çalışılmıştır. Yarı statik analizlerde, yükleme hızı ve kauçuk sıkıştırılabilirliğinin çözümlere etkisi belirlenmiştir. Statik analizler için örtük entegrasyon, yarı statik analizler için belirtik entegrasyon kullanılmıştır.

Bu tezde sunulan hesaplamalı yaklaşımlar çoğu bina ve köprü yalıtıcı analizleri için uygulanabilir. Gelecek çalışmalarda basma yükü ile beraber çevrimsel kayma yükleri de hesaba katılabilir.

TABLE OF CONTENTS

LIST OF FIGURES

LIST OF TABLES

LIST OF SYMBOLS

E	Elastic modulus
E'	Hardening modulus
K_0	Initial bulk modulus
U1	Horizontal displacement
U2	Vertical displacement
RF1	Horizontal reaction force
RF2	Vertical reaction force
SF	Shape factor
ε	Nominal strain
γ	Shear strain
μ	Coefficient of friction
μ_0	Initial shear modulus
λ_2	Stretch in y direction
ν	Poisson's ratio
σ_{avg}	Average compressive stress
σ_{yield}	Yield stress
σ_{11}	Normal stress in x direction
σ_{22}	Normal stress in y direction
σ_{21}	Shear stress in xy plane

LIST OF ACRONYMS / ABBREVIATIONS

2D	Two Dimensional
3D	Three Dimensional
FE	Finite Element
FEA	Finite Element Analysis
HDR	High Damping Rubber
IE	Internal Energy
KE	Kinetic Energy
NR	Natural Rubber

1. INTRODUCTION

Elastomeric bearings are stratified structures with repeated parallel layers of elastically hard and elastically soft materials. The hard material is typically steel and the soft material is natural or synthetic rubber. Plain rubber may also be used as a bearing.

Elastomeric bearings are widely used in civil, mechanical and automotive engineering. As an example, bridge bearings are used under pre-cast concrete beams or steel beams and are designed to handle vertical loading and rotation through vertical deflection. Vibration isolation bearings are used to isolate vibrating machines or buildings in severe acoustic environments. Seismic isolation or base isolation bearings are used to reduce the effects of earthquake in buildings and bridges. Figure 1.1 shows an example of a natural rubber isolator [1].

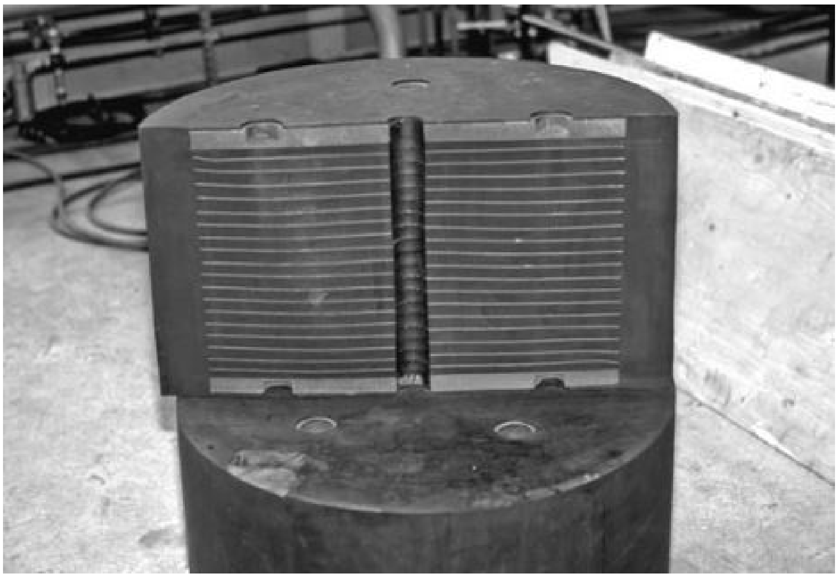

Figure 1.1. A natural rubber isolator [1].

The bearings are usually subjected either to compression or to a combination of compression and shear which is illustrated in Figure 1.2 [2]. In the case of seismic isolation, the steel layers provide large stiffness under vertical load, while the rubber layers provide low horizontal stiffness, when the structure is subjected to lateral loads (e.g., earthquake, wind, etc.).

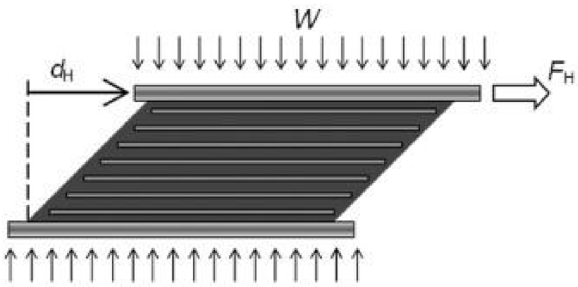

Figure 1.2. Typical deformation produced by seismic actions [2].

1.1. Literature Review

In the study by Amin et. al. [4], an exponential, rate-independent, that is hyperelastic model was proposed to characterize the rubber behavior. The responses of high damping rubber and filled natural rubber under compression and shear loading were studied. Both instantaneous and equilibrium responses were measured and presented in the study. In this thesis, compression and simple shear test data of HDR at instantaneous state were used in order to calibrate elastic response of the base isolation rubber.

In Amin et. al.'s study [5], a rate-dependent, i.e. visco-hyperelasticity model, was developed in order to represent the response of high damping rubber under compression and shear loading. Shape factor and loading rate are two of the parameters examined in the paper. In this thesis, stress relaxation test data of HDR, which is the same material used in [4], were used to calibrate the viscoelastic behavior of rubber.

In the study by Quaglini et. al. [2], an experimental procedure was established to evaluate the behavior of high damping rubber specimens subjected to combination of compression and shear loading. The study calls attention to effects of compression load on mechanical behavior of HDR bearings, for instance, the secant shear modulus increases as compression load increases.

In the study by G. Milani and F. Milani [6], the exponential models proposed in [4, 7] and nine-constant Mooney-Rivlin model were used to represent the response of different rubber compounds. The predictions for compression and shear loading were compared to experimental results.

J.M. Kelly and D.A. Konstantinidis [1] highlighted that compressibility of rubber plays a crucial role in the mechanical behavior of base isolation systems. It was also determined that for the bearing subjected to shear loading, bending moment is created at the top and bottom of the isolation system. This bending moment, in turn, leads to shear strains in rubber pads. In addition, friction between the unbonded bearing and its supports above and below, notably influences the compression stiffness and the pressure distribution.

In the study by Yurdabak [8], static analysis with implicit integration and quasi-static analysis with explicit integration were performed to study compression of rubber discs with different shape factors and compressibility values. 2D axisymmetric models were analyzed via ABAQUS/Standard and ABAQUS/Explicit. Compressive stiffness, total load and bulge strain values were calculated and results obtained from static and quasi-static analyses were compared. In this thesis, the study provides a basis for quasi-static analysis with explicit integration.

In the study by Hamzeh et. al. [9], elastomeric bridge bearings were numerically analyzed taking geometric nonlinearities, material nonlinearities and frictional interface properties into account. Yeoh's strain energy function was used to model the rubber pads. The study stated that in bearings subjected to compression rubber pads tend to bulge outward which is reduced by the presence of steel shims; as a result, compressive stiffness of pads increases. In addition, when the pads are horizontally displaced, reduction in shear stiffness is observed.

Salomón et. al. [10] constituted a FE formulation which models elastomers for base isolation considering viscoelastic behavior. The study points out that modeling elastomers as viscoelastic is necessary when the loads are quasi-static or dynamic.

In Gajewski et. al.'s study [11], FEA of bridge bearings under compression and shear loading were conducted using ABAQUS/Standard for different hyperelastic material models, such as Yeoh and Neo-Hookean. It is concluded that results differed considerably between 3D analysis and 2D plane strain analysis when the loading was compression, while results showed good agreement when the loading was shear.

H.H. Nguyen and J.L. Tassoulas [12] studied effects of shear loading direction on bridge bearings by performing 3D analysis of rectangular and square bearings via ABAQUS. Frictional contact was defined between bearing and rigid supports. It is concluded that rubber strains decrease when the shear load is applied along the direction of short side of rectangular bearings.

In the study by Kalfas et. al. [13], 3D FEA of elastomeric bearings under various combinations of vertical and cyclic shear loads were performed in order to study tensile stress developments within the rubber using ABAQUS. It is deduced that the presence of shear strain and free or restricted rotation boundary conditions affect the development of tensile stresses.

1.2. Objectives of the Thesis

Finite element modeling of plain elastomer bearings and of composite bearings with steel layers is constructed in this thesis. Accurate representation of the mechanical behavior of elastomer and steel, and geometric nonlinearities are addressed during the development of the finite element model.

The thesis focused on the static analysis with implicit time integration and quasi-static analysis with explicit time integration. Using the developed finite element model, the effect of the following parameters on the bearing mechanical response were studied:

- Constitutive model of rubber
- Compressibility of rubber
- Shape factor of the bearing
- Magnitude of the applied load
- Rate of the applied load
- Friction

The FE model is developed and analyzed in commercial general purpose finite element software ABAQUS/Standard and ABAQUS/Explicit [3].

This thesis focuses on computational approaches to evaluate global and local responses of plain rubber bearings and rubber-steel composite bearings. This study is not limited to hyperelastic constitutive model, as it is the case in most of the work in the literature, but also accounts for the viscoelastic behavior of rubber. In addition, in the thesis explicit time integration was explored for global response analysis of bearings. In order to highlight the importance of rubber compressibility for explicit time integration, different levels of rubber compressibility were evaluated. Formerly, compressive response of a rubber disc was investigated with implicit and explicit time integrations in [8]. This study investigated not only compressive response but also shear response of a rubber layer with implicit and explicit time integration.

Organization of the remainder of the thesis is as follows: Background information about large deformation analysis, hyperelasticity, viscoelasticity, shape factor, compressibility of rubber, and comparison of implicit and explicit time integration are presented in Chapter 2. Finite element analysis of a plain rubber bearing by employing hyperelastic model and viscoelastic model are discussed in Chapter 3 and in Chapter 4, respectively. Chapter 5 focuses on finite element analysis of composite bearing model. Summary and conclusions are presented in Chapter 6.

2. THEORY

2.1. Basic Quantities in Large Deformation Analysis

2.1.1. Kinematics

Elastomers are mostly subjected to large deformations. In this section, the fundamental quantities in finite deformation analysis are summarized.

The deformation gradient **F** relates undeformed, $d\mathbf{X}$, and deformed, $d\mathbf{x}$, configurations of a material line. The deformation gradient is given as:

$$\mathbf{F} = \frac{\partial \mathbf{x}}{\partial \mathbf{X}} = \begin{bmatrix} \dfrac{\partial x_1}{\partial X_1} & \dfrac{\partial x_1}{\partial X_2} & \dfrac{\partial x_1}{\partial X_3} \\ \dfrac{\partial x_2}{\partial X_1} & \dfrac{\partial x_2}{\partial X_2} & \dfrac{\partial x_2}{\partial X_3} \\ \dfrac{\partial x_3}{\partial X_1} & \dfrac{\partial x_3}{\partial X_2} & \dfrac{\partial x_3}{\partial X_3} \end{bmatrix} \tag{2.1}$$

Right Cauchy-Green deformation tensor, which is the most commonly used among various ways to measure the geometric changes in the continuous medium, is defined as:

$$\mathbf{C} = \mathbf{F}^T\mathbf{F} \tag{2.2}$$

Nonlinear, isotropic and elastic response of solids may be derived from a strain energy function which is defined in terms of invariants of **C**:

$$I_1 = tr\mathbf{C} \tag{2.3}$$

$$I_2 = \frac{1}{2}\left[(tr\mathbf{C})^2 - tr\mathbf{C}^2\right] \tag{2.4}$$

$$I_3 = J^2 = det\mathbf{C} \tag{2.5}$$

where J is the volume change ratio. Distortional part of **C** is defined as:

$$\bar{\mathbf{C}} = J^{-2/3}\mathbf{C} \tag{2.6}$$

The invariants of volume preserving part of the deformation is defined as:

$$\bar{I}_1 = J^{-2/3}I_1 \tag{2.7}$$

$$\bar{I}_2 = J^{-4/3}I_2 \tag{2.8}$$

$$\bar{I}_3 = 1 \tag{2.9}$$

In this study, the test data and model predictions are presented in terms of principal stretch ratios, λ_i, which is the ratio of the deformed length to the undeformed length and is shown as:

$$\lambda = \frac{dl}{dL} = \sqrt{\frac{d\mathbf{x}^T \cdot d\mathbf{x}}{d\mathbf{X}^T \cdot d\mathbf{X}}} \tag{2.10}$$

In addition, shear strain, γ, which is the ratio of the horizontal displacement, u_x, to the thickness is shown in Figure 2.1 [9].

$$\gamma = \frac{u_x}{T} \tag{2.11}$$

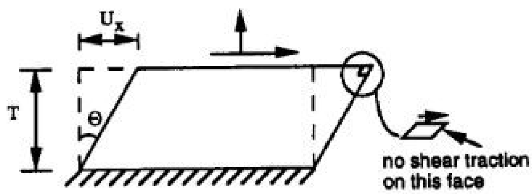

Figure 2.1. Block of elastomers under simple shear (Dotted lines represent original configuration) [9].

2.1.2. Stress Measures

There are three stress measures in finite deformation theory. The Cauchy stress, or true stress, $\boldsymbol{\sigma}$, is defined as force per unit deformed area. The First Piola-Kirchhoff stress, **T**, is defined as force per unit undeformed area, and is often referred to as engineering stress. Although First Piola-Kirchhoff stress is physically motivated, it is unsymmetric. The second Piola-Kirchhoff stress, **S**, is derived from the First Piola-Kirchhoff stress and is symmetric. The three stress measures are related as:

$$\mathbf{T} = J\boldsymbol{\sigma}\mathbf{F}^{-T} \tag{2.12}$$

$$\boldsymbol{\sigma} = \frac{1}{J}\mathbf{F}\mathbf{S}\mathbf{F}^{T} \tag{2.13}$$

2.2. Hyperelasticity

For a hyperelastic material model, the relationship between stress and strain is obtained from a strain energy density potential. In particular, in terms of **S:**

$$\mathbf{S} = 2\frac{\partial W}{\partial \mathbf{C}} \tag{2.14}$$

Several strain energy functions are available in the literature. In this thesis, Yeoh's strain energy function [14] is used. For compressible elastomers, Yeoh's strain energy function is given as the following:

$$W = \sum_{i=1}^{3} C_{i0}\,(\bar{I}_1 - 3)^i + \sum_{i=1}^{3} \frac{1}{D_i}(J - 1)^{2i} \tag{2.15}$$

where C_{i0} and D_i are the material parameters. The relation between the parameters and initial bulk and shear modulus are defined as:

$$K_0 = \frac{2}{D_1} \tag{2.16}$$

$$\mu_0 = 2C_{10} \tag{2.17}$$

For incompressible elastomers, the function becomes as the following:

$$W = \sum_{i=1}^{3} C_{i0} \, (I_1 - 3)^i \tag{2.18}$$

2.3. Viscoelasticity

Rate-dependent representation of the behavior of elastomers requires nonlinear viscoelastic material model. The viscoelastic material property may be defined by shear and bulk relaxation functions in Prony series form:

$$G(t) = G_\infty + \sum_{i=1}^{m} G_i e^{-t/\tau_i} \tag{2.19}$$

$$K(t) = K_\infty + \sum_{i=1}^{m} K_i e^{-t/\tau_i} \tag{2.20}$$

where G_∞ and K_∞ are the equilibrium shear and bulk moduli, respectively. G_i and K_i are Prony coefficients, and τ_i are relaxation times.

The dimensionless forms of relaxation functions used in ABAQUS are defined with respect to G_0 and K_0 which are the instantaneous shear and bulk moduli, respectively.

$$g(t) = \frac{G(t)}{G_0} \tag{2.21}$$

$$k(t) = \frac{K(t)}{K_0} \tag{2.22}$$

2.4. Shape Factor

Shape factor is a design parameter used for elastomeric bearings and is classified as the first and the second shape factor. The ratio of the loaded area over the force-free area of a rubber layer is the first shape factor. The ratio of the effective width over the total thickness of rubber pads in bearings is the second shape factor [15,16]. In this thesis, the focus is on the first shape factor, SF.

There are some differences between building isolation and bridge bearing requirements. Building bearings are typically circular in shape, while bridge bearings are rectangular in shape [17]. In this thesis, rectangular rubber pads with different SF are examined due to available experimental data. For this geometry, the first shape factor becomes:

$$SF = \frac{\mathrm{BL}}{2(\mathrm{B}+\mathrm{L})t} \tag{2.23}$$

where B and L are the side lengths and t is the thickness of the rubber pad shown in Figure 2.2 [18].

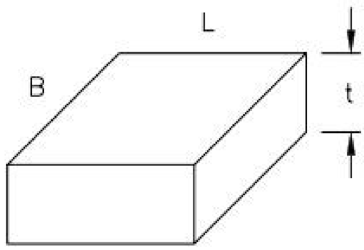

Figure 2.2. Dimensions of a single rubber layer [18].

2.5. Compressibility of Rubber

Elastomers mostly behave as incompressible or nearly incompressible. The ratio of the initial bulk modulus to the initial shear modulus, K_0/μ_0 , is a measure of compressibility. The initial Poisson's ratio may be obtained from the following equation.

$$\nu = \frac{3K_0/\mu_0 - 2}{6K_0/\mu_0 + 2} \tag{2.24}$$

The different compressibility and the corresponding Poisson's ratio values are given in Table 2.1.

Table 2.1. The relation between compressibility and Poisson's ratio.

K_0/μ_0	ν
10	0.452
20	0.475
50	0.490
100	0.495
2000	0.49975
∞	0.5

Compressibility of elastomer substantially influences the procedures for implicit and especially for explicit integration because the minimum time increment approaches zero as the incompressibility increases. In ABAQUS, the recommended maximum limit for the ratio of the initial bulk modulus to initial shear modulus is 100 for analyses with explicit time integration [3].

2.6. Comparison of Implicit and Explicit Time Integration

Simulations can be performed using implicit or explicit time integration in FEA. Depending on problem types, selection between these integration techniques can be done. In general, implicit time integration and explicit time integration are used for static and dynamic analysis, respectively.

In implicit time integration process, there is equilibrium check meaning that analysis is completed when the predetermined tolerance based on the equilibrium of the system is obtained. Throughout that process, a large number of non-diagonal matrix inversions are encountered, so the duration of the prediction exponentially increases with increasing in degrees of freedom of the model and with existing of nonlinear material properties, incompressibility, large deformations, and contact properties. In explicit time integration process, there is no equilibrium check and there is no need of calculating the stiffness matrix. The diagonal mass matrix inversion is required. The analysis time increases linearly with increasing number of degrees of freedom of the model. The comparison between implicit and explicit time integration considering the cost per number of degrees of freedom is presented in Figure 2.3 [3].

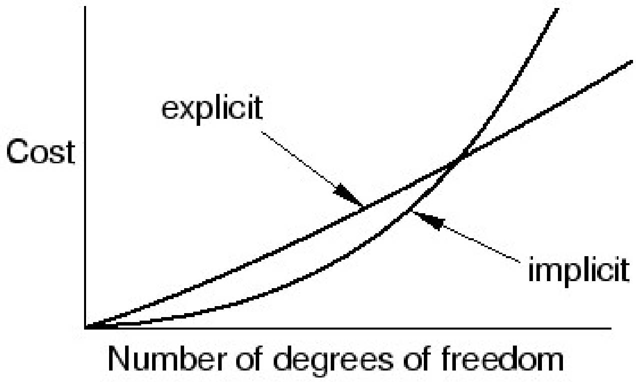

Figure 2.3. The cost per number of degrees of freedom for implicit and explicit time integration techniques [3].

3. FINITE ELEMENT ANALYSIS OF AN ELASTOMER BEARING

Finite element model of a plain elastomer bearing is presented in this chapter. The response of the bearing for either compression load or combination of compression and shear loads was studied. The effects of shape factor and compressibility on vertical and horizontal response of the bearing were investigated in static analysis with implicit time integration. In addition, quasi-static analysis with explicit time integration, and dynamic analysis with implicit time integration were explored. For the explicit analysis, the effect of loading velocity on the predictions was determined.

3.1. Finite Element Model

In this section, material model, geometry, loading and boundary conditions, mesh properties of the finite element model are presented.

3.1.1. Material Model

The elastomer was considered to be HDR (high damping rubber) which is widely used for base isolation. Energy dissipation is an important design parameter for base isolation systems under large shear displacements. The use of fillers in HDR such as extra fine carbon black and oils increases energy dissipation [19]; therefore, HDR provides better damping capabilities than NR (natural rubber).

The experimental data for rubber was taken from the literature [4]. The available data consisted of stress-strain relations for uniaxial compression and simple shear. Both instantaneous and equilibrium curves for HDR were available. In the thesis, the elastomer was represented as hyperelastic considering the instantaneous response. Yeoh form of strain energy function was selected. Yeoh form was preferred since it allows reasonable representation of various deformation states based on uniaxial tension or compression state only. The Yeoh coefficients were obtained in Abaqus using uniaxial compression data. The experimental data and the resulting curve fit for uniaxial compression are shown in Figure 3.1.

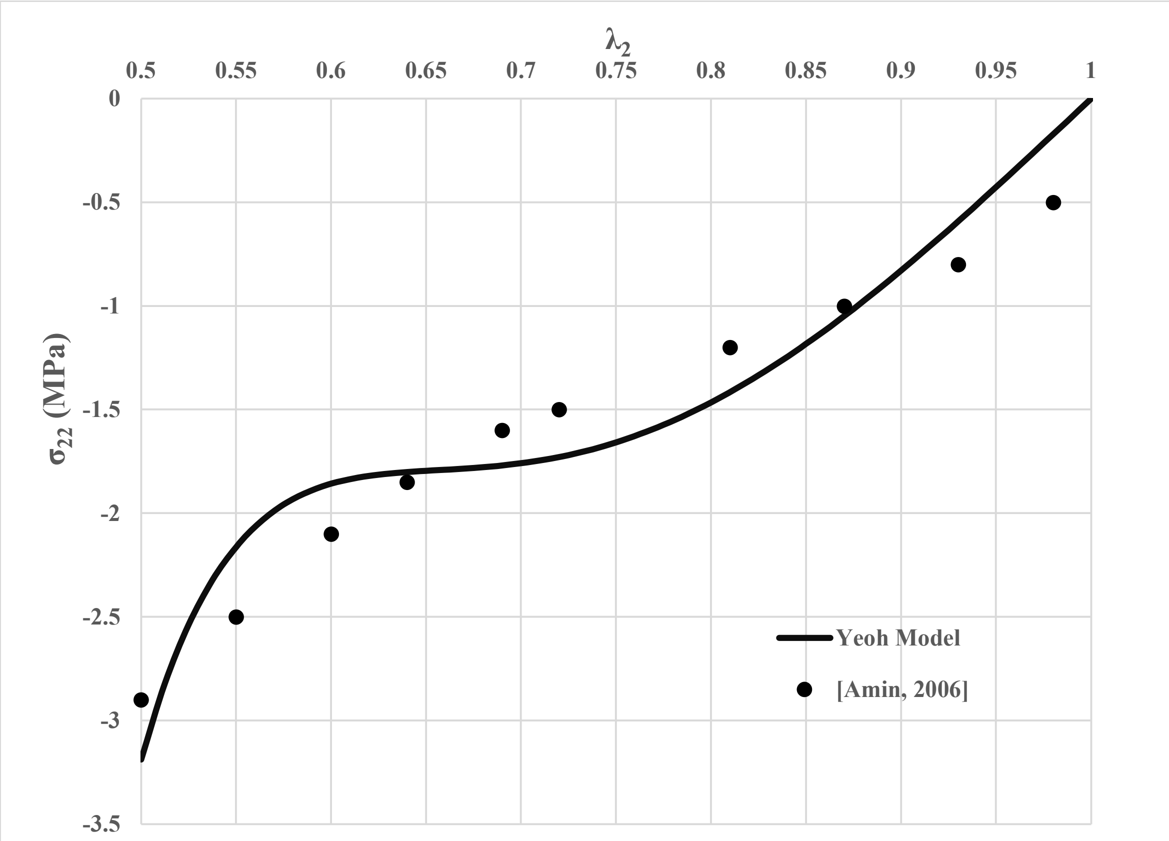

Figure 3.1. Stress-Stretch response for uniaxial compression loading (test data [4]).

The material response under simple shear loading as predicted by Abaqus is presented in Figure 3.2 along with the test data. Note that only uniaxial compression data was used in calibrating Yeoh model. The good fit in simple shear is a proof of why this particular strain energy form was selected.

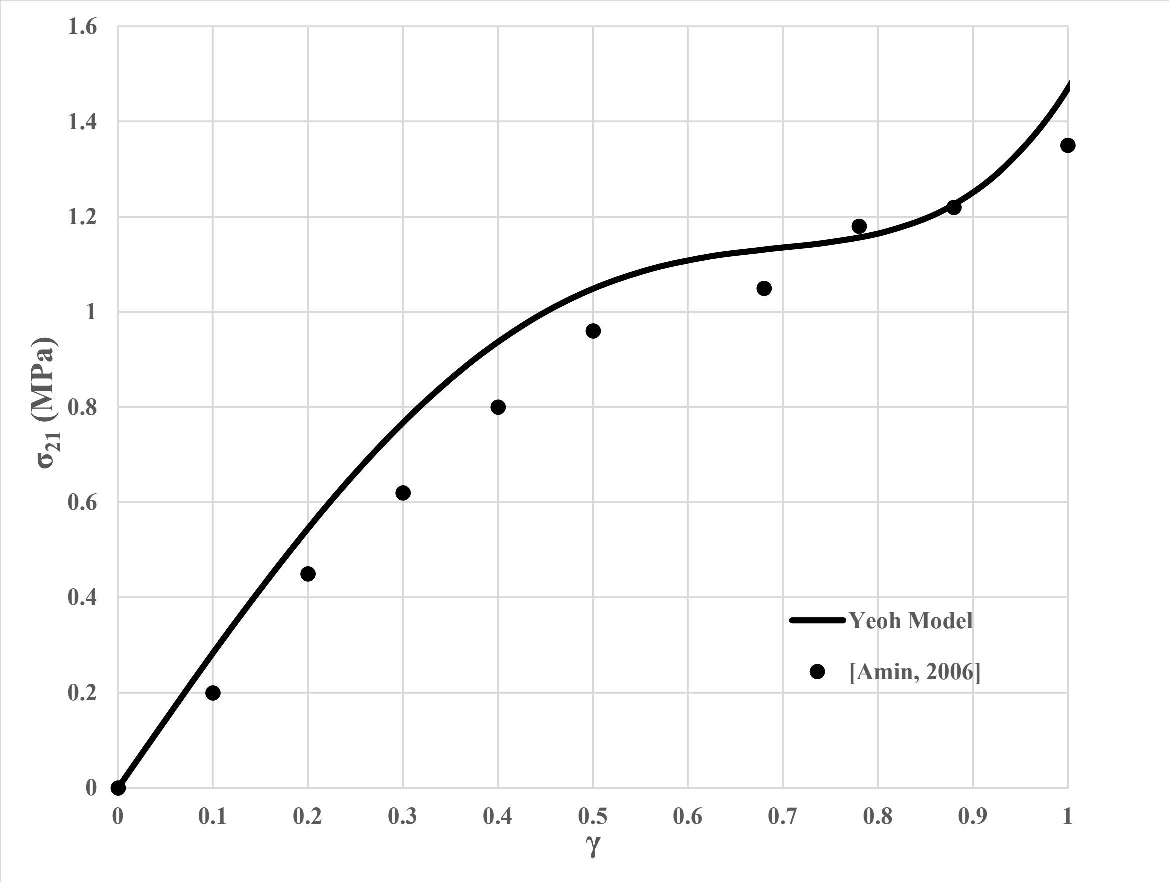

Figure 3.2. Stress-Strain response for simple shear loading (test data [4]).

To evaluate the effect of compressibility, the coefficients C_{i0} (Equation 2.14) were kept constant, while bulk modulus was varied. The ratio of initial bulk modulus to initial shear modulus, which were used in this thesis, are given in Table 3.1. The initial shear modulus is $\mu_0 = 2C_{10} = 2.87\ MPa$.

Table 3.1. The Yeoh coefficients.

K_0/μ_0	ν_0	D_1 (1/MPa)	C_{10} (MPa)	C_{20} (MPa)	C_{30} (MPa)
10	0.452	0.06976	1.433477	-0.910061	0.373833
20	0.475	0.03488			
50	0.490	0.01395			
100	0.495	0.006976			
2000	0.49975	0.0003488			
∞	0.5	0			

For explicit analyses, the rubber density was taken as $1\ g/cm^3$.

3.1.2. Geometry of the Problem

Small-scale rectangular bearings with shape factors of 1, 5, and 12.5 were selected. To assess mechanical response of HDR, small-scale specimens were used in [4] from which experimental test data was taken to calibrate the for rubber material model used in this thesis. Also, the experimental study [2] showed applicability of small-scale specimens for seismic performance evaluations. The side dimensions of rectangular bearings were kept constant as 50x50 mmxmm. The thickness of bearings was adjusted as per the shape factor. Figures 3.3, 3.4, and 3.5 illustrate the geometries of rectangular bearings for shape factors 1, 5 and 12.5, respectively.

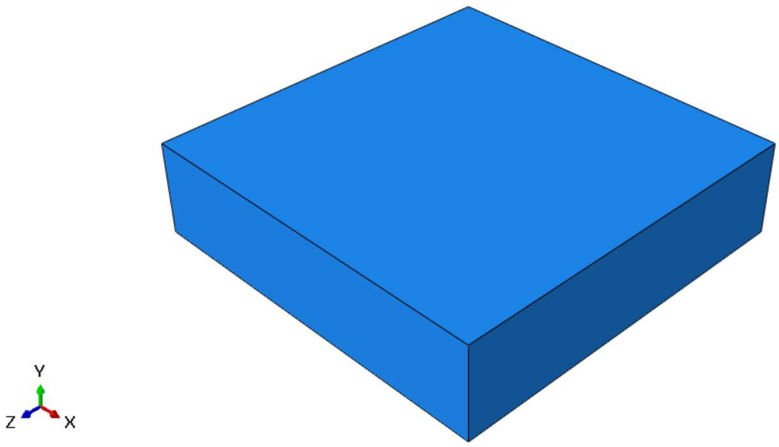

Figure 3.3. The geometry of the bearing with SF=1 (12.5x50x50 mmxmmxmm).

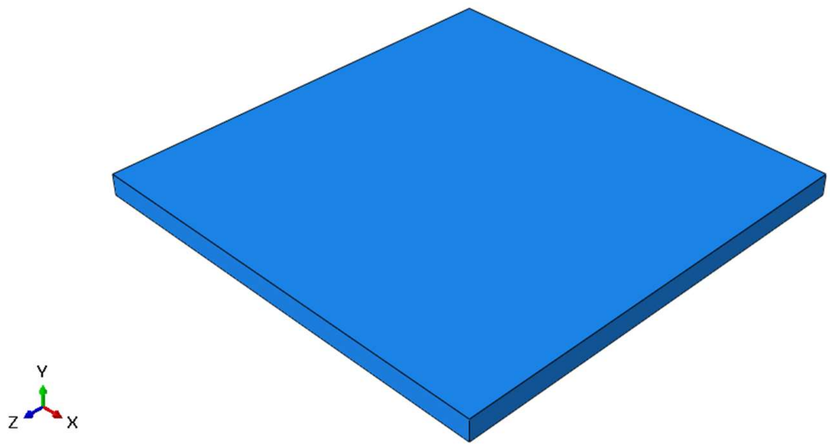

Figure 3.4. The geometry of the bearing with SF=5 (2.5x50x50 mmxmmxmm).

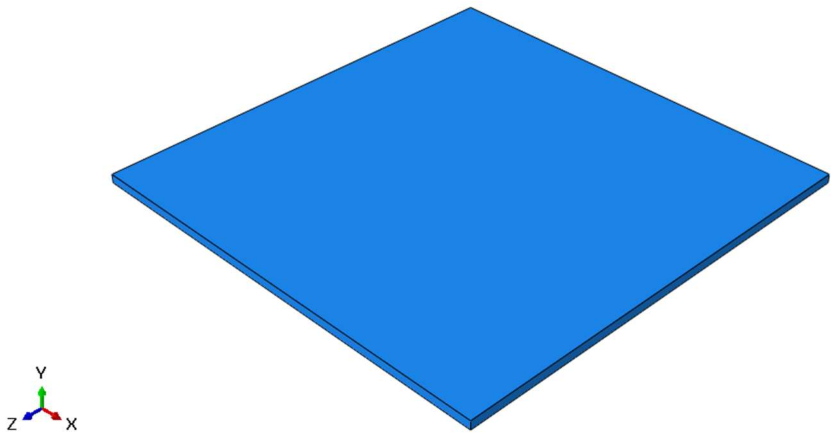

Figure 3.5. The geometry of the bearing with SF=12.5 (1x50x50 mmxmmxmm).

3.1.3. Mesh

Plane strain analysis of the bearings was conducted. Mesh consisted of quadrilateral, reduced integration, linear elements for static analyses with implicit integration and quasi-static analyses with explicit integration. For dynamic analyses with implicit integration, full integration elements were used. Linear elements were used since they are more efficient in contact. Hybrid elements were considered for static and dynamic analyses with implicit integration. In summary, the elements used for predictions are the followings:

- CPE4RH for static analysis with implicit time integration
- CPE4R for quasi-static analysis with explicit time integration
- CPE4H for dynamic analysis with implicit time integration

The mesh structure for each shape factor is shown in Figures 3.6, 3.7, and 3.8. The mesh convergence study is presented in Appendix-A.

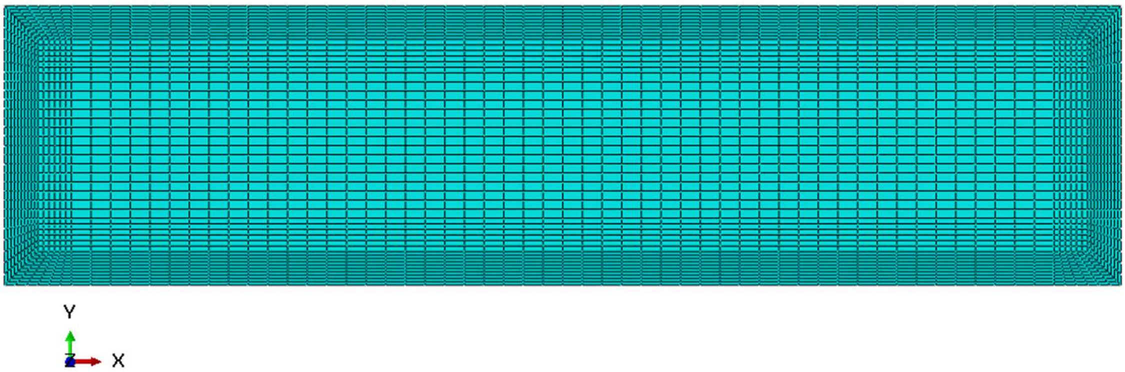

Figure 3.6. The mesh for SF=1. Total number of elements: 3536.

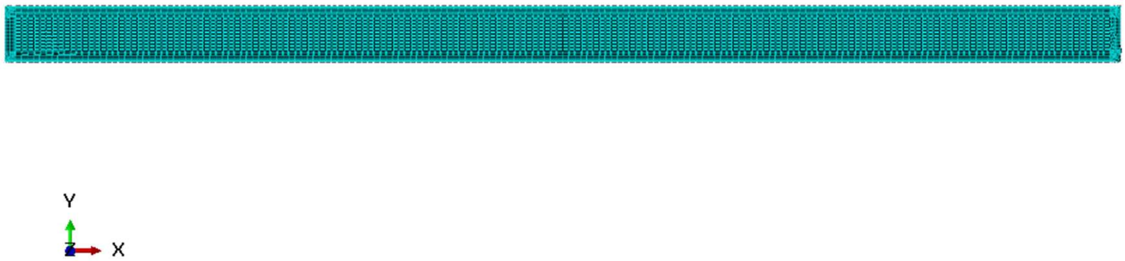

Figure 3.7. The mesh for SF=5. Total number of elements: 6792.

Figure 3.8. The mesh for SF=12.5. Total number of elements: 4096.

3.1.4. Loading and Boundary Conditions

Bearings were subjected to either compression load or combination of compression and shear loads. The loads were applied through an analytical rigid body as displacement.

The compression load was determined according to [15]. In there, one of the allowable compression stresses is 12 MPa. For the geometry used in this study, this corresponds to total load of 30000 N. Table 3.2 shows the vertical displacement corresponding to different shape factors and bulk modulus to shear modulus ratio.

Table 3.2. Total load and the corresponding vertical displacements in the FE models of the bearings.

SF	K_0/μ_0	Total Load (N)	Vertical Displacement (mm)
1	∞	30000	-1.9918
5	10	30000	-0.9255
	20	30000	-0.5343
	50	30000	-0.2549
	100	30000	-0.1503
	∞	30000	-0.0355
12.5	10	30000	-0.3633
	20	30000	-0.2015
	50	30000	-0.0886
	100	30000	-0.0471
	∞	30000	-0.0017

The shear load was also selected according to the same standard [15] referred for compression load. In the standard, the required shear strain is equal to 1. The applied horizontal displacement for each shape factor is shown in Table 3.3. The loads were applied through a rigid body at top surface of the bearing.

Table 3.3. Shear strain and horizontal displacements.

SF	Shear Strain	Horizontal Displacement (mm)
1	1	12.5
5	1	2.5
12.5	1	1

The boundary conditions were defined through reference points of the two rigid bodies as shown in Figure 3.9. For both compression and shear, all displacement components were set to zero at “RP_1”. For compression, horizontal displacement component was set to zero at “RP_2” while for shear vertical displacement component was set to zero at “RP_2.

Vertical and horizontal displacements were applied at “RP_2” for compression and shear, respectively.

Figure 3.9. The boundary conditions for the elastomer bearing

Tie constraint was applied between top and bottom surfaces, and rigid bodies in order to model bearings as bounded. Contact was defined between side surfaces and rigid bodies. For normal behavior, hard contact was defined. For implicit analysis, the constraint was enforced via Augmented Lagrange Method, while for the explicit analyses only, kinematic constraint enforcement method was employed. Tangential behavior was defined as frictionless.

3.2. Results

The finite element predictions were evaluated for the following quantities: vertical force, vertical stiffness, horizontal force and horizontal stiffness. Vertical stiffness is defined as the ratio of the vertical load to the vertical displacement. Horizontal stiffness is defined as the ratio of the horizontal load to the horizontal displacement.

For static analysis with implicit time integration, the effects of the following parameters on the response were investigated:

- Shape Factor
- Compressibility

For quasi-static analysis with explicit time integration and dynamic analysis with implicit time integration, the effects of following parameters on the response were investigated:

- Compressibility
- Loading Velocity

3.2.1. Results for Compressive Loading

The results presented in this section are for the bearings subjected to compression load only. The analyses were conducted with implicit and explicit time integrations.

3.2.1.1. Effect of Shape Factor and Compressibility. For an incompressible material model, the vertical force and vertical displacement predictions for different shape factors are shown in Figure 3.10. The figure highlights that for the same axial load, axial displacement decreases as the shape factor gets larger. The latter is equivalent to increased confinement. Therefore, bearings with higher shape factors have higher vertical stiffness.

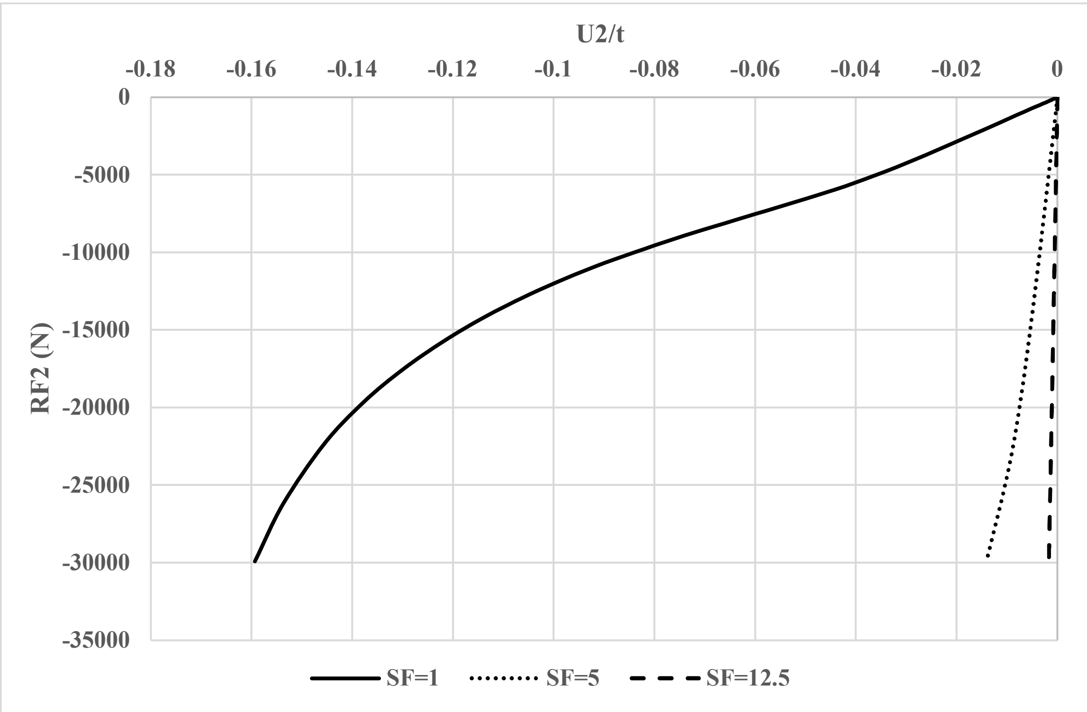

Figure 3.10. The static results for vertical force for the different shape factors for incompressible case.

The vertical stiffness for various shape factors is shown in Figures 3.11 and 3.12 for incompressible case and $K_0/\mu_0 = 20$, respectively. The stiffness values were normalized with respect to SF=12.5 result. It is concluded that vertical stiffness is strongly affected by the compressibility. For $K_0/\mu_0 = 20$, there seems to be a linear relation between vertical stiffness and shape factor, while for incompressible case the relation is exponential.

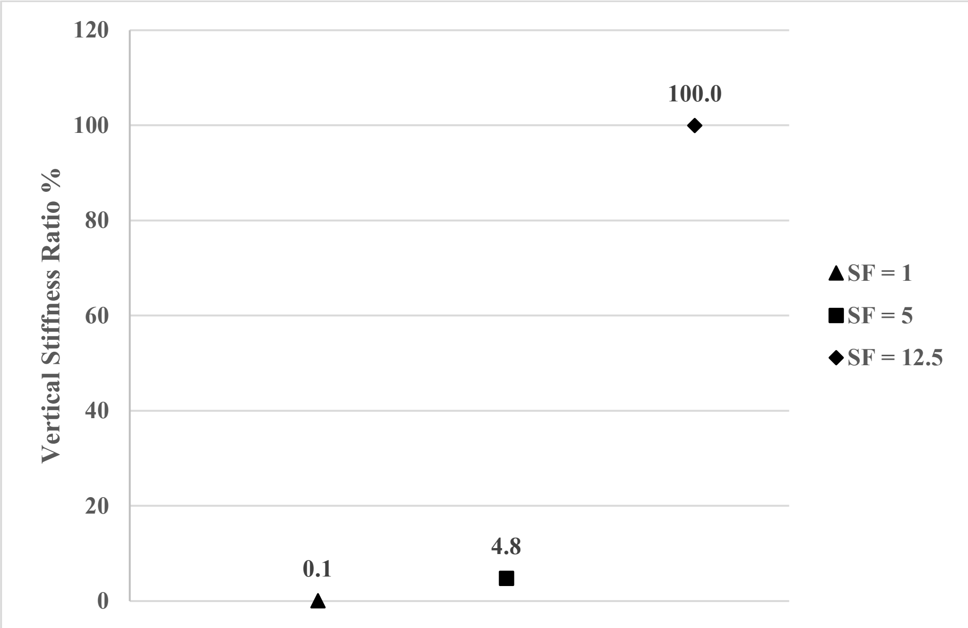

Figure 3.11. The static results for incompressible case where vertical stiffness ratio is normalized with respect to the case of SF=12.5.

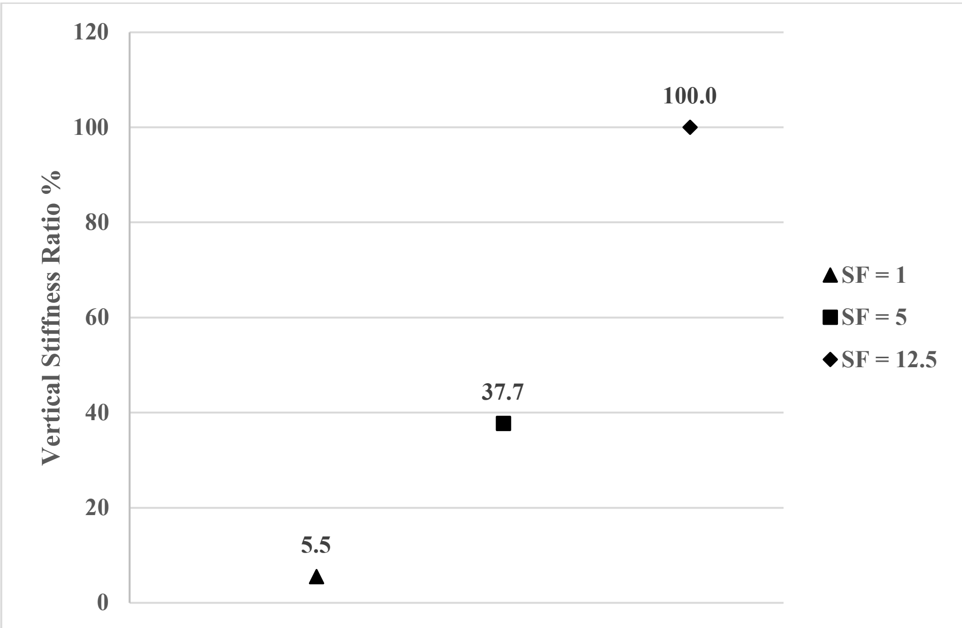

Figure 3.12. The static results for $K_0/\mu_0 = 20$ where vertical stiffness ratio is normalized with respect to the case of SF=12.5.

The vertical stiffness of a bearing with shape factor of 5 and 12.5 was evaluated for various bulk to shear stiffness ratios. The results shown in Figure 3.13 and Figure 3.14 were normalized by the value of the incompressible case of the corresponding shape factor. It is observed that the use of $K_0/\mu_0 \leq 100$ will result in significant error in the predictions of the vertical stiffness as compared to the solution for an incompressible material behavior. Moreover, this error increases as shape factor increases from SF=5 to SF=12.5.

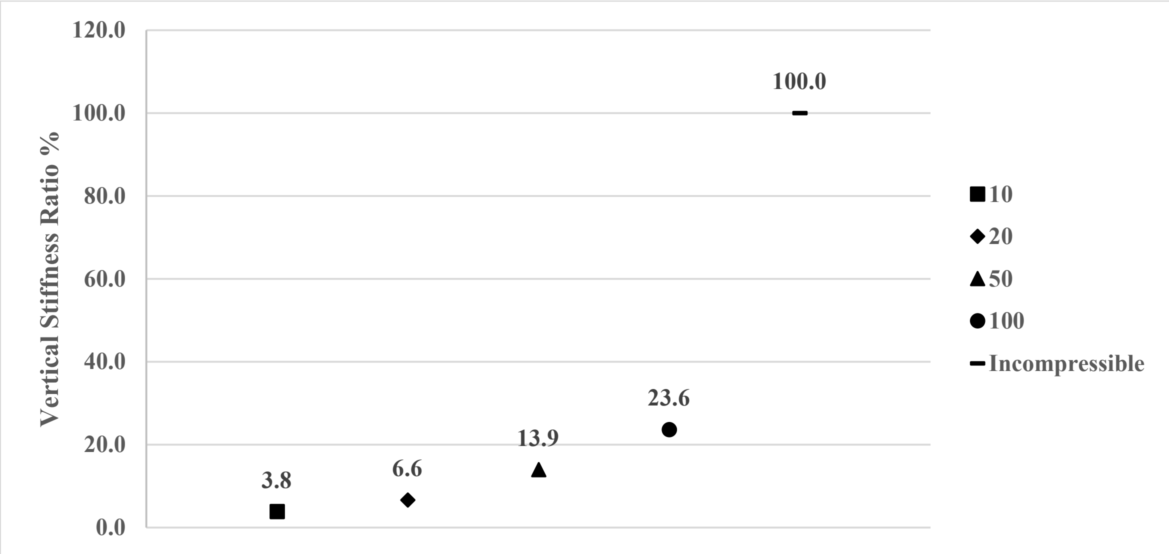

Figure 3.13. The static results for vertical stiffness ratio normalized with respect to the incompressible case for the different compressibility values for SF=5.

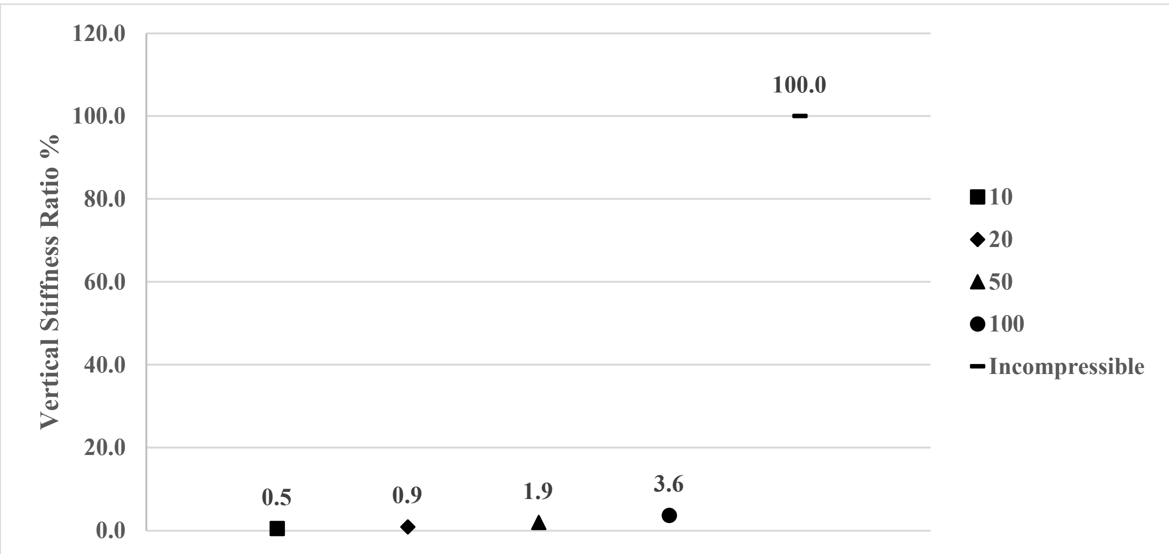

Figure 3.14. The static results for vertical stiffness ratio normalized with respect to the incompressible case for the different compressibility values for SF=12.5.

3.2.1.2. Explicit Time Integration. Quasi-static analyses with explicit time integration were performed to evaluate the effects of the loading rate and compressibility on the vertical force and vertical displacement response of a bearing with shape factor of 5. The strain rates of 0.4/s and 2/s refers to frequencies of 0.1 Hz and 0.5 Hz, respectively. These frequencies are defined as reference values in [17].

Negligible inertial effects should be observed in the results of quasi-static analysis with explicit time integration. One of the quantities that may be investigated for this effect is the ratio of the KE to the IE. Table 3.4 shows the KE/IE ratios for the different velocities and compressibility values. From the table, it is observed that for a given loading rate, a decreasing KE/IE ratio is obtained with increasing compressibility. Also, for a given compressibility, KE/IE decreases with decreasing loading rate.

Table 3.4. KE/IE for the model subjected to compression load.

Strain Rate	$\boldsymbol{K_0/\mu_0}$	**Duration (s)**	**KE/IE %**
2/s	10	0.185	0.9
	20	0.107	2.3
	50	0.051	9.5
	100	0.030	18
0.4/s	10	0.926	0.04
	20	0.534	0.09
	50	0.255	0.45
	100	0.150	1.71

Figures 3.15 and 3.16 show vertical force and vertical displacement response of the model with shape factor of 5 for $K_0/\mu_0 = 100$ and $K_0/\mu_0 = 20$.

As presented in Figure 3.15, quasi-static solution for strain rate of 0.4/s overlaps with static solution. Quasi-static analysis with explicit time integration at higher strain rate (2/s) deviates from static solution with implicit time integration, e.g. at -0.1 mm displacement the deviation is roughly 20%.

Figure 3.16 ($K_0/\mu_0 = 20$) indicates that quasi-static solution for both strain rates of 0.4/s and 2/s overlaps with static solution. In consideration of Figure 3.15 ($K_0/\mu_0 = 100$), it is concluded that as compressibility increases quasi-static solutions for a given loading velocity become closer to static solutions.

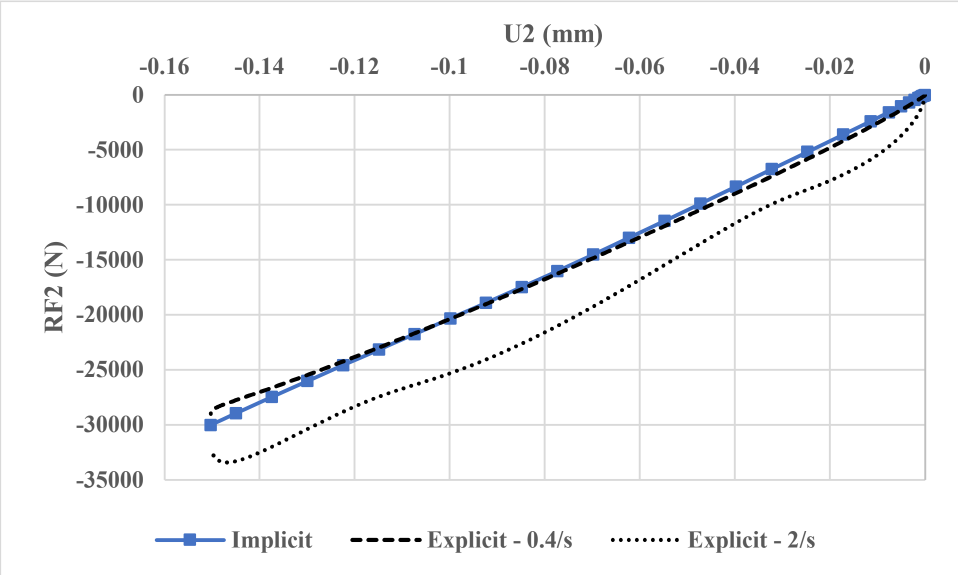

Figure 3.15. The static and quasi-static results for vertical force for the different velocities for $K_0/\mu_0 = 100$.

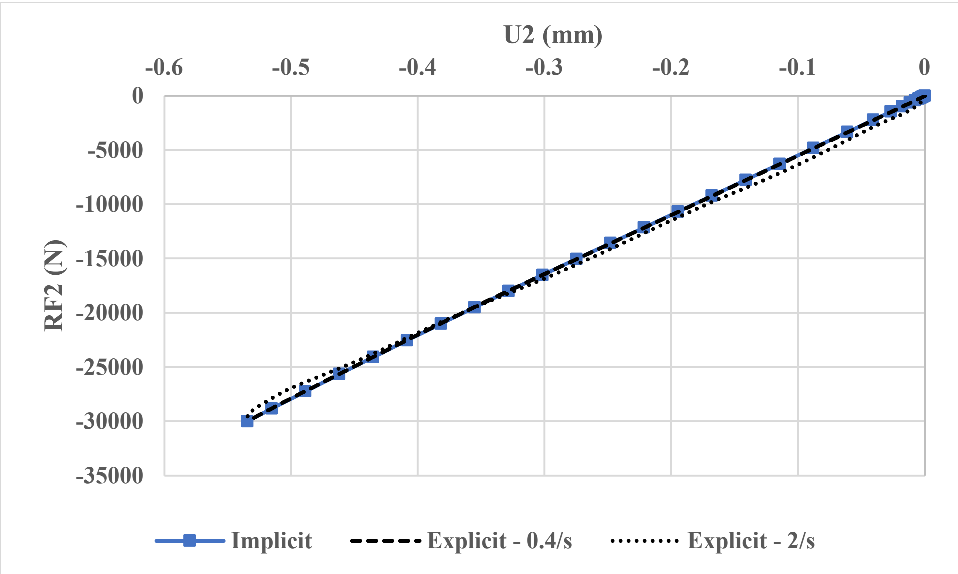

Figure 3.16. The static and quasi-static results for vertical force for the different velocities for $K_0/\mu_0 = 20$.

The following are concluded based on the compressive loading results presented in Section 3.2.1.

- Vertical stiffness increases as shape factor (confinement) increases.
- The shape factor effect on vertical stiffness decreases as compressibility increases.
- The use of lower K_0/μ_0 for rubber results in significant error in the predictions of the vertical stiffness as compared to the solution for an incompressible material behavior. This error increases with increasing shape factor.
- For $K_0/\mu_0 = 20$, there seems to be linear relation between vertical stiffness and shape factor, while for incompressible case the relation is exponential.
- In quasi-static analysis with explicit time integration, KE/IE values decrease as compressibility increases and/or loading velocity decreases.
- Results of quasi-static analysis at higher strain rate (2/s) mildly deviates from static solution with implicit time integration.
- For a given loading velocity, results of quasi-static analysis become closer to static solutions as compressibility increases.

3.2.2. Results for Combined Compressive and Shear Loading

The results presented in this section are for the bearings subjected to combination of compression and shear loads. The analyses were conducted with implicit and explicit time integrations.

3.2.2.1. Effect of Shape Factor and Compressibility. For an incompressible material model, the horizontal force and shear strain predictions for different shape factors are shown in Figure 3.17. The figure shows that for shear strain up to 0.5, almost the same horizontal force response is observed for all shape factors. However, for shear strain greater than 0.5, higher horizontal force is observed as shape factor becomes smaller meaning as confinement is decreased.

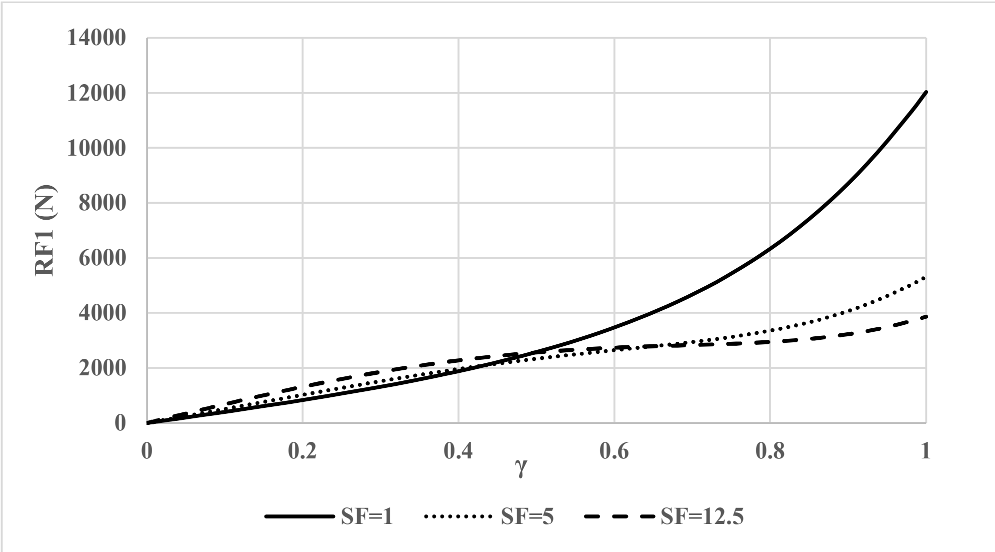

Figure 3.17. The static results for horizontal force with respect to shear strain for the different shape factors for incompressible case.

The shear stiffness for various shape factors are shown in Figure 3.18 and Figure 3.19 for incompressible case and $K_0/\mu_0 = 20$, respectively. The stiffness values were normalized with respect to SF=12.5 result. It is concluded that shear stiffness is mildly affected by the shape factor. In addition, shape factor affects the response in a similar way for various levels of compressibility.

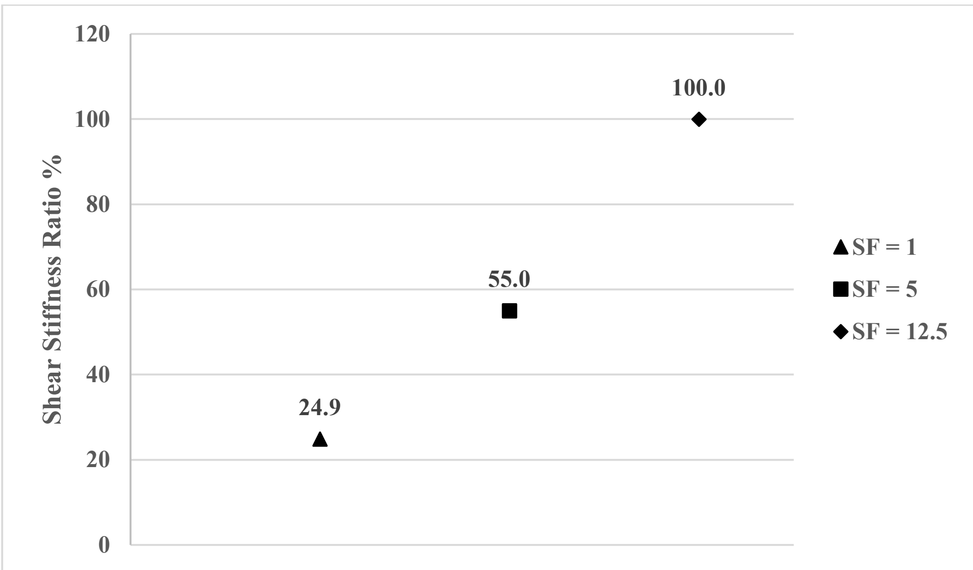

Figure 3.18. The static results for incompressible case where shear stiffness ratio is normalized with respect to the case of SF=12.5.

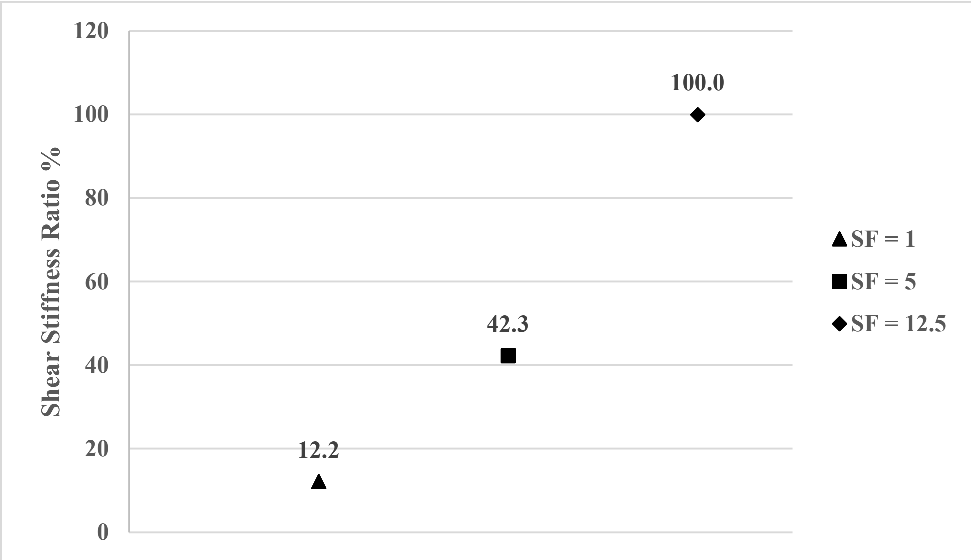

Figure 3.19. The static results for $K_0/\mu_0 = 20$ where shear stiffness ratio is normalized with respect to the case of SF=12.5.

3.2.2.2. Explicit Time Integration. Quasi-static analyses with explicit time integration were done to investigate the effects of compressibility and the loading rate on the horizontal force and horizontal displacement response of the bearing with shape factor of 5. Table 3.5 presents the KE/IE ratios for the different velocities and compressibility values.

Table 3.5. KE/IE for the model subjected to the combination of compression and shear loads.

Strain Rate	K_0/μ_0	**Duration (s)**	**KE/IE %**
2/s	10	0.5	0.5
	20	0.5	1.03
	50	0.5	3.7
	100	0.5	6.3
0.4/s	10	2.5	0.02
	20	2.5	0.03
	50	2.5	0.05
	100	2.5	0.16

Figures 3.20 and 3.21 show horizontal force-displacement response of the model for $K_0/\mu_0 = 100$ and $K_0/\mu_0 = 20$. According to the figures, for a given compressibility, quasi-static solution with explicit time integration follows the response path predicted with static solution with implicit time integration.

According to Figure 3.20, for $K_0/\mu_0 = 100$, noise is present in explicit integration for the high loading rate (2/s). On the other hand, Figure 3.21 shows that explicit integration noise is significantly reduced for $K_0/\mu_0 = 20$. Quasi-static solutions for a given loading velocity become closer to static solutions with increasing compressibility.

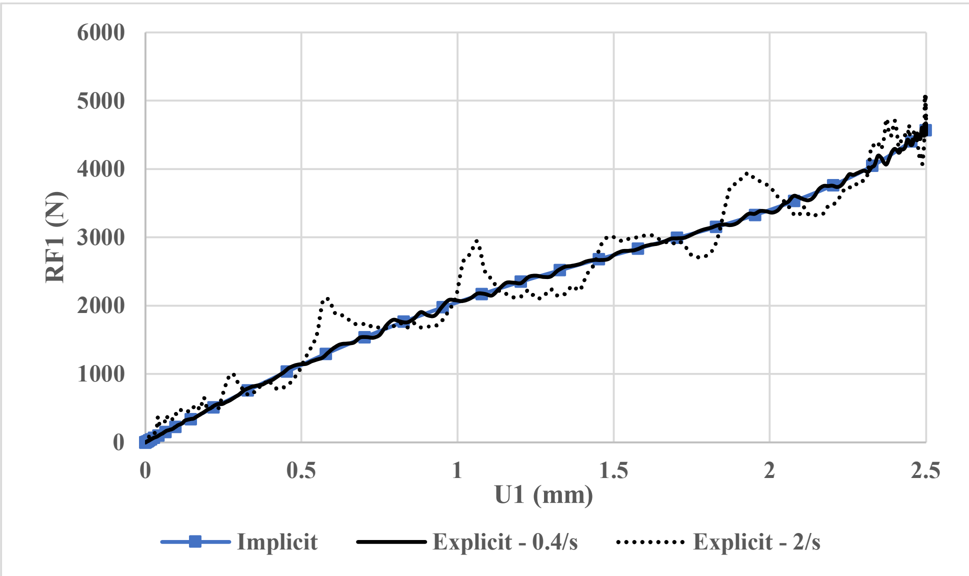

Figure 3.20. The static and quasi-static results for horizontal force for the different velocities for $K_0/\mu_0 = 100$.

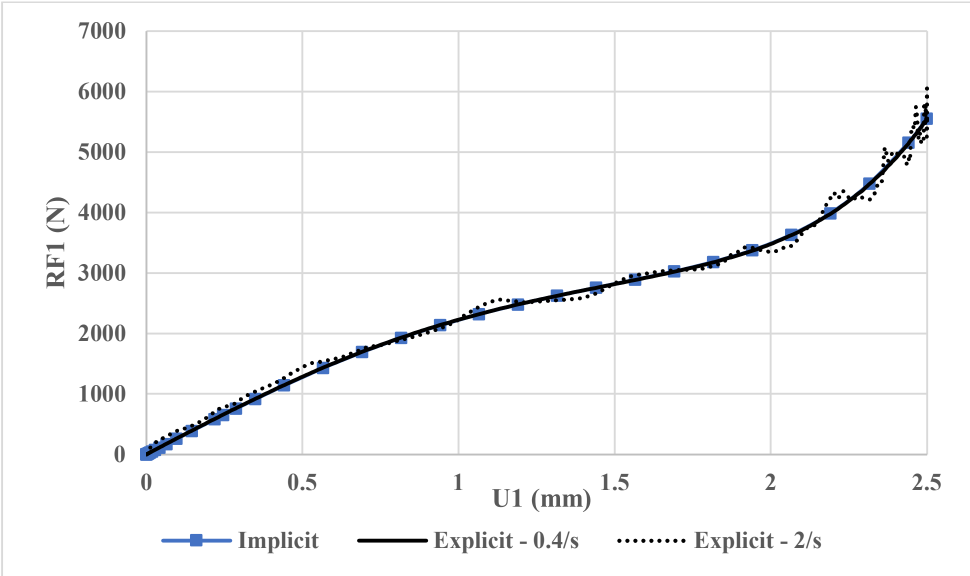

Figure 3.21. The static and quasi-static results for horizontal force for the different velocities for $K_0/\mu_0 = 20$.

The following are concluded according to the combined compressive and shear loading results presented in Section 3.2.2.

- Nearly the same horizontal force response is obtained for all shape factors for $\gamma \leq 0.5$.
- For $\gamma > 0.5$, horizontal force increases with decrease in shape factor.
- Shape factor (confinement) mildly affects shear stiffness. Shear stiffness gets larger as shape factor increases.
- Shape factor affects the shear stiffness in a similar trend for various levels of compressibility.
- Results of quasi-static solution follows the response path predicted with static solution for any compressibility and/or loading rate.
- For the high loading rate (2/s), noise is present in quasi-static analysis for $K_0/\mu_0 = 100$.
- Results of quasi-static analysis for a given loading velocity become closer to static solutions as compressibility increases.

3.2.3. Results of the Dynamic Analysis with Implicit Time Integration

The results presented in this section are for the bearings subjected to either compression only or combination of compression and shear loads. Dynamic analyses with implicit time integration of the model with shape factor of 5 were performed and results were compared with quasi-static analyses with explicit time integration. Effects of the loading rate and compressibility were studied. Tables 3.6 and 3.7 present the KE/IE ratios for different velocities and compressibility values. According to the tables, slightly lower KE/IE ratios were obtained compared to those for explicit analyses presented in Tables 3.4 and 3.5 for compression load only and for the combination of compression and shear loads, respectively.

Table 3.6. KE/IE for the model subjected to compression load.

Strain Rate	K_0/μ_0	**Duration (s)**	**KE/IE %**
2/s	20	0.107	1.03
	100	0.030	15.07
0.4/s	20	0.534	0.04
	100	0.150	1.13

Table 3.7. KE/IE for the model subjected to the combination of compression and shear loads.

Strain Rate	K_0/μ_0	**Duration (s)**	**KE/IE %**
2/s	20	0.5	0.57
	100	0.5	5.29
0.4/s	20	2.5	0.20
	100	2.5	0.32

Figures 3.22 and 3.23 show vertical force and vertical displacement response for compression only, at $K_0/\mu_0 = 100$ and $K_0/\mu_0 = 20$. It is observed that fluctuations occur for the analysis with strain rate of 2/s in dynamic implicit analysis. The amplitude of fluctuations decreases with increasing compressibility. For vertical response, quasi-static

analyses with explicit time integration provide sufficient accuracy with respect to dynamic analyses with implicit time integration, especially at lower strain rate (0.4/s).

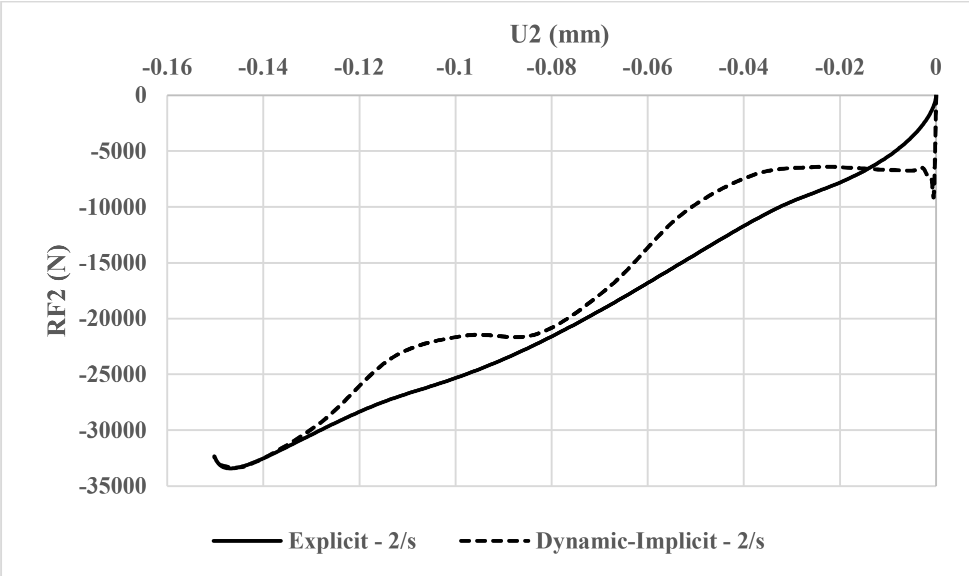

(a)

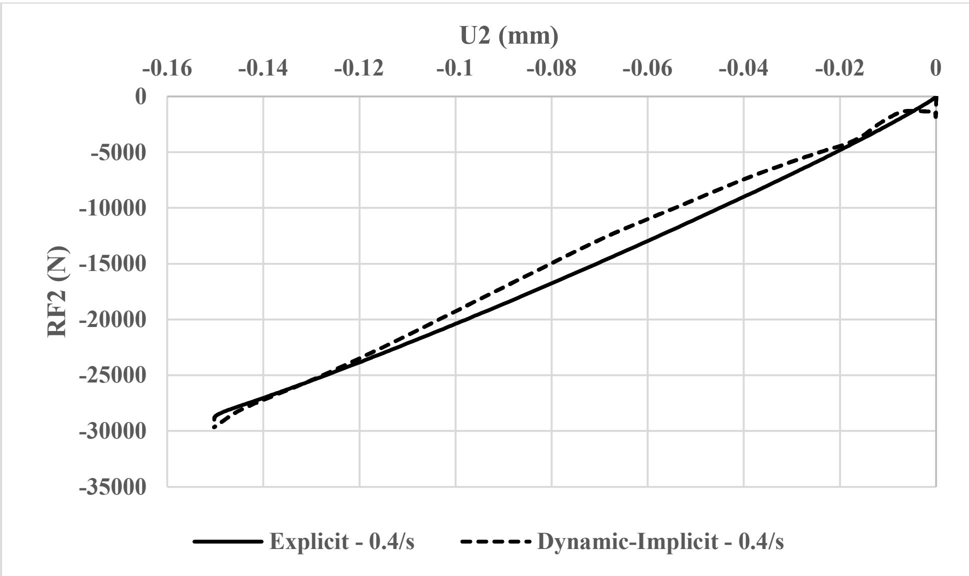

(b)

Figure 3.22. The quasi-static and dynamic results for vertical force-displacement response for $K_0/\mu_0 = 100$ for strain rate 2/s (a) and 0.4/s (b).

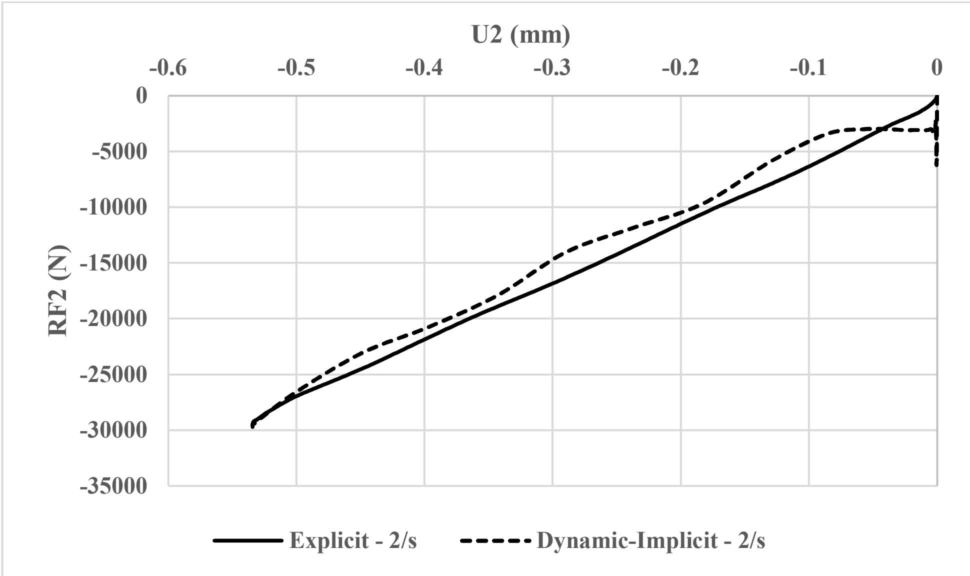

(a)

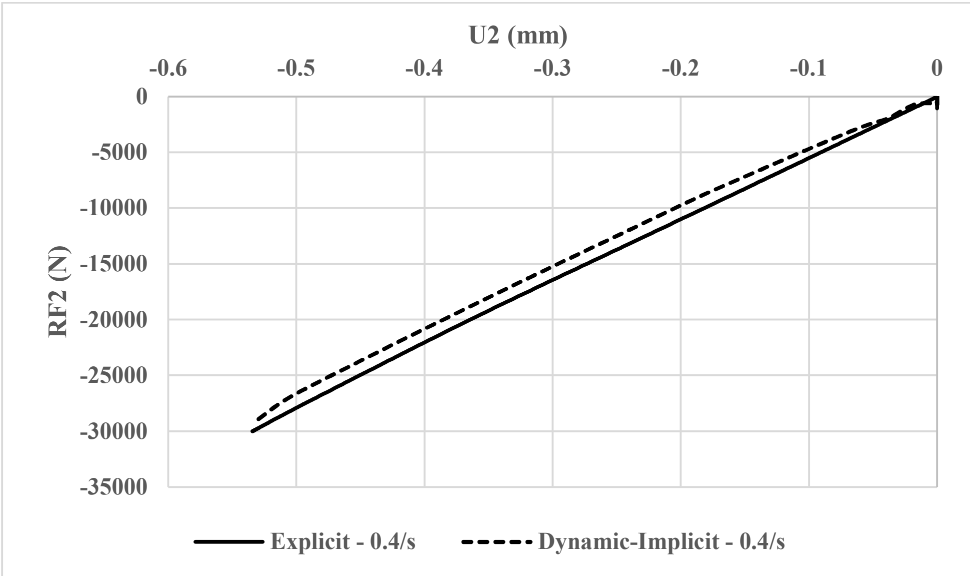

(b)

Figure 3.23. The quasi-static and dynamic results for vertical force-displacement response for $K_0/\mu_0 = 20$ for strain rate 2/s (a) and 0.4/s (b).

Figures 3.24 and 3.25 show results for horizontal force and horizontal displacement response for combination of compression and shear, at $K_0/\mu_0 = 100$ and $K_0/\mu_0 = 20$, respectively. Overall, explicit analysis results follow the results of dynamic analyses with implicit time integration. Increase in compressibility from $K_0/\mu_0 = 100$ to $K_0/\mu_0 = 20$ reduces the fluctuations for horizontal response.

Based on Figure 3.22 through Figure 3.25, the analysis at higher strain rate (2/s) exhibits noisier response than the analysis with lower strain rate (0.4/s) in both explicit analysis and dynamic implicit analysis.

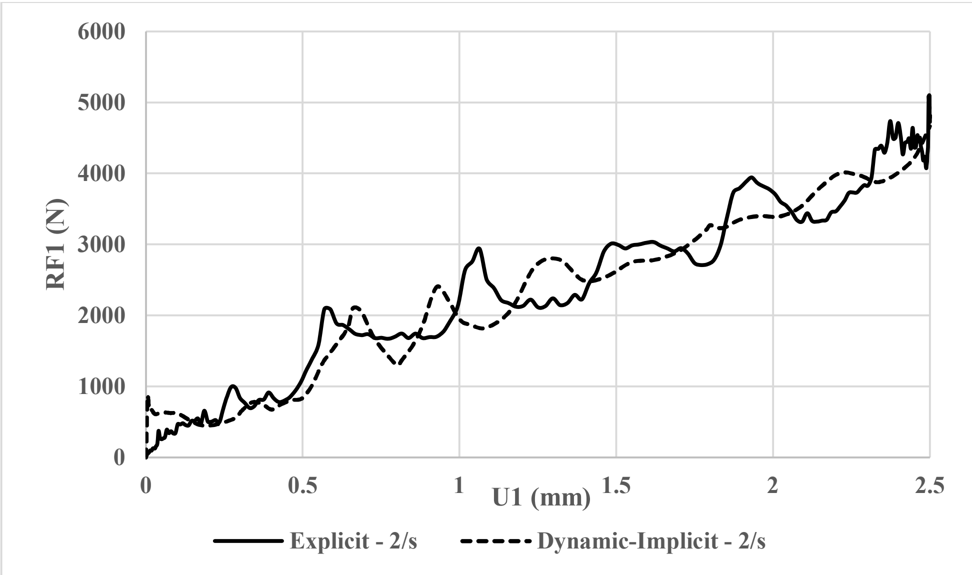

(a)

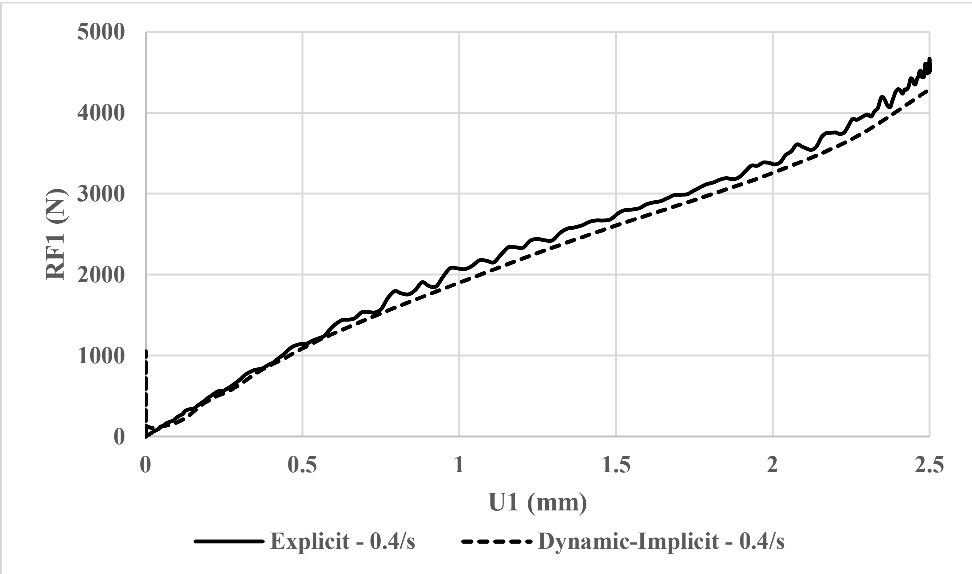

(b)

Figure 3.24. The quasi-static and dynamic results for horizontal force-displacement response for $K_0/\mu_0 = 100$ for strain rate 2/s (a) and 0.4/s (b).

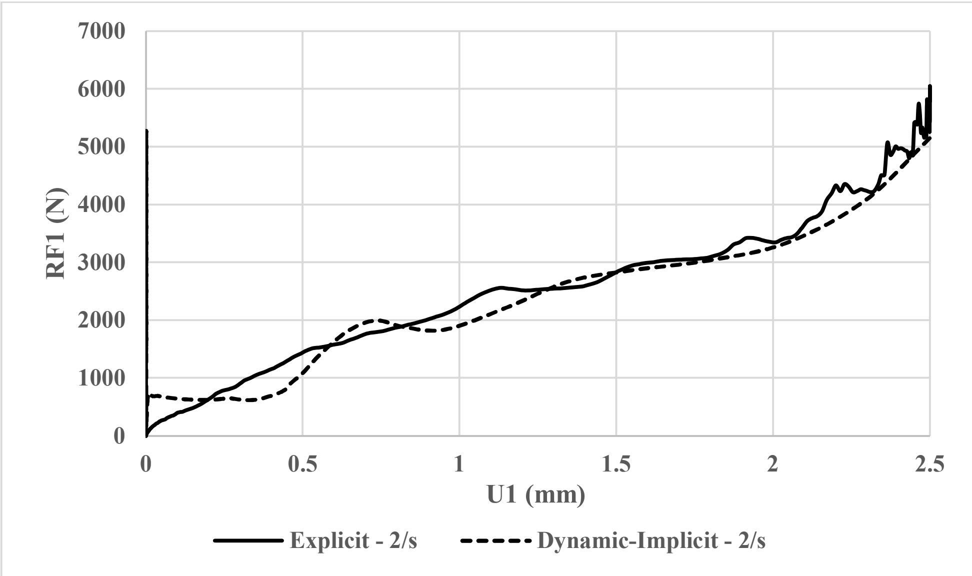

(a)

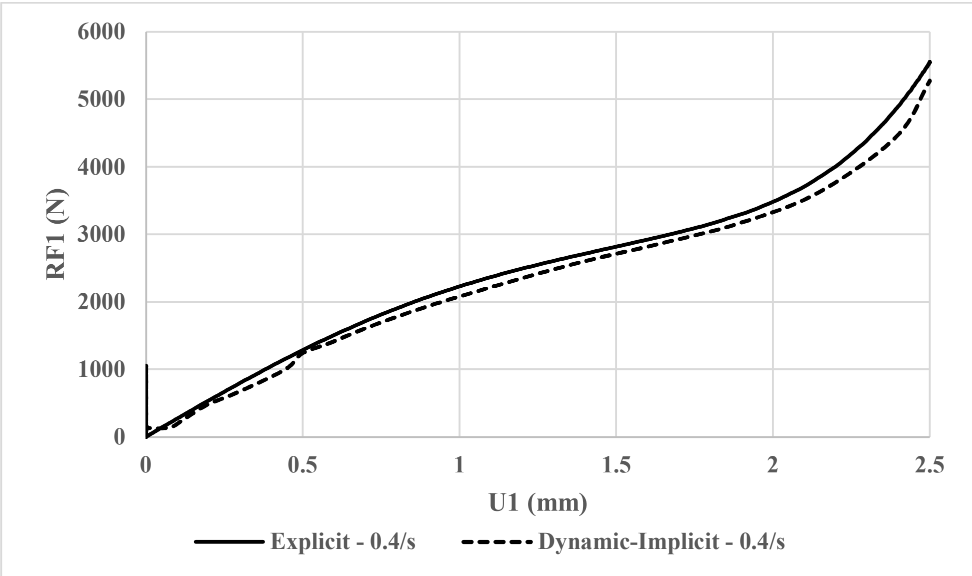

(b)

Figure 3.25. The quasi-static and dynamic results for horizontal force-displacement response for $K_0/\mu_0 = 20$ for strain rate 2/s (a) and 0.4/s (b).

The following are concluded according to the results presented in this section.

- In implicit analysis, slightly lower KE/IE ratios were gathered compared to explicit analysis.
- For vertical and horizontal responses, fluctuation is present in dynamic analysis at higher strain rate (2/s). Increase in compressibility decreases fluctuations.

- For vertical and horizontal responses, the analyses with explicit time integration show sufficient accuracy with respect to the analyses with implicit time integration.
- For horizontal response, results of the analyses with explicit time integration follow the response predicted with implicit time integration.

3.3. Conclusions

The followings are concluded based on the results presented in this chapter.

- The effect of the shape factor on the stiffness is much more pronounced in the vertical direction as compared to horizontal direction.
- The effect of shape factor on vertical stiffness decreases with increasing compressibility, while the effect on shear stiffness does not considerably change for various levels of compressibility.
- The use of lower K_0/μ_0 for rubber results in significant error in the predictions of the vertical stiffness as compared to the solution for an incompressible material behavior. This error increases with increasing shape factor.
- Lower KE/IE values are obtained as compressibility increases and/or loading velocity decreases.
- Compressibility of a rubber material is one of the major concerns in terms of the accuracy of a finite element solution in an explicit analysis. For higher K_0/μ_0 (100), significant noise is present in quasi-static-explicit integration solution and results diverge from static solution with implicit integration. For lower K_0/μ_0 (20), explicit integration noise is significantly reduced, and results overlap with those from implicit solution.
- The horizontal response for $\gamma \leq 0.5$ is nearly the same for all shape factors.

4. FINITE ELEMENT ANALYSIS OF AN ELASTOMER BEARING WITH VISCOELASTIC MATERIAL PROPERTIES

Finite element model of a plain elastomer bearing with viscoelastic material properties is presented in this chapter. Previously, finite element model of a plain rubber bearing with hyperelastic properties was presented in Chapter 3.

The response of the bearing under either compression load or combination of compression and shear loads was studied. The effects of compressibility, viscoelasticity, and velocity on vertical and horizontal response of the bearing were investigated in static analysis with implicit time integration. Also, quasi-static analysis with explicit time integration was performed and the effect of loading velocity on the predictions was determined.

4.1. Finite Element Model

In this section, viscoelastic material model, geometry, loading and boundary conditions, mesh properties of the finite element model are presented.

4.1.1. Material Model

The elastomer was considered to be HDR as in Chapter 3 and was represented with a viscoelastic material model. The experimental data for HDR was taken from the literature [5]. The available data consisted of stress relaxation response for uniaxial compression and simple shear.

A nonlinear viscoelastic material model was calibrated. The model consisted of a relaxation function combined with a hyperelastic model. Elastic response of the material model was obtained from Yeoh form of strain energy and was described in Section 3.1.1 of this thesis. The relaxation function was represented with Prony series. The Prony terms were determined using the least square method. The experimental data and the resulting curve fit for simple shear are shown in Figure 4.1. The resulting coefficients of Prony series are given in Table 4.1.

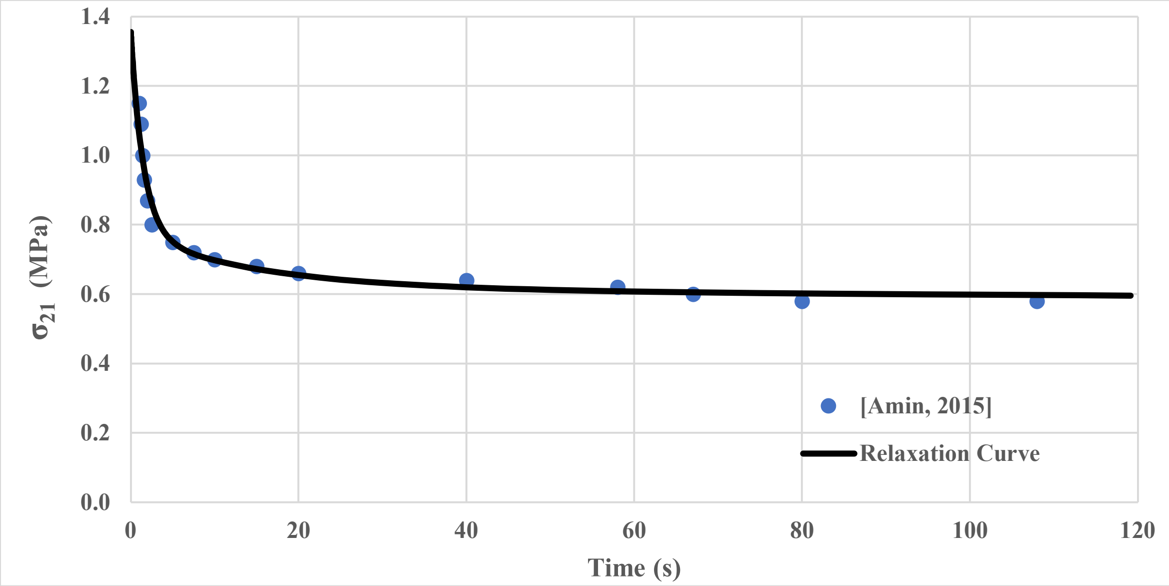

Figure 4.1. Shear stress relaxation response of viscoelastic material model (test data [5]).

Table 4.1. The Prony series coefficients.

G_1	G_2	G_3	τ_1	τ_2	τ_3
0.57941	0.15825	0.04063	1.5	15	150

The equilibrium shear modulus is $G_\infty = 0.57778$ MPa.

The volumetric behavior of rubber was assumed to be incompressible.

To investigate the effect of loading rate on response of viscoelastic material model, two different strain rates (0.4/s and 2/s) were studied. Figure 4.2 shows stress-stretch response for uniaxial compression. Figure 4.3 shows stress-strain response for simple shear. It is concluded that stress relaxation gets higher as loading rate decreases for both loading types.

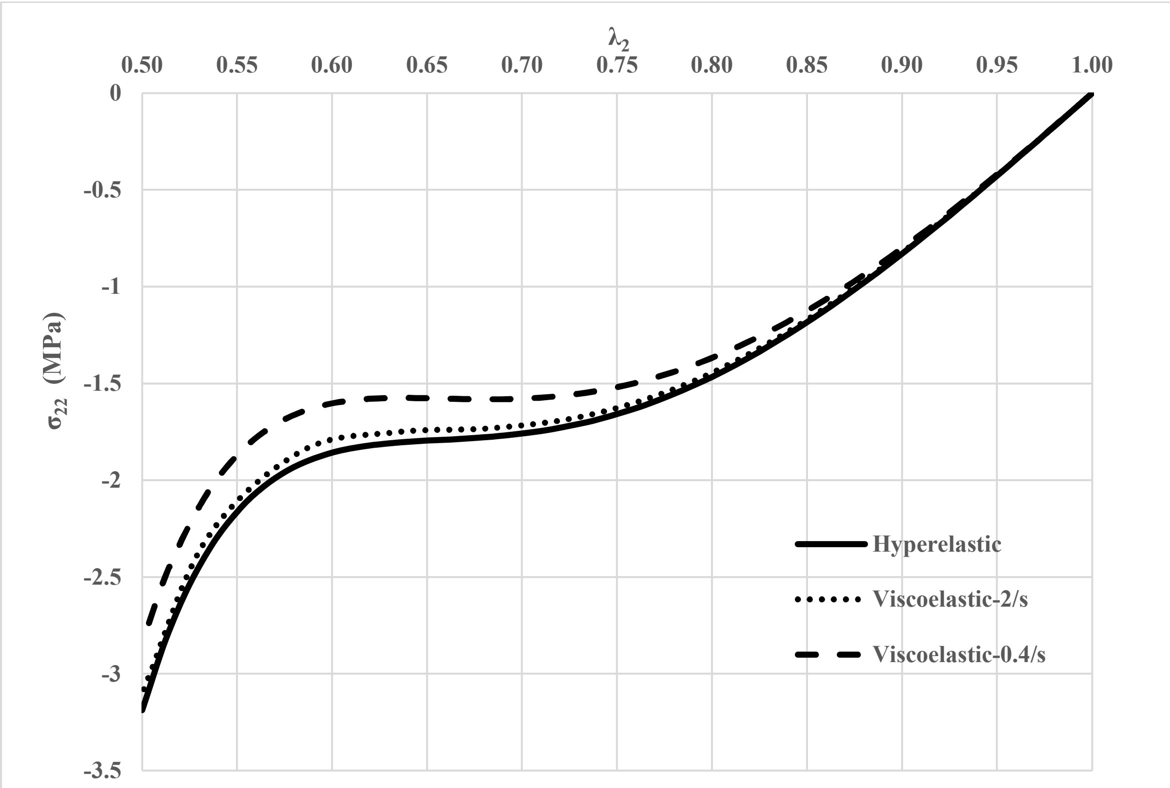

Figure 4.2. Loading rate effect for viscoelastic model subjected to uniaxial compression.

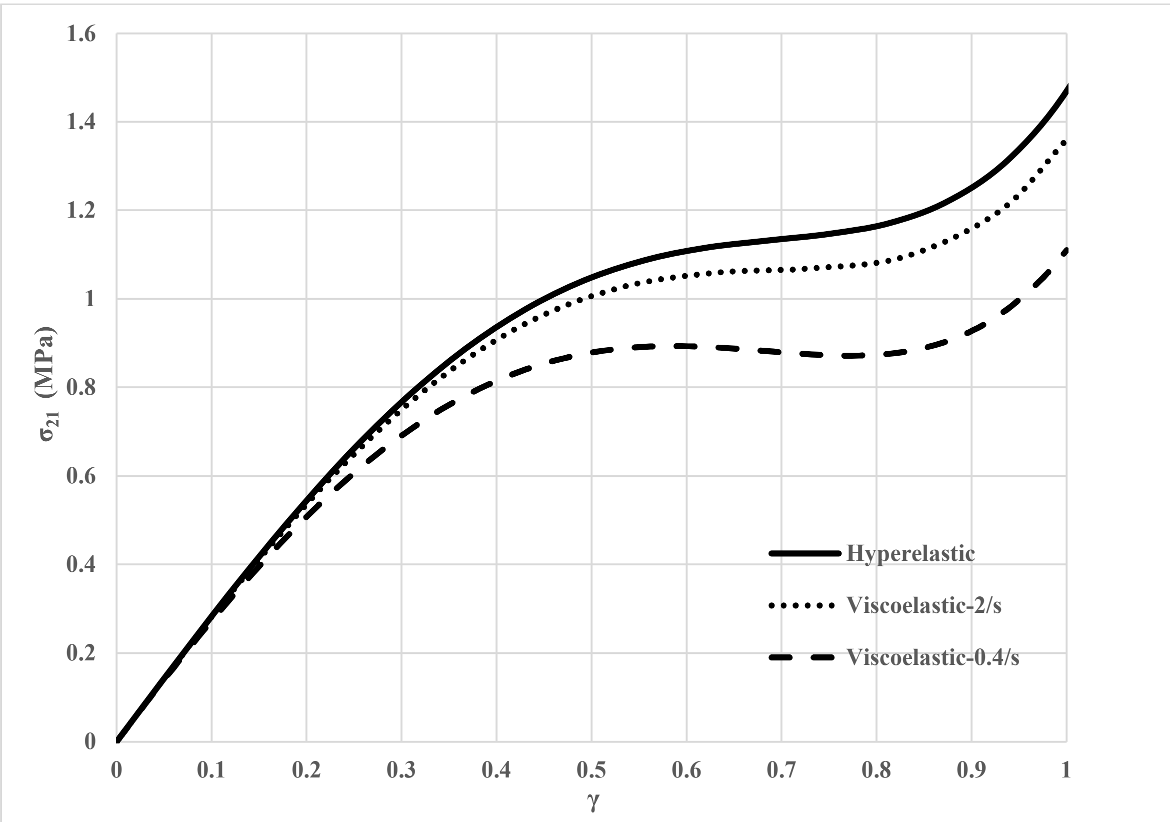

Figure 4.3. Loading rate effect for viscoelastic model subjected to simple shear.

To validate the calibrated material model, long and short term responses were predicted for incompressible case under simple shear load at different strain rates (0.1/s, 0.01/s and 0.005/s) as shown in Figure 4.4. As the loading rate decreases, shear stress-strain behavior resembles to equilibrium response presented in [4]. This proves that the constructed material model with viscoelastic properties agrees with the experimental data.

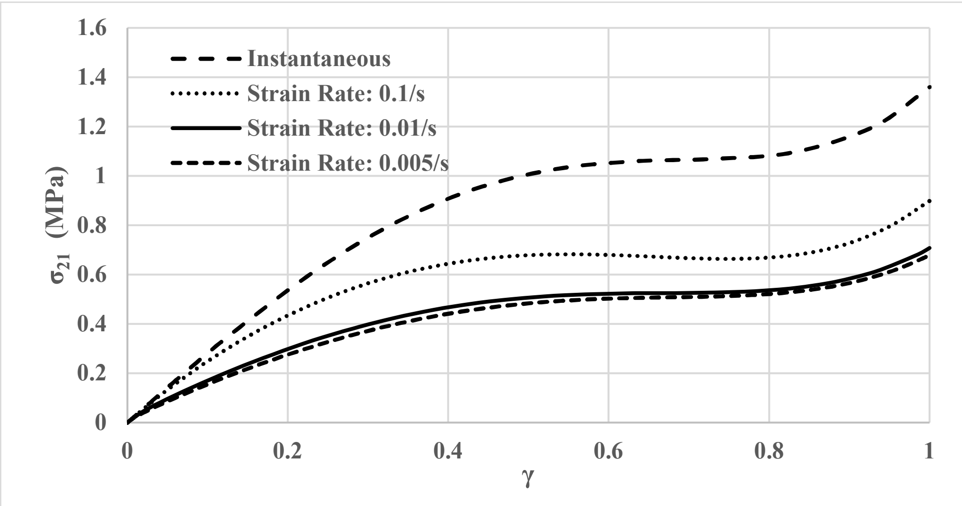

Figure 4.4. Instantaneous and equilibrium response of viscoelastic material model.

The rubber density was taken as $1\ g/cm^3$ for explicit analyses.

4.1.2. Geometry of the Problem

A rectangular bearing with shape factor of 5, which corresponds to the side dimensions of 50x50 mm and thickness of 2.5 mm, was selected. The geometry is shown in Figure 3.4.

4.1.3. Mesh

Plane strain analysis of the bearings was conducted. Mesh consisted of quadrilateral, reduced integration, linear elements for static analyses with implicit integration and quasi-static analyses with explicit integration. Hybrid elements were considered for the analysis with implicit integration. In summary, the elements used for predictions are the followings:

- CPE4RH for the analysis with implicit time integration
- CPE4R for the analysis with explicit time integration

The mesh structure for the geometry is shown in Figure 3.7.

4.1.4. Loading and Boundary Conditions

Bearings were subjected to either compression load or combination of compression and shear loads. The loads were applied as described in Section 3.1.4 of this thesis. Table 4.2 is extracted from Table 3.2 and lists the vertical displacements for SF=5. The applied horizontal displacement for SF=5 is 2.5 mm which corresponds to the shear strain of 1.

Table 4.2. Total load and the corresponding vertical displacements in the FE models of the bearing with SF=5.

SF	K_0/μ_0	Total Load (N)	Vertical Displacement (mm)
5	10	30000	-0.9255
	20	30000	-0.5343
	50	30000	-0.2549
	100	30000	-0.1503
	∞	30000	-0.0355

The boundary conditions and contact behavior were defined as described in section 3.1.4 of this thesis.

4.2. Results

The finite element predictions were evaluated for the following quantities: vertical force, vertical stiffness, horizontal force and horizontal stiffness.

For static analysis with implicit time integration and quasi-static analysis with explicit time integration, the effects of the following parameters on the response were investigated.

- Compressibility
- Viscoelasticity
- Loading Velocity

4.2.1. Results for Compressive Loading

The results presented in this section are for the bearings subjected to compression load only. The analyses were conducted with implicit and explicit time integrations.

4.2.1.1. Effects of Compressibility, Viscoelasticity, and Loading Velocity. The vertical force and vertical displacement predictions for incompressible case and $K_0/\mu_0 = 20$ are shown in Figures 4.5a and 4.5b, respectively. The figures highlight that for a given compressibility vertical response of the bearing is not affected by viscoelasticity and/or loading velocity for the considered range of strain rate. The conclusions regarding the compressibility effect are the same as those presented in Section 3.2.1.1.

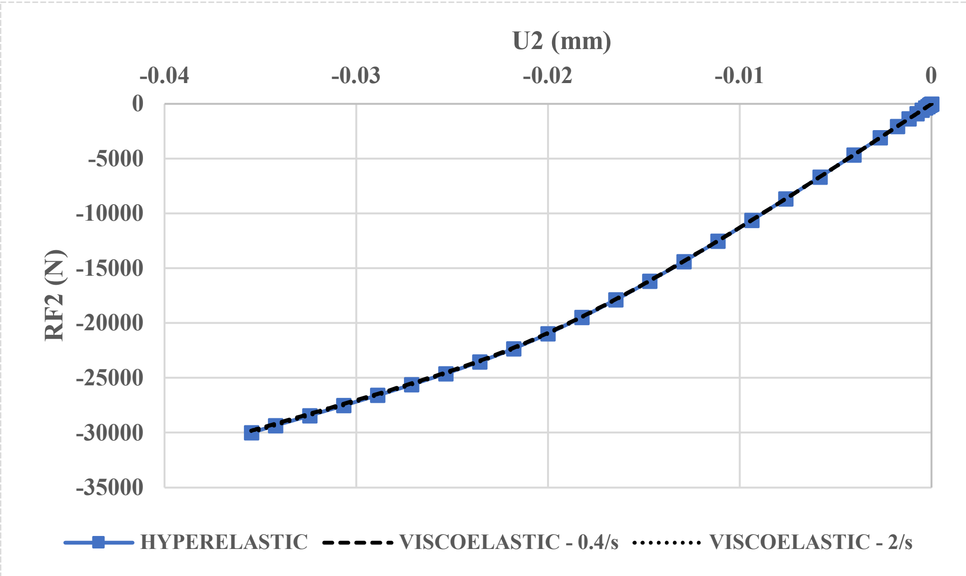

Figure 4.5a. The static results for vertical force-displacement response for incompressible case.

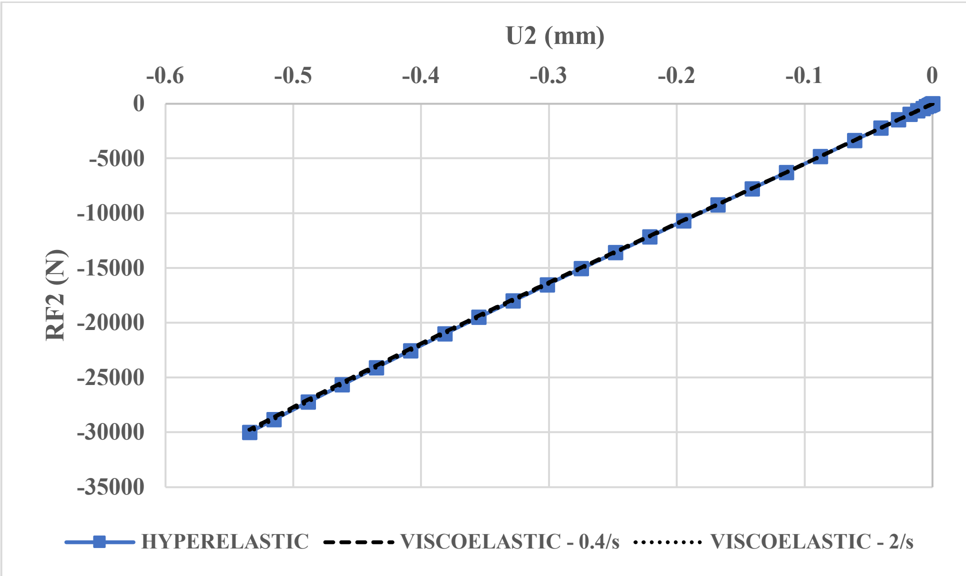

Figure 4.5b. The static results for vertical force-displacement response for $K_0/\mu_0 = 20$.

4.2.1.2. Explicit Time Integration. Quasi-static analyses with explicit time integration were performed to evaluate the effects of the loading rate and compressibility on the vertical force and vertical displacement response of the bearing.

The KE/IE ratios obtained for the viscoelastic bearings were the same as the KE/IE ratios calculated for hyperelastic model presented in Section 3.2.1.2 of this thesis. Therefore, it is concluded that viscoelasticity has no effect on the KE/IE ratio for the range of strain rates considered in this study.

Figures 4.6 and 4.7 present vertical force and vertical displacement responses of the viscoelastic model for $K_0/\mu_0 = 100$ and $K_0/\mu_0 = 20$, respectively. For lower strain rate (0.4/s), explicit solution overlaps with the implicit solution. Explicit solution for strain rate of 2/s, on the other hand, deviates from the implicit solution. It is concluded that explicit analysis at higher strain rate (2/s) deviates from implicit solution.

Figure 4.7 ($K_0/\mu_0 = 20$) indicates that explicit solution for both strain rates of 0.4/s and 2/s overlaps with implicit solution. In consideration of Figure 4.6 ($K_0/\mu_0 = 100$), it is concluded that as compressibility increases, explicit solutions for a given loading velocity become closer to implicit solutions.

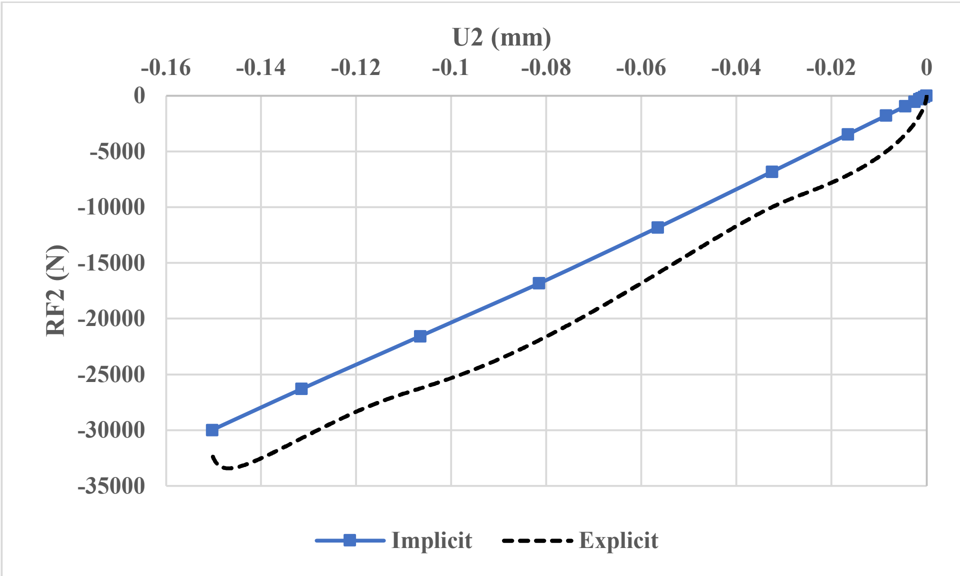

(a)

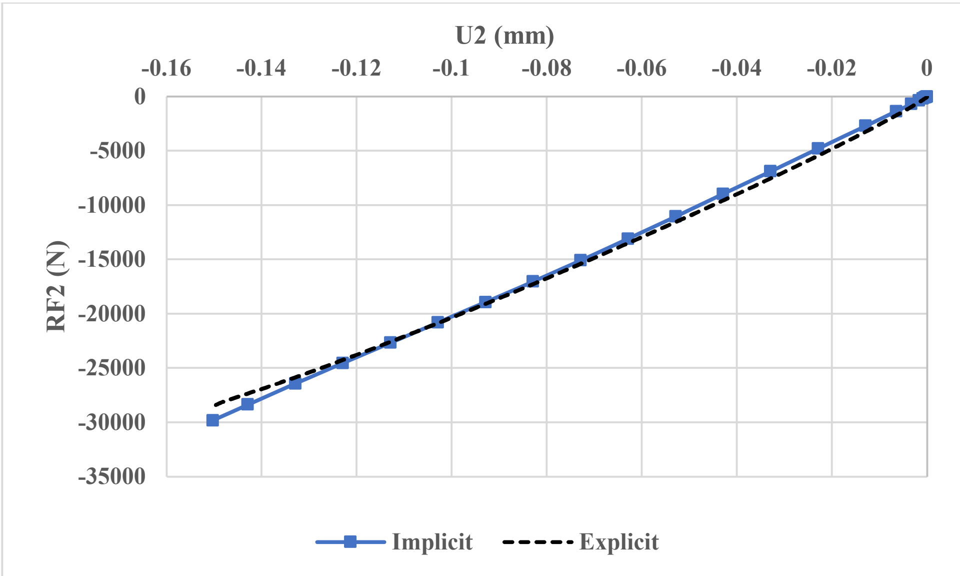

(b)

Figure 4.6. The static and quasi-static results for vertical force-displacement response for $K_0/\mu_0 = 100$ for strain rate 2/s (a) and 0.4/s (b).

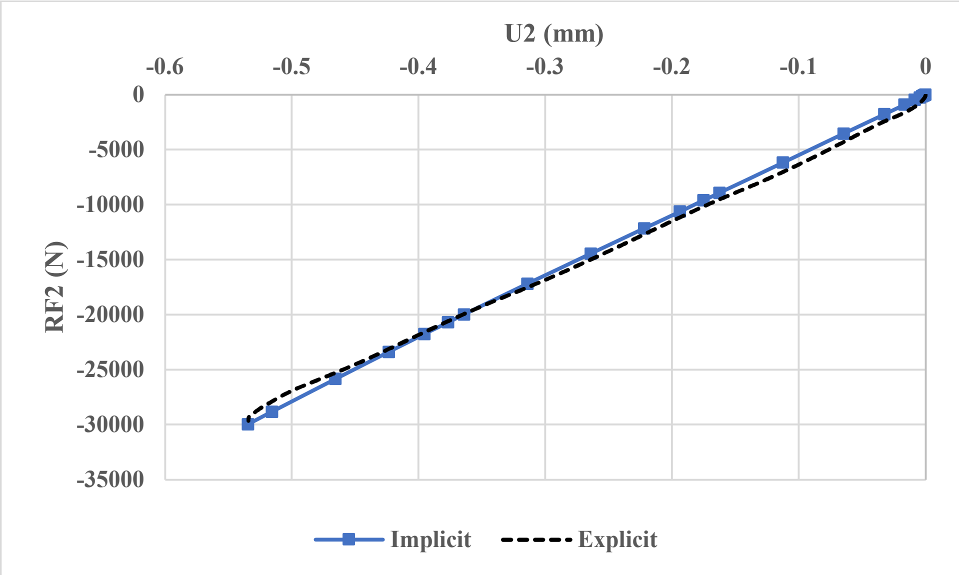

(a)

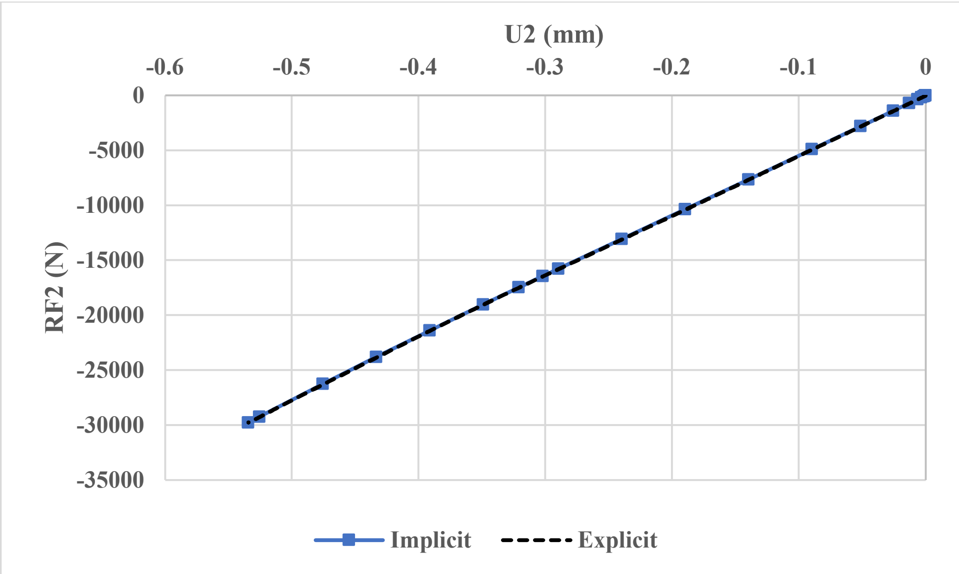

(b)

Figure 4.7. The static and quasi-static results for vertical force-displacement response for $K_0/\mu_0 = 20$ for strain rate 2/s (a) and 0.4/s (b).

The following are concluded based on the compressive loading results presented in Section 4.2.1.

- For a given compressibility, vertical response of the bearing is not affected by viscoelasticity and/or loading velocity, for the considered range of strain rates.

- For vertical response, viscoelasticity has no effect on the KE/IE ratio as compared to the KE/IE ratios with hyperelastic model predictions, for the considered range of strain rates.
- Predictions with explicit analysis at higher strain rate (2/s) deviate from predictions with implicit analysis.
- For a given loading velocity, results of quasi-static analysis become closer to static solutions as compressibility increases.

The above conclusions are consistent with the elastic volumetric behavior assumed for the bearing.

4.2.2. Results for Combined Compressive and Shear Loading

The results presented in this section are for the bearings subjected to combination of compression and shear loads. The analyses were conducted with implicit and explicit time integrations.

4.2.2.1. Effects of Compressibility, Viscoelasticity, and Loading Velocity. The horizontal force and horizontal displacement predictions for incompressible case and $K_0/\mu_0 = 20$ are presented in Figure 4.8. The figure shows that horizontal response is mildly affected by viscoelasticity. The effect of viscoelasticity decreases as compressibility increases. Also, for a given compressibility, viscoelastic predictions become closer to hyperelastic results as loading velocity increases. Since hyperelastic model was based on instantaneous material response, this conclusion is not surprising.

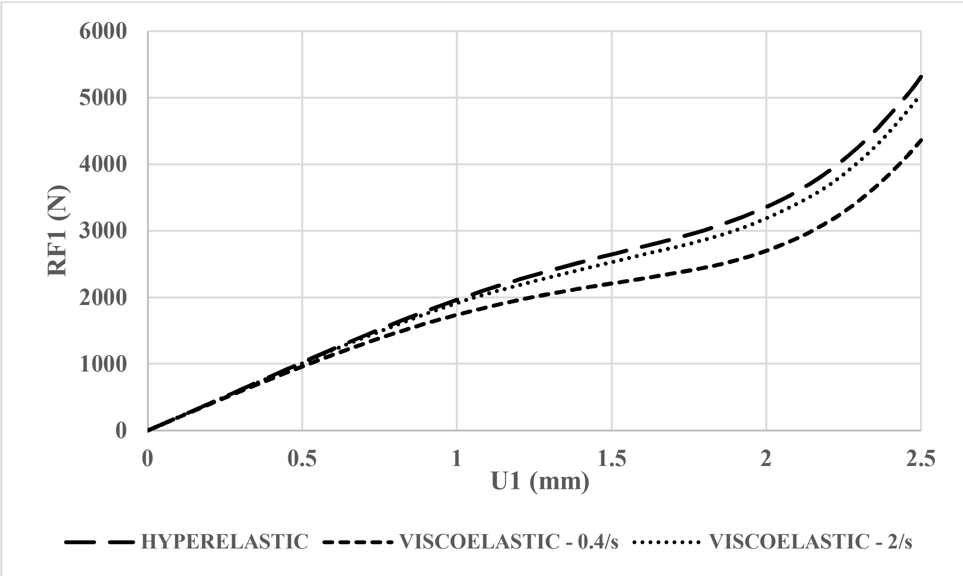

(a)

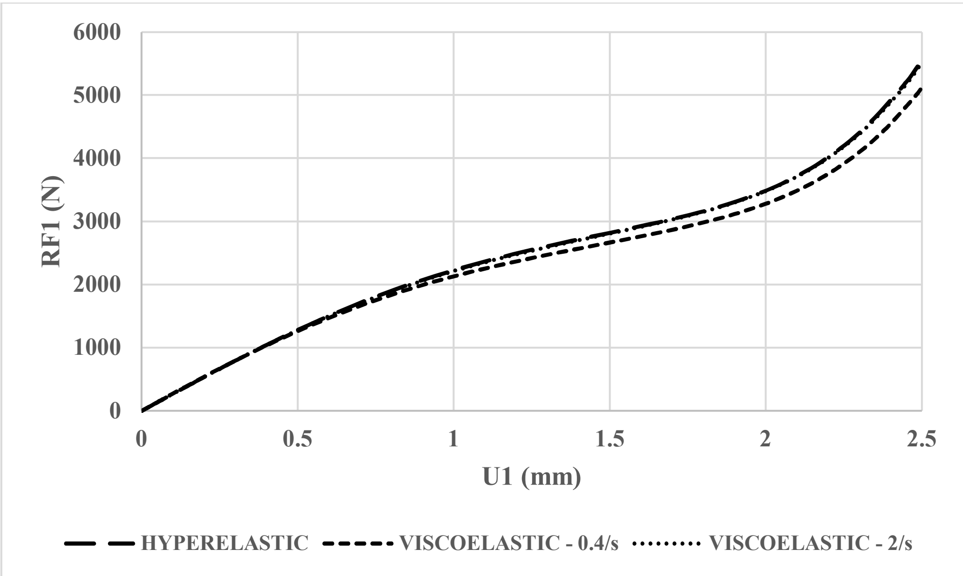

(b)

Figure 4.8. The static results for horizontal force-displacement response for incompressible case (a) and $K_0/\mu_0 = 20$ (b).

The shear stiffness for various compressibility levels (10, 20, 50, 100 and incompressible) are shown in Figure 4.9 where the stiffness values were normalized with respect to those for the incompressible hyperelastic case. For both hyperelastic and viscoelastic models regardless of loading velocity, the stiffness values slightly decrease from incompressible case to $K_0/\mu_0 \cong 90$. Then, the stiffness values slightly increase from $K_0/\mu_0 \cong 90$ to $K_0/\mu_0 = 20$. There is a sharp increase in stiffness values between $K_0/\mu_0 =$

20 and $K_0/\mu_0 = 10$. Therefore, modeling nearly incompressible bearings with higher compressibility ($K_0/\mu_0 \leq 20$) in explicit analysis likely results in significant error for shear response predictions.

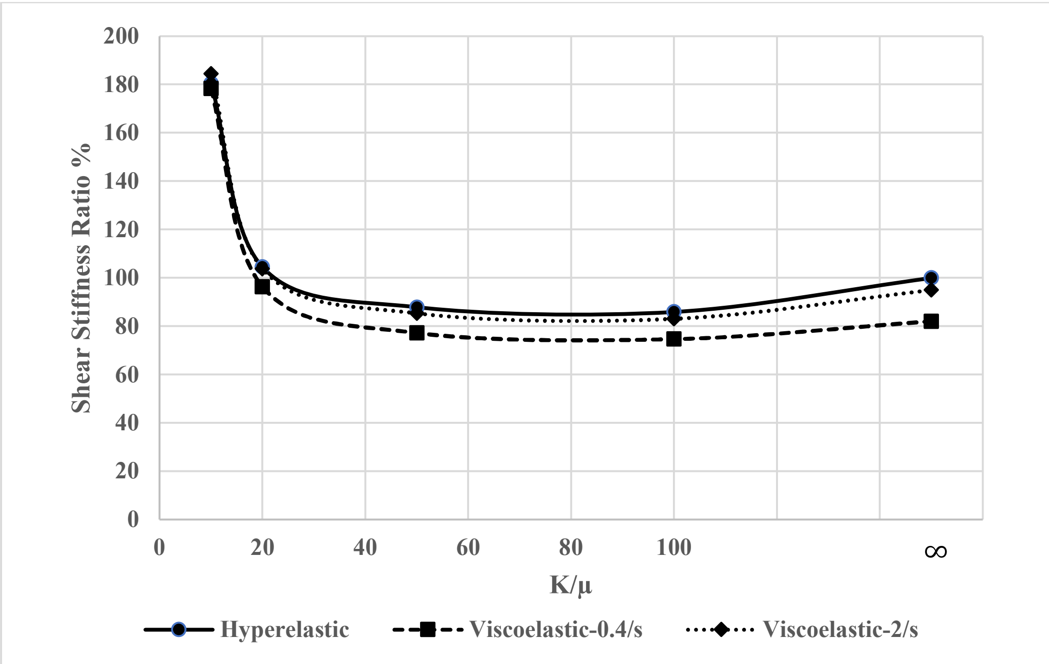

Figure 4.9. The static results for different compressibility values where shear stiffness ratio is normalized with respect to incompressible result of hyperelastic case.

4.2.2.2. Explicit Time Integration. Quasi-static analyses with explicit time integration were done to investigate the effects of the loading rate and compressibility on the horizontal force and horizontal displacement response of a bearing.

The KE/IE ratios obtained for the viscoelastic bearings were the same as the KE/IE ratios presented for hyperelastic model in Section 3.2.2.2 of this thesis. It is concluded that viscoelasticity has no effect on the KE/IE ratio for the range of strain rates considered in this study.

Figures 4.10 and 4.11 present horizontal force and horizontal displacement responses of the viscoelastic model for $K_0/\mu_0 = 100$ and $K_0/\mu_0 = 20$, respectively. According to the figures, for a given compressibility, explicit solution follows the response path predicted with the implicit solution.

According to Figure 4.10, for $K_0/\mu_0 = 100$, noise is present in explicit integration for the high loading rate (2/s). On the other hand, Figure 4.11 shows that explicit integration noise is significantly reduced for $K_0/\mu_0 = 20$. Explicit solutions for a given loading velocity become closer to implicit solutions with increasing compressibility.

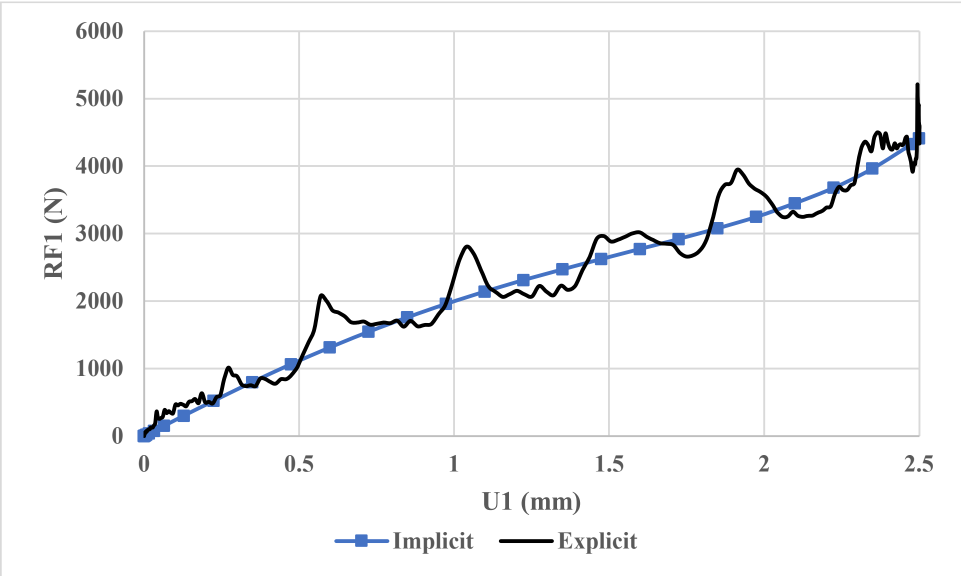

(a)

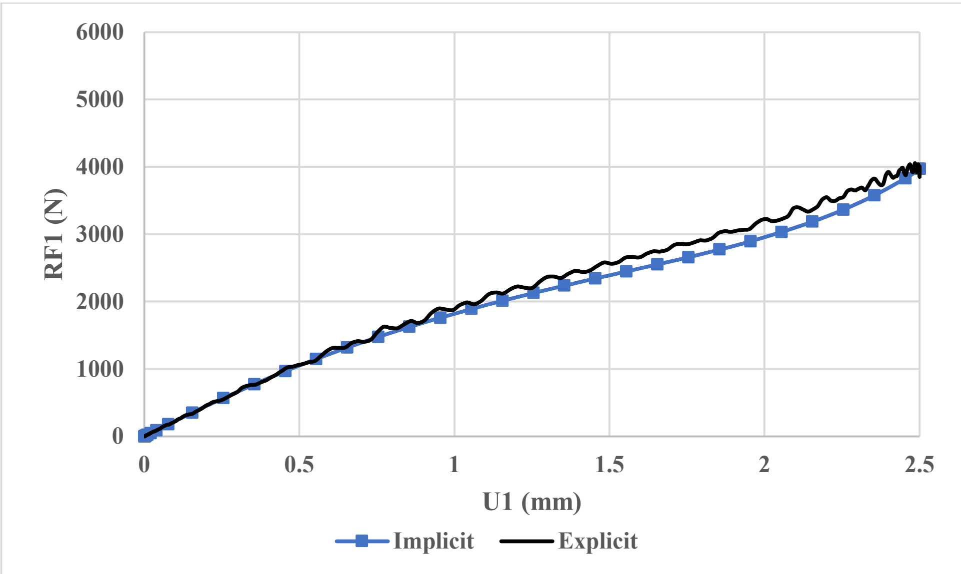

(b)

Figure 4.10. The static and quasi-static results for horizontal force-displacement response for $K_0/\mu_0 = 100$ for strain rate 2/s (a) and 0.4/s (b).

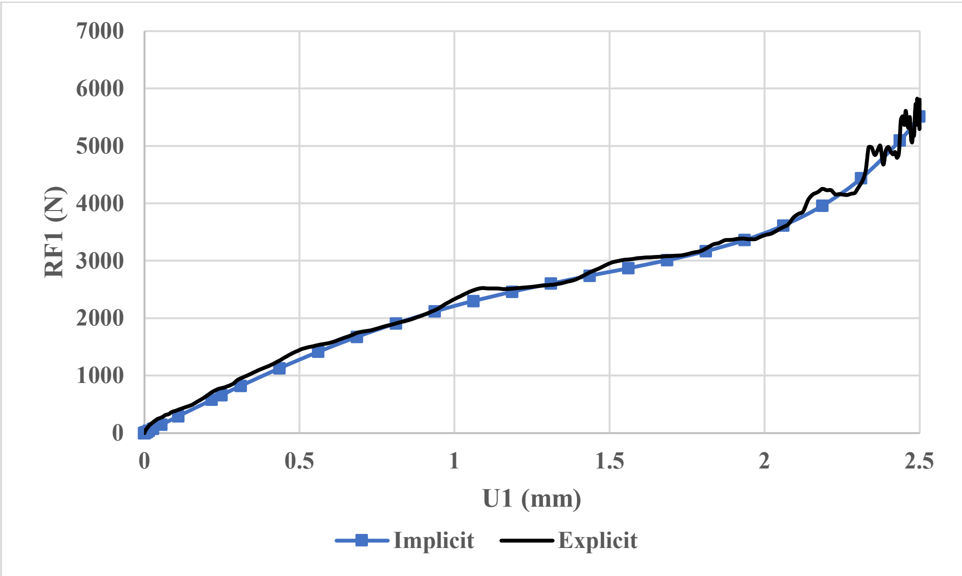

(a)

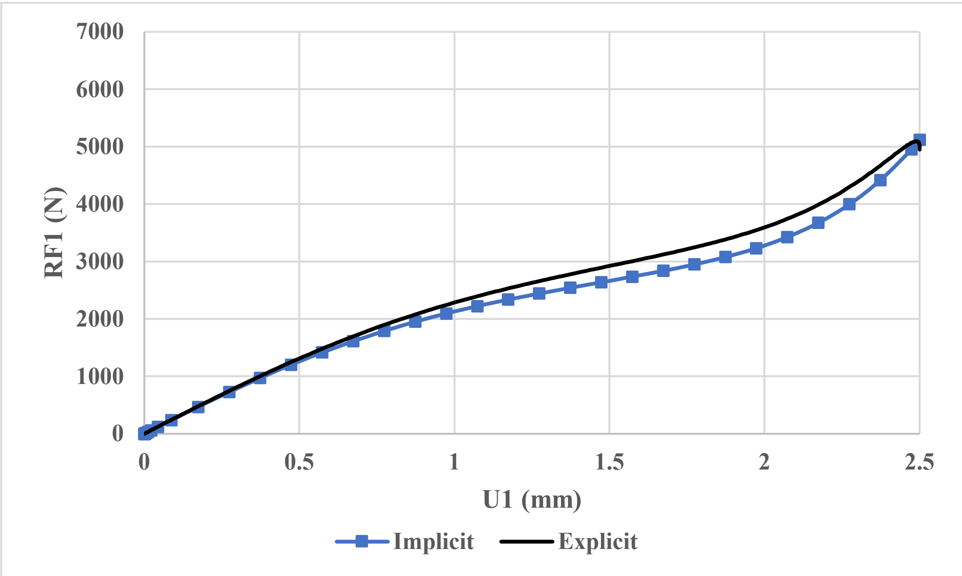

(b)

Figure 4.11. The static and quasi-static results for horizontal force-displacement response for $K_0/\mu_0 = 20$ for strain rate 2/s (a) and 0.4/s (b).

The following are concluded based on the combined compressive and shear loading results presented in Section 4.2.2.

- Viscoelasticity mildly affects horizontal response.
- The effect of viscoelasticity decreases as compressibility increases.

- For a given compressibility, as loading velocity increases viscoelastic results get closer to hyperelastic ones, since the latter was calibrated to instantaneous test data.
- The use of higher compressibility ($K_0/\mu_0 \leq 20$) for rubber results in significant error in the predictions of the shear stiffness as compared to that with an incompressible material behavior.
- For horizontal response, viscoelasticity has no effect on the KE/IE ratio as compared to the KE/IE ratios with hyperelastic model predictions, for the considered range of strain rates.
- Results of explicit solution follow the response path predicted with implicit solution for all considered compressibility levels and loading rates.
- For a given loading velocity, results of quasi-static analysis become closer to static solutions as compressibility increases.

4.3. Conclusions

The followings are concluded based on the results presented in this chapter.

- Stress relaxation increases as loading rate decreases for both uniaxial compression and simple shear.
- For a given compressibility, vertical response of the bearing is not affected by viscoelasticity and/or loading velocity, for the considered range of strain rates.
- Horizontal response is mildly affected by viscoelasticity. The effect of viscoelasticity decreases as compressibility increases. For a given compressibility, viscoelastic predictions become closer to hyperelastic results as loading velocity increases.
- The use of higher compressibility ($K_0/\mu_0 \leq 20$) for rubber results in significant error in the predictions of the shear stiffness as compared to the solution for an incompressible material behavior.
- For both vertical and horizontal response, viscoelasticity has no effect on the KE/IE ratio as compared to the KE/IE ratios with hyperelastic model predictions, for the considered range of strain rates.
- Predictions with explicit analysis at higher strain rate (2/s) deviate from predictions with implicit analysis.

- For horizontal response, results of explicit solution follow the response path predicted with implicit solution for any compressibility and loading rate considered in the study.
- For a given loading velocity, explicit solutions become closer to implicit solutions as compressibility increases.

5. FINITE ELEMENT ANALYSIS OF A COMPOSITE BEARING

In Chapters 3 and 4, finite element models of plain rubber bearing with hyperelastic and viscoelastic material properties were presented. In this chapter, a bearing composed of alternating layers of rubber and steel is considered. In particular, the response of the composite bearing under either compression load or combination of compression and shear loads was studied. Finite element analysis results are presented for global and local responses of the bearing.

For global response, the effect of rubber compressibility on vertical and horizontal response of the bearing was investigated in static analysis with implicit time integration. In addition, quasi-static analysis with explicit time integration was explored. For the explicit analysis, the effect of loading velocity on the predictions was evaluated.

For local response, the effects of loading type, boundary type, compression load magnitude, and rubber compressibility on stress distribution in rubber pads were investigated for static analysis with implicit time integration. In addition, the stress distribution at various interfaces was studied.

5.1. Finite Element Model

In this section, details of the finite element model such as material model of steel, geometry, mesh, and loading and boundary conditions are presented.

5.1.1. Material Models for Rubber and Steel

Rubber was represented with the same material model described in Chapter 3.

The steel was represented with an elastoplastic material model. In particular, kinematic hardening model was employed. The model parameters were taken from the literature [9].

- $E = 200\ GPa$
- $\nu = 0.3$
- $\sigma_{yield} = 276\ MPa$
- $E' = 1034\ MPa$

The uniaxial stress-strain behavior of steel for tension is shown in Figure 5.1.

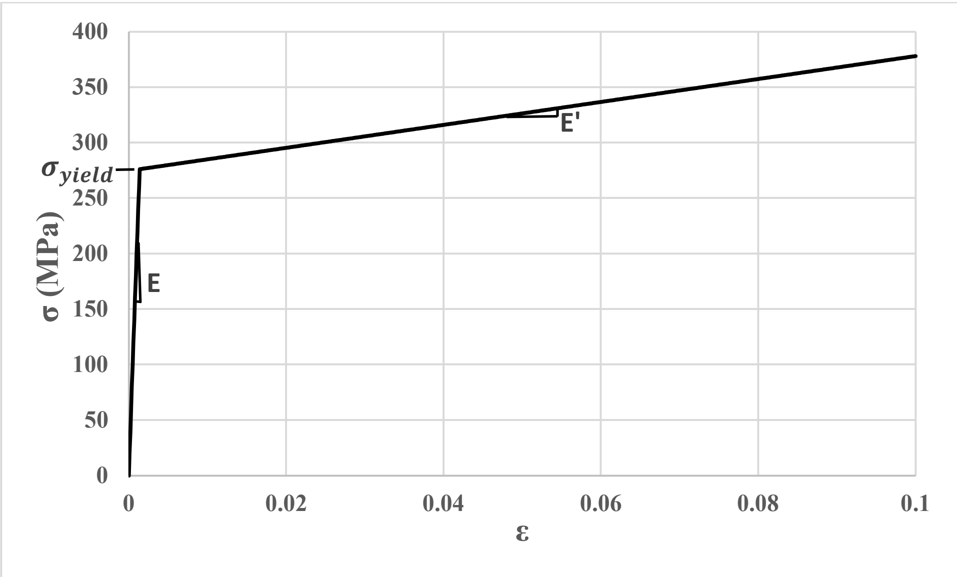

Figure 5.1. Stress-Strain curve of steel.

For explicit analyses, the steel density was taken as 8 g/cm^3.

5.1.2. Geometry of the Problem

The bearing consists of three layers of rubber pads and two layers of steel plates, which are placed in between the rubber pads. A small-scale bearing was considered. Overall thickness of the bearing is 11.5 mm. The geometry of the bearing is illustrated in Figure 5.2.

A layer of rubber pad has side dimensions of 50x50 mmxmm and thickness of 2.5 mm. These dimensions correspond to shape factor of 5. A steel layer has the side dimensions of 50x50 mmxmm and thickness of 2 mm.

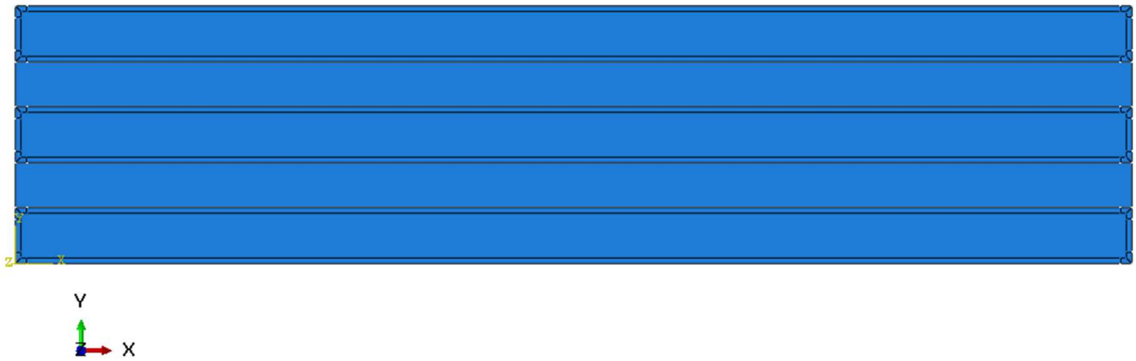

Figure 5.2. The geometry of the bearing (11.5x50x50 mmxmmxmm).

5.1.3. Mesh

Plane strain analysis of the steel-rubber bearing was conducted. For rubber pads, mesh consisted of quadrilateral, reduced integration, linear elements for static analyses with implicit integration and quasi-static analyses with explicit integration. Linear elements were used since they are more efficient in contact. Hybrid elements were considered for static analysis with implicit integration.

For steel plates, mesh consisted of quadrilateral, linear elements for static analyses with implicit integration; and quadrilateral, reduced integration, linear elements for quasi-static analyses with explicit integration. The mesh convergence study for a steel plate is presented in Appendix-B. The mesh structure for the bearing is shown in Figure 5.3. The elements used for predictions are as following:

- For rubber pads, CPE4RH in analyses with implicit time integration
- For rubber pads, CPE4R in analyses with explicit time integration
- For steel plates, CPE4 in analyses with implicit time integration
- For steel plates, CPE4R in analyses with explicit time integration

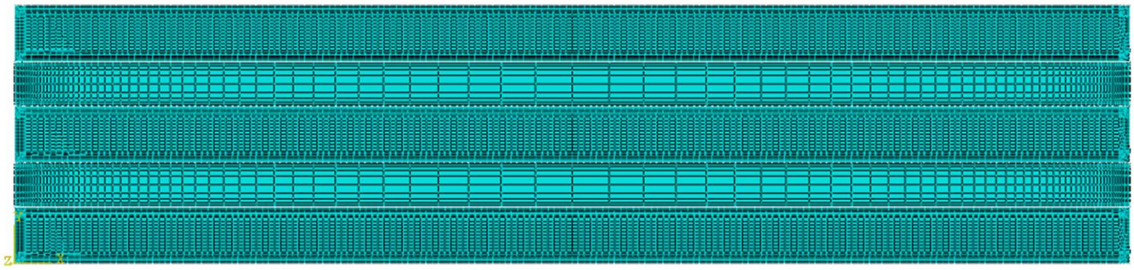

Figure 5.3. The mesh for the steel-rubber bearing. Total number of elements: 22376.

5.1.4. Loading and Boundary Conditions

The bearing was subjected to either compression load or combination of compression and shear loads. The loads were applied through an analytical rigid body. The load was applied as displacement.

Compression stress of 12 MPa was considered in analyses for global response. Compression stresses of 12 MPa and 18 MPa were considered in analyses for local response. For the geometry used in this study, 12 MPa and 18 MPa correspond to total loads of 30000 N and 45000 N, respectively. Table 5.1 shows the applied vertical displacement for different shape factors and bulk modulus to shear modulus ratios.

Table 5.1. Total load and the corresponding vertical displacements in the FE models of the composite bearing.

SF	K_0/μ_0	Total Load (N)	Vertical Displacement (mm)
5	10	30000	-2.7844
	20	30000	-1.6056
	50	30000	-0.7655
	100	30000	-0.4517
	2000	30000	-0.1255
	∞	30000	-0.1074
	20	45000	-2.3145
	50	45000	-1.1059
	100	45000	-0.6568
	2000	45000	-0.2007

For shear loading the applied horizontal displacement is 7.5 mm which corresponds to shear strain equal to 1.

The boundary conditions were defined through reference points of the two rigid bodies as presented in Figure 5.4. For both compression and shear, all displacement components were set to zero at “RP_1”. For compression, horizontal displacement component was set to zero at “RP_2” while for shear vertical displacement component was set to zero at “RP_2”. Vertical and horizontal displacements were applied at “RP_2” for compression and shear, respectively.

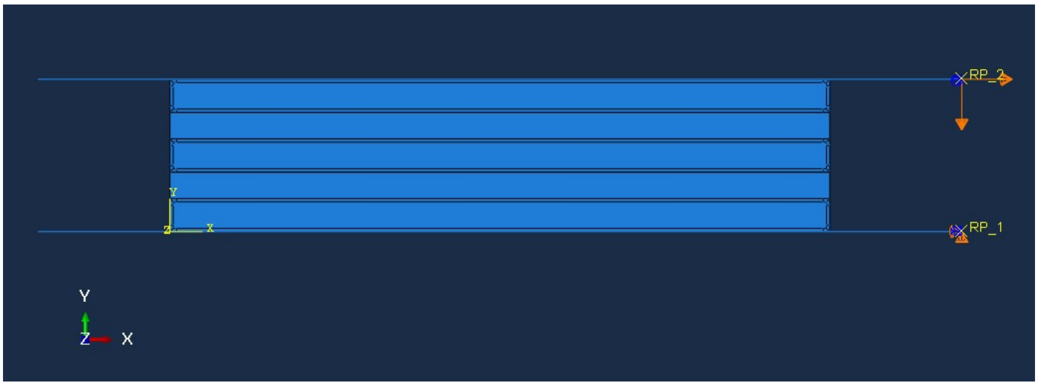

Figure 5.4. The boundary conditions for the bearing.

Two different interface properties were defined between the bearing and rigid bodies. First case is a tie constraint which was applied in order to characterize the bearing as bounded. For the second case, contact was modeled. In particular, tangential behavior with friction and normal behavior with hard contact were defined. For friction formulation, penalty method was used. The friction coefficient was selected as μ = 0.3 [9]. Unless otherwise specified, results are presented for tie constraint.

For either of the above models, at the bearing-rigid body interface contact was defined between lateral surfaces of rubber pads and rigid bodies. Contact was also defined between lateral surfaces of rubber pads and lateral surfaces of steel plates. For normal behavior, hard contact was defined. For implicit analysis, the constraint was enforced via Augmented Lagrange Method, while for the explicit analysis, kinematic constraint enforcement method was employed. Tangential behavior was defined as frictionless. Finally, tie constraint was defined at rubber-steel interfaces.

5.2. Results

The finite element predictions were evaluated in terms of global as well as local responses. Quantities representative of the global response were selected as:

- Vertical force
- Vertical stiffness
- Horizontal force
- Horizontal stiffness

Static analyses with implicit time integration and quasi-static analyses with explicit integration were performed. The effects of following parameters on the global response were investigated.

- Rubber Compressibility
- Loading Velocity

Quantities representative of the local response were selected as:

- Normal stress at top of bearing
- Maximum tensile stress in rubber
- Maximum Mises stress in steel
- Horizontal normal stress at the rubber-steel interface

For static analyses with implicit time integration, the effects of following parameters on the local response were investigated.

- Loading Type (Compression only vs. combination of compression and shear)
- Boundary Type (Bounded vs. frictional)
- Compression Load Magnitude
- Compressibility

5.2.1. Results for Global Response

In this section, the results of analyses in regard to vertical and horizontal behavior of the bearing are presented.

5.2.1.1. Results for Compressive Loading. The results presented in this section are for the steel-rubber bearing subjected to compression load only. The analyses were conducted with implicit and explicit time integrations.

Figures 5.5 and 5.6 show the deformed configurations of the bounded bearing and of the bearing with frictional boundary condition subjected to compression load. For the bounded bearing, element distortions are much more severe than for the bearing with frictional boundary condition. In the former, element distortions are mostly near the edges where rubber pads and rigid bodies are in contact. These distortions may cause stress concentration at the edges.

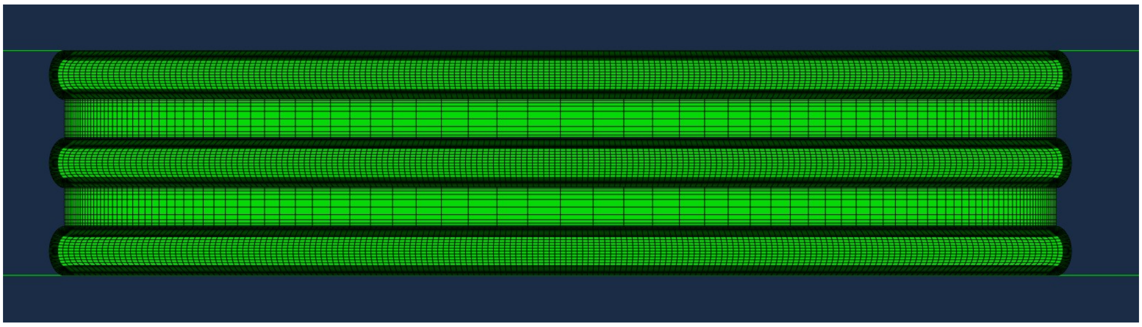

Figure 5.5. The deformed configuration of the bounded bearing under compression load only.

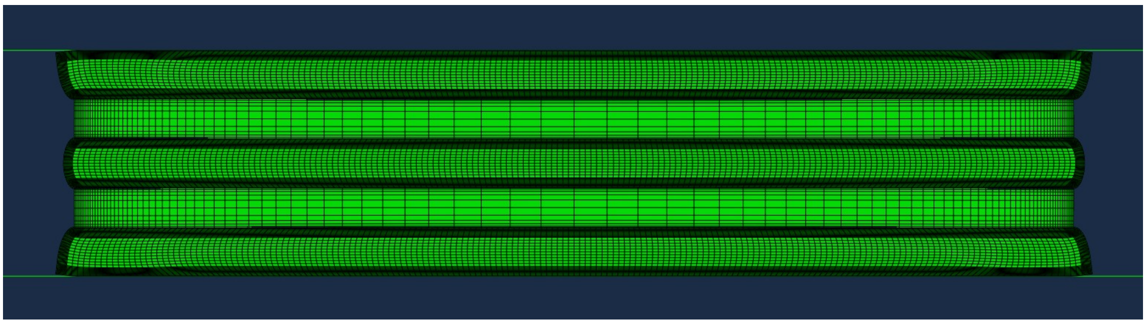

Figure 5.6. The deformed configuration of the bearing with frictional boundary condition under compression load only.

<u>5.2.1.1.1. Vertical Stiffness.</u> The vertical displacement of the bearing which is subjected to compression load of 30000 N was investigated for various bulk to shear stiffness ratios. The results are presented in Table 5.2 along with those obtained for one rubber pad presented in Chapter 3. It is concluded that at each compressibility level the vertical displacements obtained for bearing are about three times of those obtained for a single pad. This result is reasonable because the bearing consists of three layers of rubber pads. Furthermore, the results indicate that conducting finite element analysis of one layer of rubber pad is adequate to characterize the vertical behavior of a complete bearing model.

Table 5.2. Vertical displacements for the steel-rubber bearing and plain rubber pad.

SF	K_0/μ_0	**Total Load (N)**	**Steel-Rubber Bearing**	**Plain Rubber Pad**
			Vertical Displacement (mm)	**Vertical Displacement (mm)**
5	10	30000	-2.7844	-0.9255
	20	30000	-1.6056	-0.5343
	50	30000	-0.7655	-0.2549
	100	30000	-0.4517	-0.1503
	∞	30000	-0.1074	-0.0355

The vertical stiffness response of the steel-rubber bearing model at different rubber compressibility values is presented in Table 5.3 along with the results of plain rubber pad model. The vertical stiffness values of single pad analyses are almost three times higher than the stiffness values of bearing model. The vertical stiffness of the bearing at various rubber compressibility levels is shown in Figure 5.7 where results are normalized by the value of the incompressible case. Comparison of Figure 5.7 and Figure 3.13 shows that the effect of compressibility on vertical stiffness is nearly the same for both the bearing and one pad models.

Table 5.3. Vertical stiffness results for the steel-rubber bearing and plain rubber pad.

SF	K_0/μ_0	**Total Load (N)**	**Steel-Rubber Bearing**	**Plain Rubber Pad**
			Vertical Stiffness (N/mm)	**Vertical Stiffness (N/mm)**
5	10	30000	10774	32415
	20	30000	18685	56146
	50	30000	39190	117715
	100	30000	66420	199645
	∞	30000	279382	845592

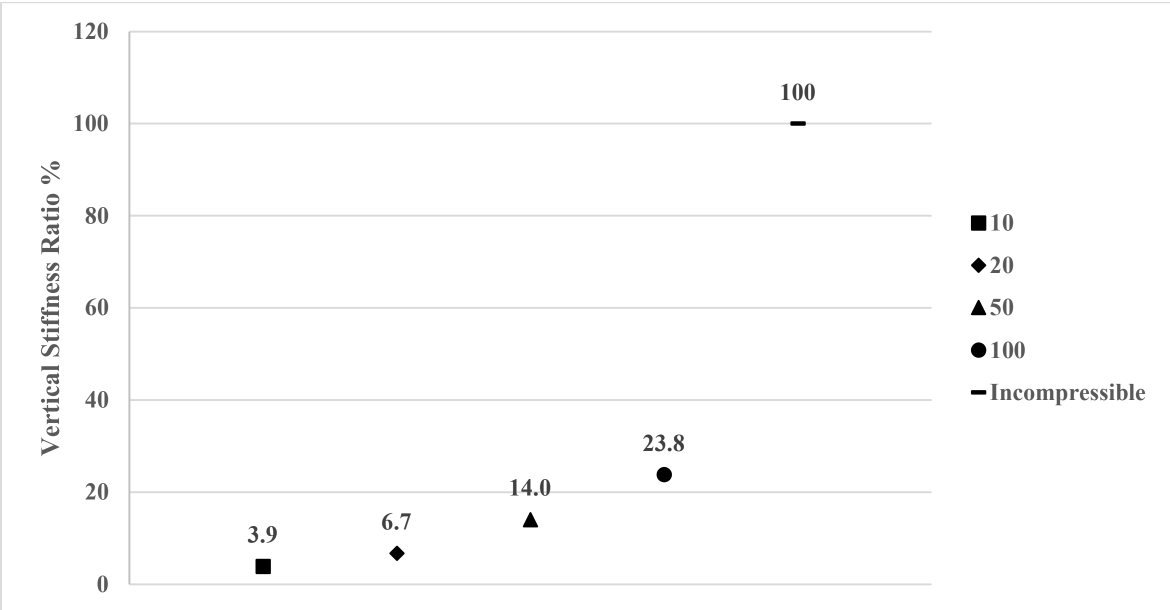

Figure 5.7. The results for vertical stiffness ratio for the different compressibility values of the bearing.

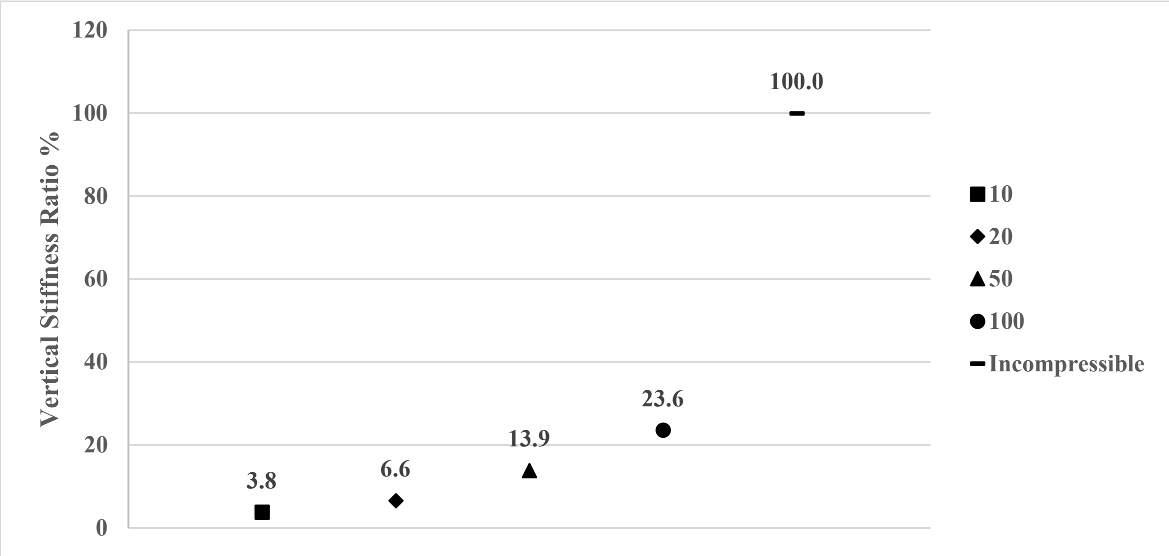

Figure 3.13. (Repeated) The static results for vertical stiffness ratio normalized with respect to the incompressible case for the different compressibility values for SF=5.

5.2.1.1.2. Explicit Time Integration. Quasi-static analyses with explicit time integration were performed to investigate the effects of loading rate and rubber compressibility on the vertical response of the bearing. The strain rates of 0.4/s and 2/s corresponding to frequencies of 0.1 Hz and 0.5 Hz, respectively, were selected for the analyses.

Table 5.4 shows the KE/IE ratios for the different velocities and compressibility values. According to the table, the KE/IE ratios for the strain rate of 2/s are significantly higher than the ratios for the strain rate of 0.4/s; therefore, for the strain rate of 2/s, analyses seem to be dynamic rather than quasi-static.

Table 5.4. KE/IE for the bearing subjected to compression load.

Strain Rate	K_0/μ_0	Duration (s)	KE/IE %
2/s	20	0.107	11.8
	100	0.030	26.5
0.4/s	20	0.535	0.5
	100	0.151	3.5

Figure 5.8 and Figure 5.9 show vertical force and vertical displacement responses at different strain rates for $K_0/\mu_0 = 100$ and $K_0/\mu_0 = 20$, respectively.

Regarding the effect of velocity, both figures indicate that the solution with explicit time integration significantly diverges from the static solution with implicit time integration for the analysis at higher strain rate (2/s). This also proves that the analyses with strain rate of 2/s are dynamic instead of quasi-static.

Regarding the effect of compressibility, for strain rate of 0.4/s, relatively better results are obtained for $K_0/\mu_0 = 20$. It is, therefore, concluded that quasi-static solutions for a given loading velocity become closer to static solutions with increasing compressibility.

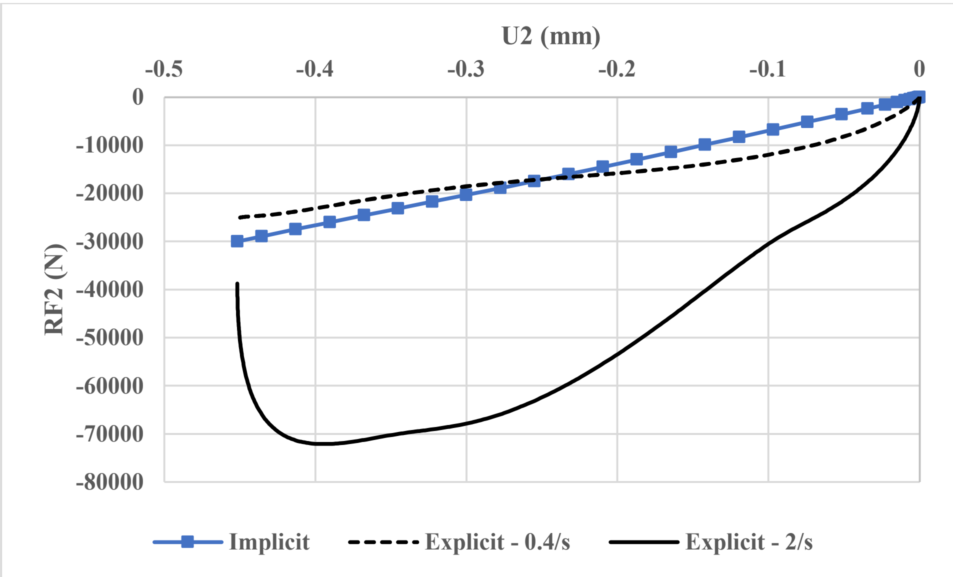

Figure 5.8. The static and quasi-static results for vertical force for the different velocities for $K_0/\mu_0 = 100$.

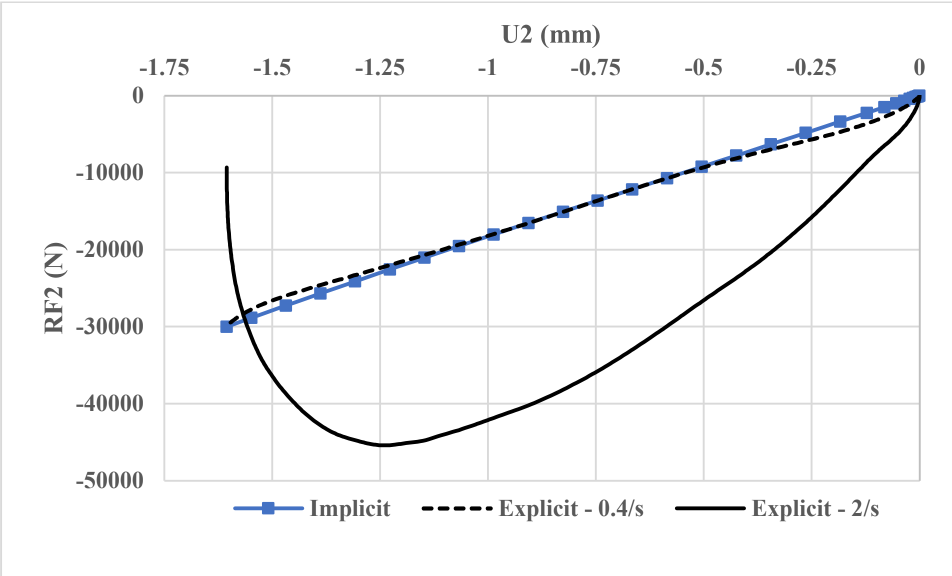

Figure 5.9. The static and quasi-static results for vertical force for the different velocities for $K_0/\mu_0 = 20$.

<u>5.2.1.2. Results for Combined Compressive and Shear Loading.</u> The results presented in this section are for the steel-rubber bearing subjected to combination of compression and shear loads. The analyses were conducted with implicit and explicit time integrations.

Figures 5.10 and 5.11 show the deformed configurations of the bounded bearing and of the bearing with frictional boundary condition subjected to combination of compression and shear loads, respectively. For the bounded bearing, element distortions are more severe than for the bearing with frictional boundary condition. In particular, near the edges where rubber pads and rigid bodies are in contact. These distortions cause stress concentrations.

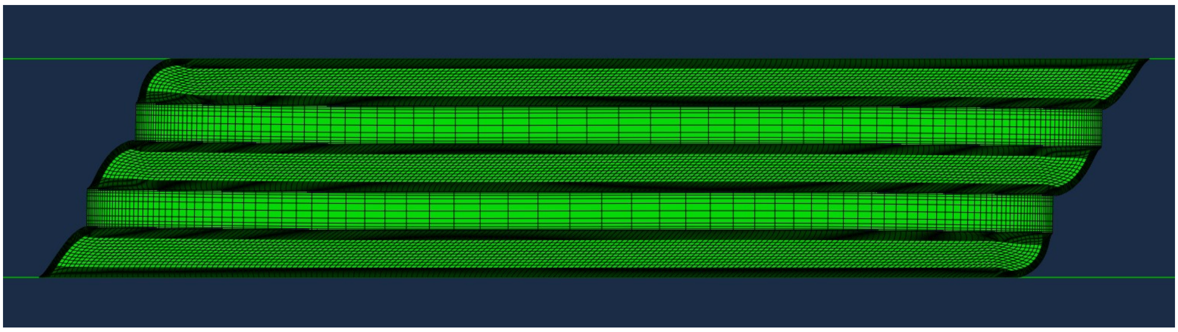

Figure 5.10. The deformed configuration of the bounded bearing under the combination of compression and shear loads.

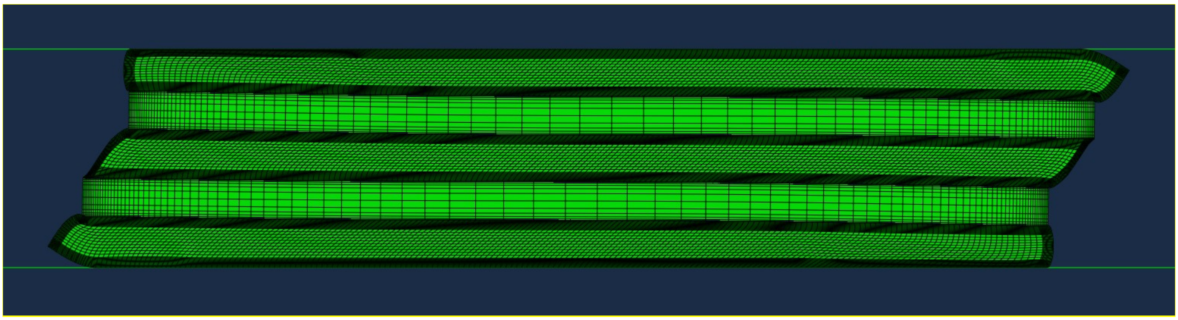

Figure 5.11. The deformed configuration of the bearing with frictional boundary condition under the combination of compression and shear loads.

5.2.1.2.1. Horizontal Stiffness. The horizontal stiffness response of the steel-rubber bearing at different rubber compressibility values is presented in Table 5.5 along with the results of plain rubber pad. In the table, the stiffness value of the bearing with $K_0/\mu_0 = 10$ is not presented due to lack of convergence in the analysis. The horizontal stiffness values of single pad are 3.09-3.22 times higher than the stiffness values of the bearing. The bearing consists of three layers of rubber pads. It is concluded that conducting finite element analysis of one layer of rubber pad may characterize horizontal behavior of a complete bearing with possible relative difference of 3.0-7.3%. The difference increases as compressibility increases except for the incompressible case.

Table 5.5. Horizontal stiffness results for the steel-rubber bearing and plain rubber pad.

SF	K_0/μ_0	Shear Strain	Steel-Rubber Bearing	Plain Rubber Pad	% Difference
			Horizontal Stiffness (N/mm)	Horizontal Stiffness (N/mm)	
5	10	1	-	3837	-
	20	1	690	2222	7.3
	50	1	597	1867	4.3
	100	1	591	1827	3.0
	∞	1	661	2126	7.2

5.2.1.2.2. Explicit Time Integration. Quasi-static analyses with explicit time integration were done to evaluate the effects of loading rate and rubber compressibility on the horizontal response of the bearing. Table 5.6 presents the KE/IE ratios for the different velocities and compressibility values. It is observed that the KE/IE ratios for the strain rate of 2/s are significantly higher than those for the strain rate of 0.4/s, as it was also observed in Table 5.4. Therefore, for the strain rate of 2/s, analyses become dynamic.

Table 5.6. KE/IE for the bearing subjected to the combination of compression and shear loads.

Strain Rate	K_0/μ_0	**Duration (s)**	**KE/IE %**
2/s	20	0.5	10.7
	100	0.5	12.6
0.4/s	20	2.5	0.3
	100	2.5	0.8

Figure 5.12 and Figure 5.13 present horizontal force and horizontal displacement responses of the bearing at different strain rates for $K_0/\mu_0 = 100$ and $K_0/\mu_0 = 20$, respectively.

Regarding loading velocity effect, predictions with explicit time integration extremely diverges from the predictions with implicit time integration and has significant noise for the analysis at higher strain rate (2/s). As a conclusion, the analyses with strain rate of 2/s are dynamic instead of quasi-static.

Regarding the effect of compressibility, for strain rate of 0.4/s, slightly better solution is obtained for $K_0/\mu_0 = 20$. This shows that quasi-static solutions for a given loading velocity become closer to static solutions with increasing compressibility.

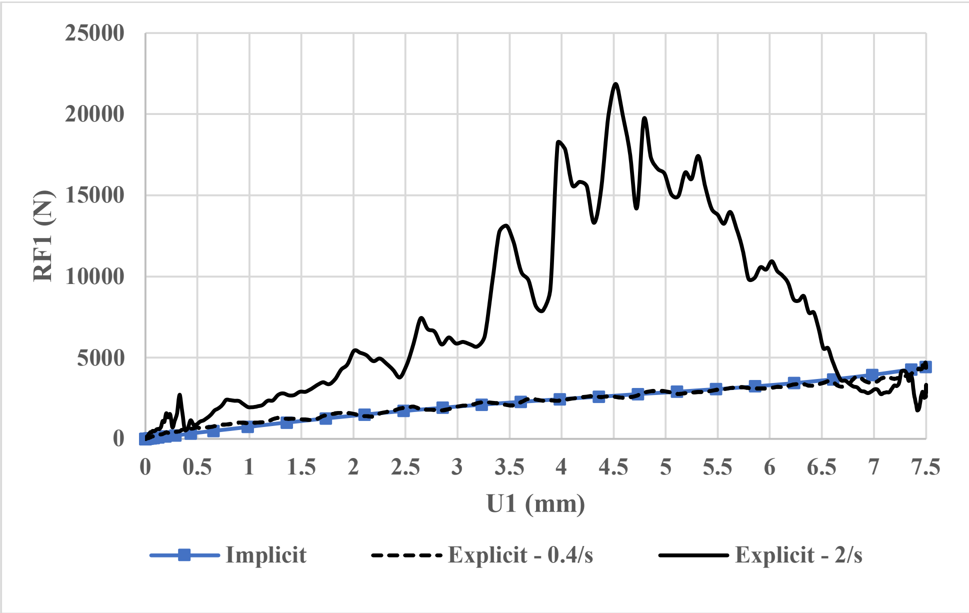

Figure 5.12. The static and quasi-static results for horizontal force for the different velocities for $K_0/\mu_0 = 100$.

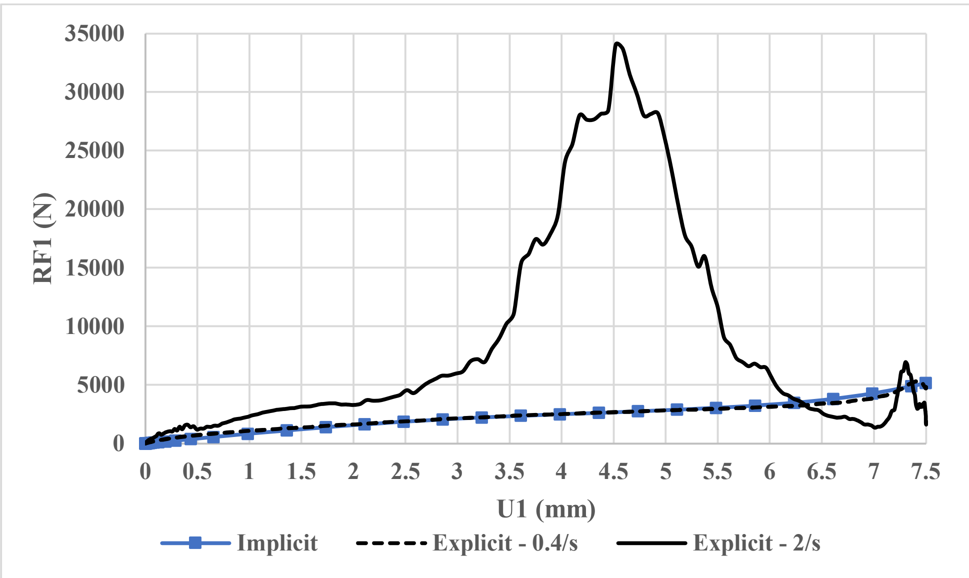

Figure 5.13. The static and quasi-static results for horizontal force for the different velocities for $K_0/\mu_0 = 20$.

5.2.1.3. Conclusions of the Problem. The following are concluded based on the results presented in Section 5.2.1.

- Finite element predictions of a one-layer rubber pad sufficiently highlight vertical response of a composite bearing model.
- Vertical stiffness of the composite bearing can be calculated based on the vertical stiffness of the single-rubber pad.
- The effect of rubber compressibility on vertical stiffness is nearly the same for both a rubber-steel bearing and a one-layer rubber pad. In the predictions of the vertical stiffness, the use of lower K_0/μ_0 for rubber causes significant error as compared to the solution for an incompressible material behavior.
- For high loading rate (2/s), solutions with explicit time integration are considered as dynamic instead of quasi-static for both vertical and horizontal responses and predictions for the high loading rate significantly diverge from static solutions with implicit time integration. This can be deduced based on the KE/IE ratios which for the high loading rate are significantly higher than those for the lower loading rate of 0.4/s.
- For vertical and horizontal responses, results of quasi-static analysis become closer to static solutions as compressibility increases for lower loading rate (0.4/s).
- Conducting finite element analysis of one layer of rubber pad may characterize horizontal behavior of the composite bearing with possible relative difference in the range of 3.0-7.3%.

5.2.2. Results for Local Response

In this section, the stress field predictions in rubber pads and in steel plates of the bearing are presented. For the rubber, compressive stress at top of the bearing and maximum tensile stress in rubber were evaluated. For the steel, maximum Mises stress, plastic deformation, and horizontal normal stress at the steel-rubber interface were studied. Implicit time integration was used for analyses.

For rubber, the ratio of initial bulk modulus to initial shear modulus was considered as 2000. Additionally, the ratios of 20, 50, 100, and incompressible case were considered for bearing models in the analysis for maximum Mises stress in steel.

5.2.2.1. Local Response of Rubber. The results presented in this section are for the steel-rubber bearing with $K_0/\mu_0 = 2000$. Either compression load only or combination of compression and shear loads were applied to the model. Compressive stress at top of the bearing and maximum tensile stress in rubber pads were evaluated. Effects of loading type, boundary type and vertical load were studied.

5.2.2.1.1. Compressive Stress at Top of the Bearing. Compressive stresses at top of the bearing with $K_0/\mu_0 = 2000$ under either compression load (45000 N) or the combination of compression and shear loads were evaluated. The results of both loading types are presented for both bounded and frictional contact models through the length of bearing in Figures 5.14 and 5.15. The results are normalized by the average compressive stress, $\sigma_{avg} = -18$ MPa.

Based on Figure 5.14, for the case of compression only, parabolic behavior of compressive stress is observed with maximum value at the middle of the length and with the values close to zero at both ends of the length where mild stress concentration is present because of the effect of bounded model. For the case of the combination of compression and shear loads, significant stress concentration is present at the end close to $x = 0$ which is on the opposite side of applied shear load direction. Compressive stress approaches to zero at the end close to $x = 50$ which is on the same side of applied shear load direction. Compared to the case of compression only, considerably high compressive stress values were observed between $x = 0$ and $x = 43$ in the case of combined loads.

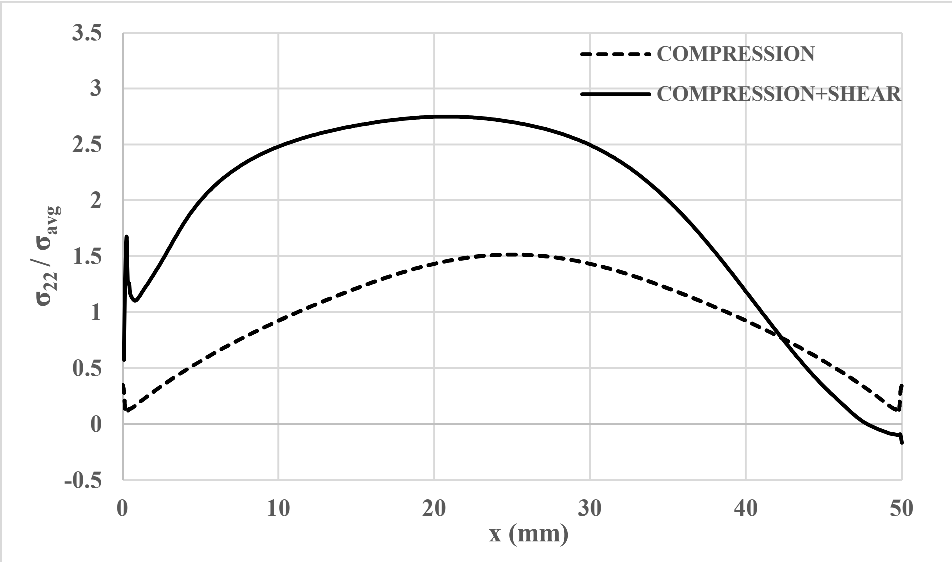

Figure 5.14. The results of normalized compressive stress at top of the bearing considering the effect of loading type for the bearing with bounded boundary type.

According to Figure 5.15, for the case of compression only, parabolic behavior of compressive stress is observed with maximum value at the middle of the length and with the values close to zero at both ends of the length where no stress concentration exists. For the case of the combined loads, mild stress concentration is present at the end close to $x = 0$. Compressive stress approaches to zero at the end close to $x = 50$. Compared to the case of compression only, high compressive stress values were obtained between $x = 5$ and $x = 25$ in the case of the combined loads. Moreover, the ratio of the compressive stress to the average compressive stress observed in the case of only compression load is similar (around 1.5 at the maximum values) to the ratio reported in [9], therein Figure 3.

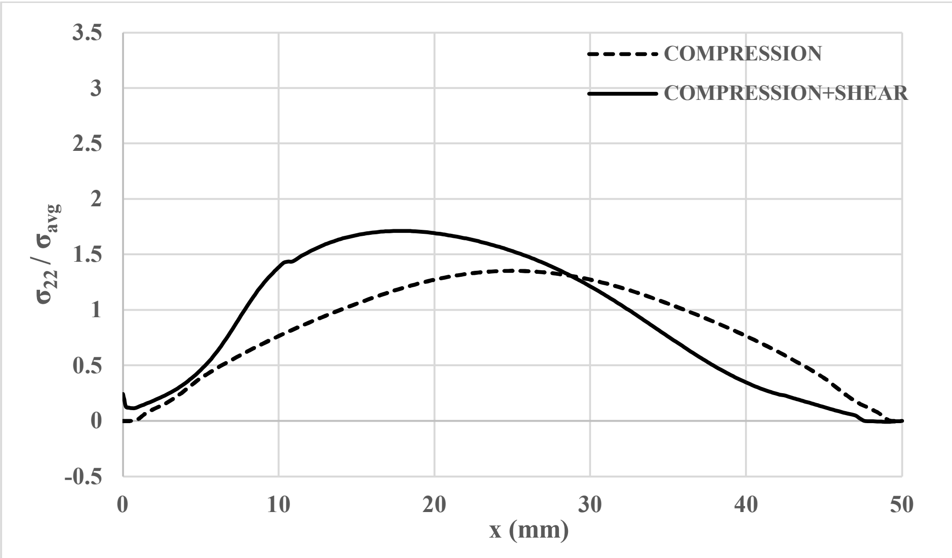

Figure 5.15. The results of normalized compressive stress at top of the bearing considering the effect of loading type for the bearing with friction boundary type.

Effects of boundary type between the bearing and rigid bodies are compared in Figure 5.16 for the case of compression load only and in Figure 5.17 for the case of the combined loads.

For the case of compression load only, it is concluded that the compressive stress values throughout the length are higher (max.12%) for the bearing with bounded contact than for the bearing with frictional contact. Moreover, the stress concentration observed at both ends of the model with bounded contact is not present for the model with frictional contact. The cause for the stress concentration was highlighted while discussing Figures 5.5 and 5.6.

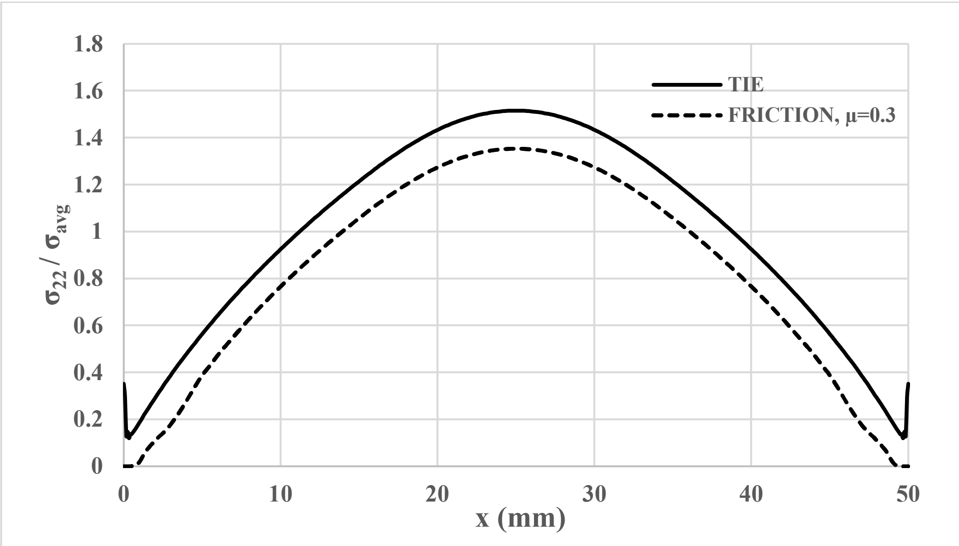

Figure 5.16. The results of normalized compressive stress at top of the bearing under compression load only for different boundary types.

For the case of the combined loads, a similar trend is observed for both boundary types. However, compressive stress values along most of the parts of the length are significantly higher (almost 60% higher at $x = 20$ where the compressive stress is maximum for bounded type of boundary) for bounded type of boundary. In addition, no stress concentration exists at both ends of the model with frictional contact. The deformed configurations for both boundary types are presented in Figures 5.10 and 5.11.

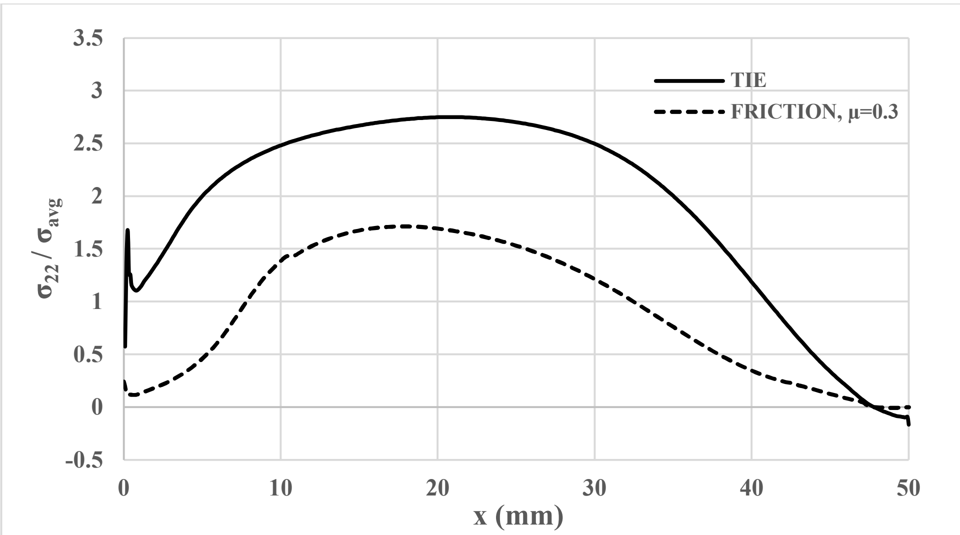

Figure 5.17. The results of normalized compressive stress at top of the bearing under the combination of compression and shear loads for different boundary types.

5.2.2.1.2. Maximum Tensile Stress in Rubber. Maximum tensile stress in rubber pads in the bearing model with $K_0/\mu_0 = 2000$ was evaluated for the combination of vertical and horizontal loads. Vertical loads were applied as 30000 N and 45000 N to study the effect of compression load magnitude on tensile stress in rubber pads. Figures 5.18 and 5.19 show normal stress distribution in vertical direction for both loads. It is observed that tensile stresses increase towards the edges of rubber pads. Furthermore, for 30000 N vertical load, the maximum tensile stress in rubber was obtained as 4.76 MPa, while for 45000 N, the maximum tensile stress in rubber was obtained as 4.28 MPa. As a conclusion, maximum tensile stress in rubber decreases with an increase in compression load magnitude.

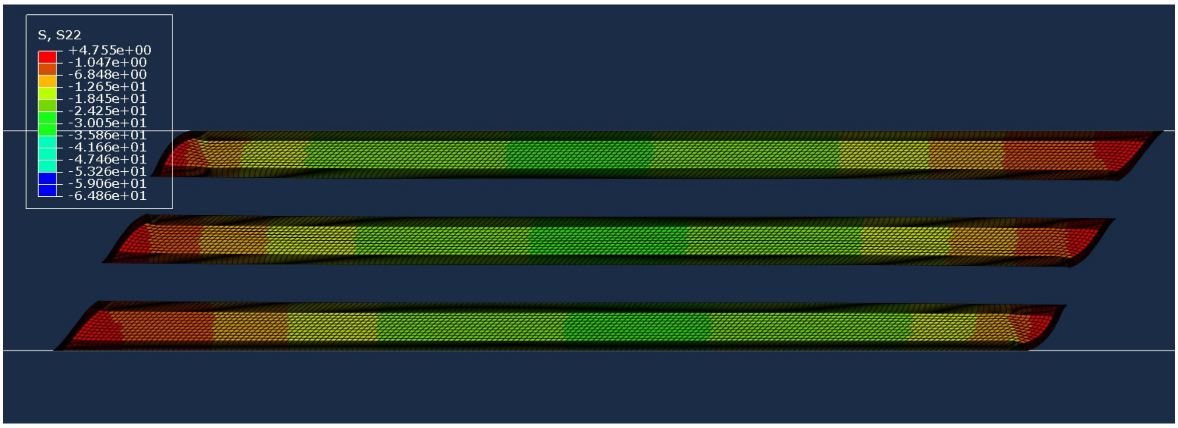

Figure 5.18. Normal stress distribution in vertical direction in rubber pads for the model subjected to vertical load of 30000 N.

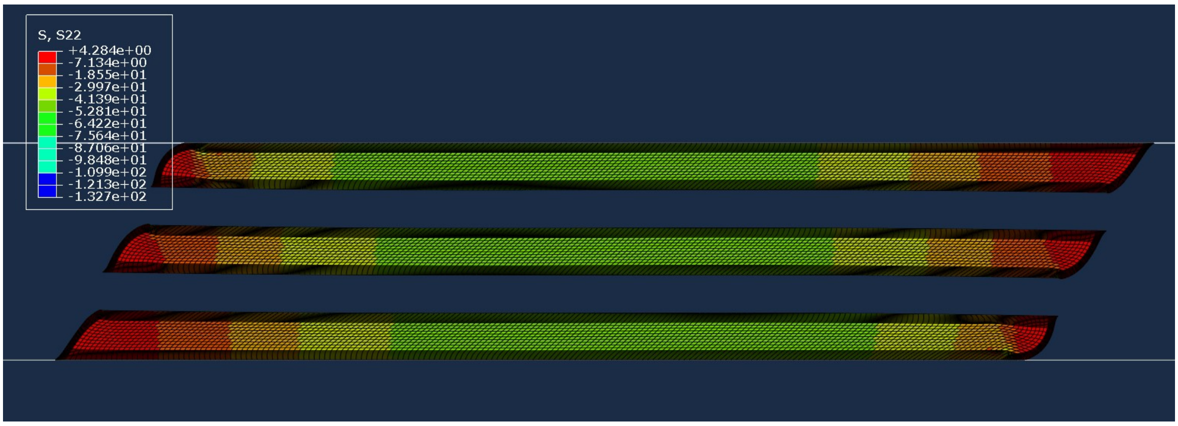

Figure 5.19. Normal stress distribution in vertical direction in rubber pads for the model subjected to vertical load of 45000 N.

5.2.2.2. Local Response of Steel. The results of the bearing with $K_0/\mu_0 = 2000$ either under compression load or under combination of compression and shear loads are presented for the steel plates. Maximum Mises stress and plastic deformation in steel, and horizontal normal stress at the steel-rubber interface were examined. The effect of vertical load magnitude was evaluated, and various interface models were considered.

5.2.2.2.1. Maximum Mises Stress and Plastic Deformation in Steel. Maximum Mises stresses within steel plates of the bearing subjected to combined compression and shear load were calculated for various rubber compressibility values. The maximum Mises stress values in steel for the applied vertical loads (30000 N and 45000 N) and for different compressibility values are given in Table 5.7. The stress values were obtained at integration points in steel. It is concluded that at each compressibility, maximum Mises stress increases as vertical load increases. Furthermore, at a given load, maximum Mises stress values seem to increase with increasing compressibility. For the case of $K_0/\mu_0 = \infty$ for vertical load of 30000 N and that of $K_0/\mu_0 = 2000$ for vertical load of 45000 N are exceptions, the former possibly due to use of hybrid formulation, the latter possibly due to use of non-converged mesh. The incompressible case for vertical load of 45000 N is not given in the table due to lack of convergence.

Table 5.7. Maximum Mises Stress (MPa).

K_0/μ_0	**Total Vertical Load (N)**	
	30000	**45000**
∞	202.1	-
2000	190.8	276.4
100	194.8	267.9
50	202.9	273.2
20	209.5	276.1

Plastic deformation within steel was observed for the case with Mises stress values exceeding the yield stress, $\sigma_{yield} = 276$ MPa. Figure 5.20 shows Mises stress distribution and Figure 5.21 shows plastic deformation locations for $K_0/\mu_0 = 2000$. Figure 5.21 highlights that plastic deformation starts near the rubber-steel interface located at the mid-height and spreads further along the interface.

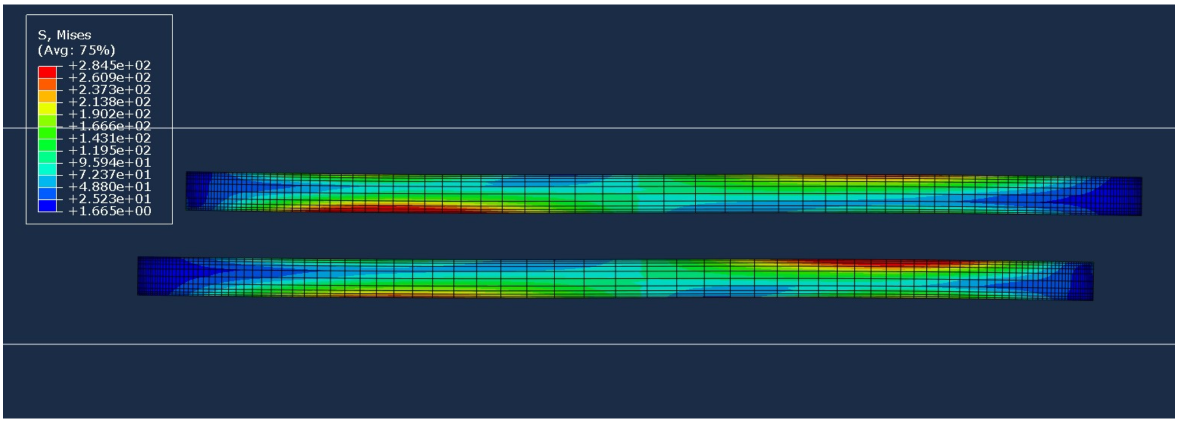

Figure 5.20. Mises stress distribution with $K_0/\mu_0 = 2000$ for the case of compression force of 45000 N.

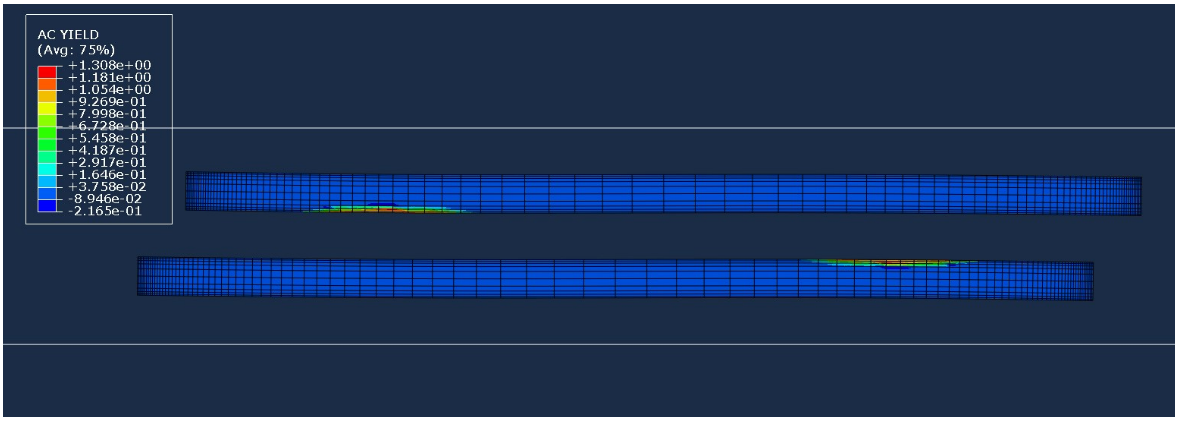

Figure 5.21. Plastic deformation locations of the model with $K_0/\mu_0 = 2000$ for the case of compression force of 45000 N.

<u>5.2.2.2.2. Horizontal Normal Stress at Interface with Rubber.</u> Horizontal normal stress at different steel-rubber interfaces was evaluated for the bearing with $K_0/\mu_0 = 2000$ subjected to either compression force or the combination of compression and shear forces. The compression force was applied as 45000 N for both loading cases. Two interfaces were selected. Interface_1 shown in Figure 5.22, is located between the bottom rubber pad and the steel plate near to bottom. Interface_2 shown in Figure 5.23, is located between the rubber pad in the middle of the bearing and the steel plate near to bottom.

Figure 5.22. Interface_1.

Figure 5.23. Interface_2.

Figure 5.24 shows horizontal normal stress results in steel through the length of Interface_1 and Interface_2 for all loading types. It is concluded that for both interfaces the results are the same for compression load only. However, for the case of the combination of compression and shear loads, the stress distribution throughout the length is different for two interfaces. These results are qualitatively similar to those presented in Figure 4 of [9], even though the applied compression and shear loads are different. Plastic deformation is observed on Interface_2 around $x = 40$ for combined loading case. This can also be observed in Figure 5.25, where horizontal normal stress contour plots are shown.

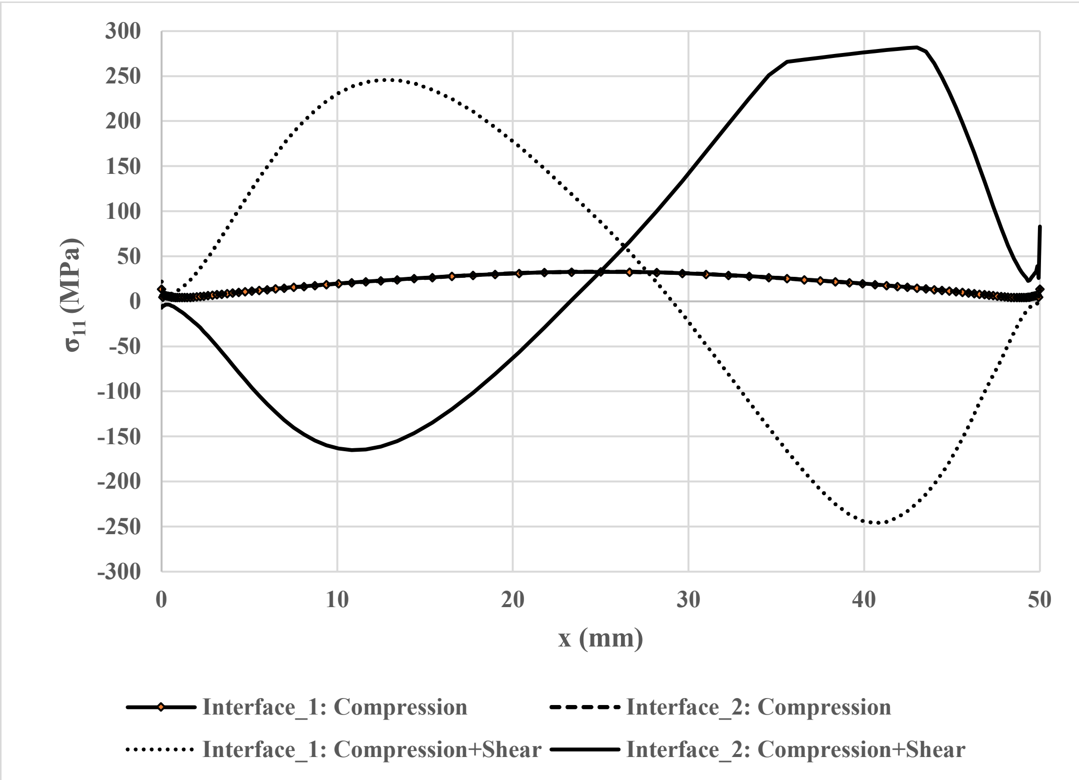

Figure 5.24. The horizontal normal stress for the different loading cases and for the different interfaces.

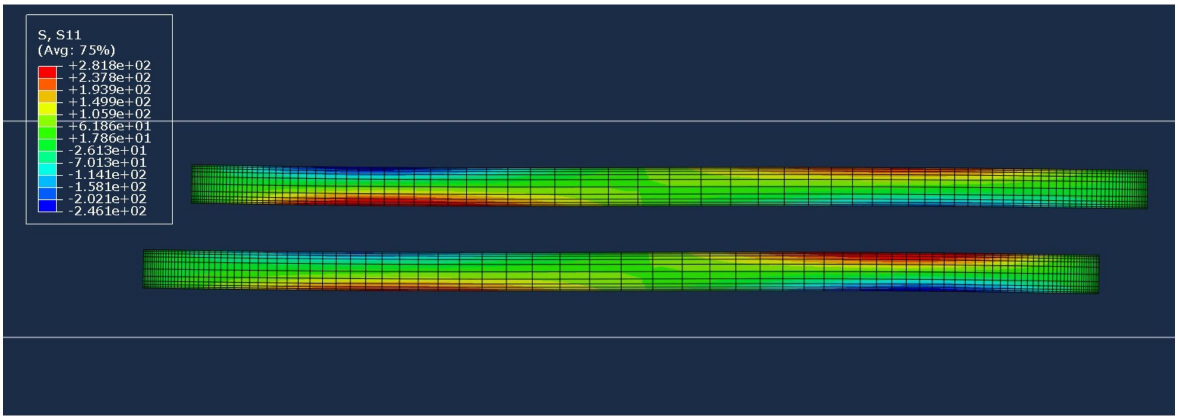

Figure 5.25. The horizontal normal stress contour plot for the case of the combination of compression and shear forces.

5.2.2.3. Conclusions of the Problem. The following are concluded based on the results presented in Section 5.2.2.

- For bounded boundary type, combined loads resulted in considerably higher compressive stresses along most of the length as compared to compression load only.

- For frictional boundary type, the difference between compressive stresses from compression only and combined loads was less and was limited to the half section of the length (between $x = 5$ and $x = 25$).
- For the case of compression load only, the bearing with bounded boundary type exhibits mildly higher (12% as maximum) compressive stress values along the length than the bearing with frictional boundary type. For the case of combined loads, this value gets considerably higher (60% at maximum value of the case of bounded boundary condition).
- Compressive stress concentration was observed at ends of the bearing with bounded boundary type while no stress concentration was present for the bearing with frictional boundary type.
- The maximum tensile stress in rubber decreases with an increase in compression load magnitude.
- Maximum Mises stress increases as compression load magnitude increases for each K_0/μ_0.
- Maximum Mises stress in steel increases with an increase in rubber compressibility. There are some exceptions to this trend, which need further modeling studies.
- Horizontal normal stress distribution differs according to interface locations for the case of combined loads, while remains the same for the case of compression load only.

6. CONCLUSION

In this thesis, finite element modeling of plain elastomer bearings and of composite bearings is constructed. The global and local responses of bearings subjected to either compression load or combination of compression and shear loads were investigated. Implicit time integration for static analysis and explicit time integration for quasi-static analysis were used. The effects of constitutive model of rubber, compressibility of rubber, shape factor of the bearing on global response were studied in static analysis. In addition, the effects of magnitude of the applied load and friction on local response of the bearing were studied in static analysis. For the explicit analysis, the effects of the applied loading rate and compressibility of rubber on the predictions were determined. A few dynamic analyses with implicit time integration were performed to check the solution quality of explicit time integration.

The results of the study highlights that for the strain rates considered in the analysis, viscoelasticity does not affect vertical response and mildly affects horizontal response of the bearing. The effect of viscoelasticity decreases with increasing compressibility level. Since the hyperelastic model was calibrated to instantaneous material data, viscoelastic solutions get closer to hyperelastic solutions as loading velocity increases. In the explicit analysis, viscoelasticity has no effect on the KE/IE ratio as compared to the KE/IE ratios with hyperelastic model predictions.

In an explicit analysis, as compressibility increases, KE/IE values decrease and results of quasi-static analysis become closer to static solutions. However, the use of high level of rubber compressibility results in significant difference in the global response analysis as compared to the solution for an incompressible material behavior. Therefore, particular attention needs to be given to the interpretation of explicit analysis results.

As shape factor (confinement) increases, both vertical and horizontal stiffness get higher. The effect of the shape factor on the vertical stiffness is much more pronounced than that on the horizontal stiffness. For all shape factors, nearly the same horizontal force is obtained up to shear strain of 0.5.

In an explicit analysis, KE/IE values decrease as rate of applied load decreases. For a plain elastomer bearing, predictions with explicit time integration at higher strain rate (2/s) mildly deviates from static solution with implicit time integration. However, for a rubber-steel composite bearing, predictions with explicit time integration at higher strain rate (2/s) significantly diverge from static solutions with implicit time integration.

Predictions of a one-layer rubber pad sufficiently highlight vertical response of a composite bearing model, while predictions of one-layer rubber pad may characterize horizontal behavior of the composite bearing within 3.0-7.3% difference.

Regarding local response, for the bounded bearing, combined loads resulted in considerably higher compressive stresses at top of the bearing as compared to compression load only. However, for frictional boundary type, the difference between compressive stresses from compression only and combined loads was less. Also, compressive stress concentration was observed at the bounded bearing edges while no stress concentration was present for the bearing with frictional boundary. Under combined loads, the maximum tensile stress in rubber decreases as compression load increases. Moreover, maximum Mises stress in steel increases as compression load magnitude increases and as rubber compressibility increases. Horizontal normal stress distribution at the rubber-steel interface changes as per interface location for the case of combined loads, while remains the same for the case of compression load only.

The computational approaches presented in this thesis may be applied to the analysis of isolators for buildings and bridges. The hyperelastic material model used in the thesis is valid up to shear strain of 1. It can be improved in future studies if it is intended to explore a bearing response for larger horizontal displacements which correspond to higher shear strain levels. Global response of bearings may be studied considering frictional interface properties defined between top and bottom surfaces of bearings and rigid bodies. Dynamic analysis of bearings with implicit time integration may be further investigated. Also, future studies may be focused on mechanical response of a bearing subjected to cyclic loads.

REFERENCES

1. Kelly, J. M. and D. A. Konstantinidis, *Mechanics of Rubber Bearings for Seismic and Vibration Isolation*, John Wiley & Sons, London, UK, 2011.

2. Quaglini, V., P. Dubini, and G. Vazzana, “Experimental Assessment of High Damping Rubber Under Combined Compression and Shear”, *Journal of Engineering Materials and Technology*, Vol. 138(1), p. 011002, 2016.

3. *SIMULIA Inc. ABAQUS 6.14 Documentation,* 2014.

4. Amin, A. F. M. S., S. I. Wiraguna, A. R. Bhuiyan, and Y. Okui, “Hyperelasticity Model for Finite Element Analysis of Natural and High Damping Rubbers in Compression and Shear”, *Journal of Engineering Mechanics*, Vol. 132(1), pp. 54–64, 2006.

5. Amin, A. F. M. S., A. R. Bhuiyan, T. Hossain, and Y. Okui, “Nonlinear Viscosity Law in Finite-Element Analysis of High Damping Rubber Bearings and Expansion Joints”, *Journal of Engineering Mechanics*, Vol. 141(6), p. 04014169, 2015.

6. Milani, G. and F. Milani, “Stretch-Stress Behavior of Elastomeric Seismic Isolators with Different Rubber Materials: Numerical Insight”, *Journal of Engineering Mechanics*, Vol. 138(5), pp. 416–429, 2012.

7. Amin, A. F. M. S., M. S. Alam, and Y. Okui, “An Improved Hyperelasticity Relation in Modeling Viscoelasticity Response of Natural and High Damping Rubbers in Compression: Experiments, Parameter Identification and Numerical Verification”, *Mechanics of Materials*, Vol. 34, pp. 75–95, 2002.

8. Yurdabak, V., *Explicit Methods in Quasi-Static Analysis of Rubber-Like Materials*, M. Sc. Thesis, Boğaziçi University, 2017.

9. Hamzeh, O. N., J. L. Tassoulas, and E. B. Becker, “Behavior of Elastomeric Bridge Bearings: Computational Results”, *Journal of Bridge Engineering*, Vol. 3(3), pp. 140–146, 1998.

10. Salomón, O., S. Oller, and A. Barbat, “Finite Element Analysis of Base Isolated Buildings Subjected to Earthquake Loads”, *International Journal for Numerical Methods in Engineering*, Vol. 46, pp. 1741–1761, 1999.

11. Gajewski, M., R. Szczerbab, and S. Jemioloa, “Modelling of Elastomeric Bearings with Application of Yeoh Hyperelastic Material Model”, *Procedia Engineering*, Vol. 111, pp. 220–227, 2015.

12. Nguyen, H. H., and J. L. Tassoulas, “Directional Effects of Shear Combined with Compression on Bridge Elastomeric Bearings”, *Journal of Bridge Engineering*, Vol. 15(1), pp. 73–80, 2010.

13. Kalfas, K. N., S. A. Mitoulis, and K. Katakalos, “Numerical Study on the Response of Steel-Laminated Elastomeric Bearings Subjected to Variable Axial Loads and Development of Local Tensile Stresses”, *Engineering Structures*, Vol. 134, pp. 346–357, 2017.

14. Yeoh, O. H., “Some Forms of the Strain Energy Function for Rubber”, *Rubber Chemistry and Technology*, Vol. 66, pp. 754–771, 1993.

15. International Organization for Standardization (ISO), *Elastomeric Seismic-Protection Isolators-Part 2: Applications for Bridges*, Standard No. ISO 22762-2:2018, 2018.

16. International Organization for Standardization (ISO), *Elastomeric Seismic-Protection Isolators-Part 3: Applications for Buildings*, Standard No. ISO 22762-3:2018, 2018.

17. International Organization for Standardization (ISO), *Elastomeric Seismic-Protection Isolators-Part 1: Test Methods*, Standard No. ISO 22762-1:2018, 2018.

18. Constantinou, M. C., A. S. Whittaker, Y. Kalpakidis, D. M. Fenz, and G. P. Warn, "Performance of Seismic Isolation Hardware under Service and Seismic Loading", Multidisciplinary Center for Earthquake Engineering Research, State University of New York at Buffalo, Buffalo, NY, Technical Report No. MCEER-07-0012, 2007.

19. Markou, A. A., N. D. Oliveto, and A. Athanasiou, "Modeling of High Damping Rubber Bearings", In: Sextos A., and G. Manolis (eds), *Dynamic Response of Infrastructure to Environmentally Induced Loads*, Vol. 2, pp. 115–138, Springer, Cham, Switzerland, 2017.

APPENDIX A: MESH CONVERGENCE STUDY FOR RUBBER

The mesh convergence study was performed for the incompressible model with SF=5. The combination of compression and shear loads were applied. The compression load was applied as vertical displacement of -0.125 which corresponds to $\lambda = 0.95$. Also, shear load applied as horizontal displacement of 2.5 which corresponds to $\gamma = 1$. Implicit time integration was used. There are three different mesh structures evaluated for convergence studies. The first mesh structure has no partitions and is shown in Figure A.1. Its side edges were divided into 10 parts and its top and bottom edges were divided into 100 parts. The simulation with this model was not converged during the application of shear load. It was aborted by the software at 83% of the solution time. The reason of this problem is element distortions in the corners of rubber pad.

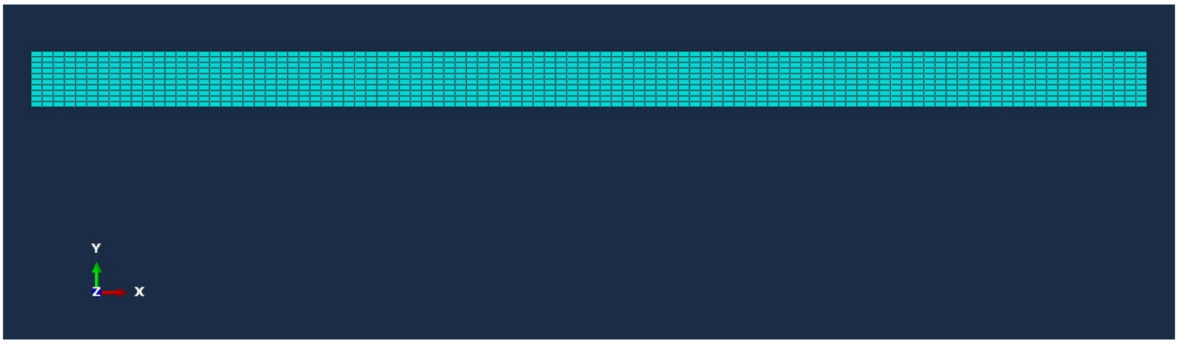

Figure A.1. The first mesh structure.

To solve the convergence problem, the second mesh structure, shown in Figure A.2, with partition in the corners was evaluated. The models which have parts from one to six in the partition sections, from 100 to 200 on top and bottom edges, and from 10 to 30 on the side edges were simulated. Table A.1 shows the difference in results of vertical force and horizontal force. Based on the results given in the table, it is concluded that differences between each case are quite low regarding the vertical and horizontal forces. Therefore, the mesh structure, illustrated in Figure A.3, has 16 parts on side edges, 200 parts on top and bottom edges were considered as the appropriate one because both force responses have difference ratios under 1% so that further refinements were performed in the corners of the rubber model.

Figure A.2. The partition of the second mesh structure.

Table A.1. The results of the mesh convergence study.

Number of Parts on Diagonal Partition	Number of Parts on Side Edges	Number of Parts on Top and Bottom Edges	Shear Step Completed (%)	RF2 (N)	Difference (%)	RF1 (N)	Difference (%)
-	*10*	*100*	*83*	-	-	-	-
1	*10*	*100*	*13*	-	-	-	-
2	10	100	100	-719500	-	45170	-
4	10	100	100	-716300	0.44	45040	0.29
6	10	100	100	-715300	0.14	45040	0.00
6	10	150	100	-692500	3.19	44250	1.75
6	10	200	100	-678300	2.05	43900	0.79
6	**16**	**200**	**100**	**-683900**	**0.83**	**44220**	**0.73**
6	20	200	100	-684700	0.12	44160	0.14
6	*30*	*200*	*84*	-	-	-	-

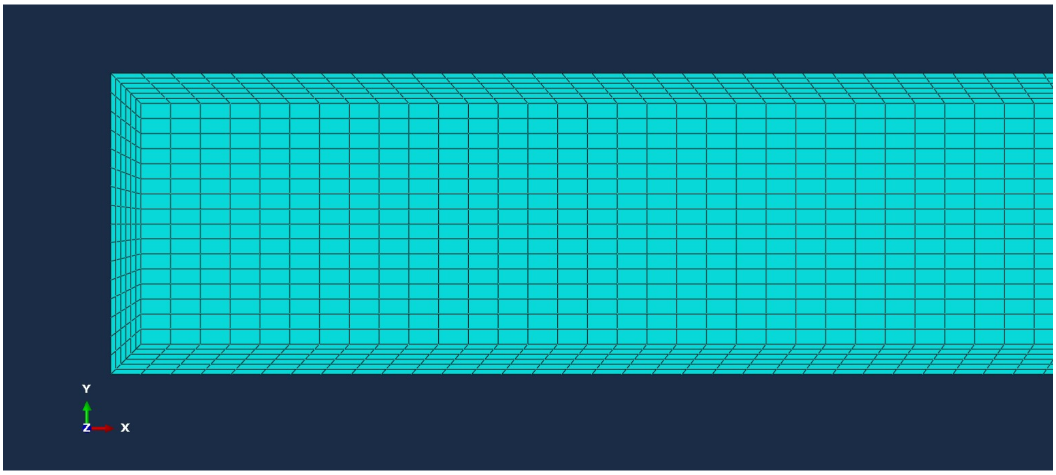

Figure A.3. The mesh design has 16 parts on side edges and 200 parts on top and bottom edges.

In order to construct more refined elements in the corner of the mesh and to construct straight elements along edges of the rubber pad, the third mesh structure with the different partition, shown in Figure A.4, was created. By taking into account the element size (0.156) for side edges of the mesh design shown in Figure A.3, the element size of 0.15 along the side edges and the element size of 0.083 along the partition section of the side edges were constructed. Although the element size on the top and bottom edges of the mesh design shown in Figure A.3 is 0.25, this size was selected as 0.27 in the third design. Figure A.5 shows the structure of mesh for SF=5. There are 6792 elements and 7007 nodes in the final mesh design.

Figure A.4. The partition of the third mesh structure.

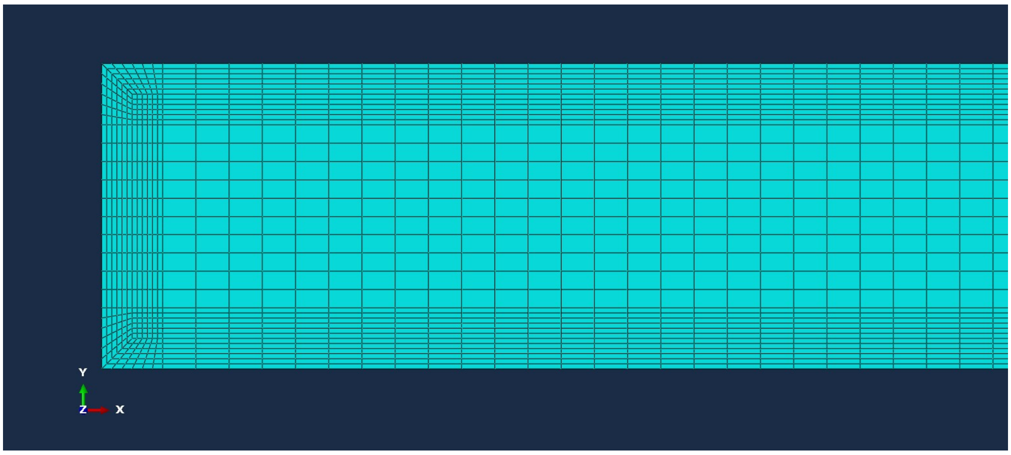

Figure A.5. The structure of mesh for SF=5.

APPENDIX B: MESH CONVERGENCE STUDY FOR STEEL

The steel mesh convergence study was performed for the bearing. The ratio of the bulk modulus to the shear modulus was considered as 2000 for rubber. The combination of compression and shear loads were applied. The compression load was applied as vertical displacement of -0.2007 which corresponds vertical load of 45000 N. Shear load was applied as horizontal displacement of 7.5 which corresponds to $\gamma = 1$. Implicit time integration was used.

The models which have parts from 50 to 100 on top and bottom edges, and from 6 to 10 on the side edges were simulated. Also, the effect of bias was investigated on top and bottom edges. The bias was applied in two directions towards edges. Table B.1 shows the differences in results of maximum Mises stress in steel, maximum and minimum horizontal normal stress at interface with rubber. The interface is called "Interface_2" was described in Section 5.2.2.2.2 of this thesis. Based on the results given in the table, it is concluded that difference ratios for all measures are under 1% for the case of 100 parts on top and bottom edges with bias of 25. The last row of the table indicates that increasing the number of parts on side edges from 6 to 10 affected normal stress values. Therefore, the mesh structure, which has 10 parts on side edges, 100 parts on top and bottom edges were considered. There are 1000 elements and 1111 nodes in the final mesh design. The mesh and the detailed view of the mesh are shown in Figure B.1 and B.2, respectively.

Table B.1. The results of the mesh convergence study.

Number of Parts on Top and Bottom Edges	Bias for Top and Bottom Edges	Number of Parts on Side Edges	Bias for Side Edges	Max. Mises Stress in Steel (MPa)	Diff. (%)	Max. S11 on Interface_2 (MPa)	Diff. (%)	Min. S11 on Interface_2 (MPa)	Diff. (%)
50	50	6	5	300	-	274	-	-149	-
80	50	6	5	291	3.00	280	2.19	-161	8.05
100	50	6	5	287	1.37	281	0.36	-164	1.86
100	25	6	5	286	0.35	282	0.36	-165	0.61
100	25	10	5	285	0.35	282	0	-165	0

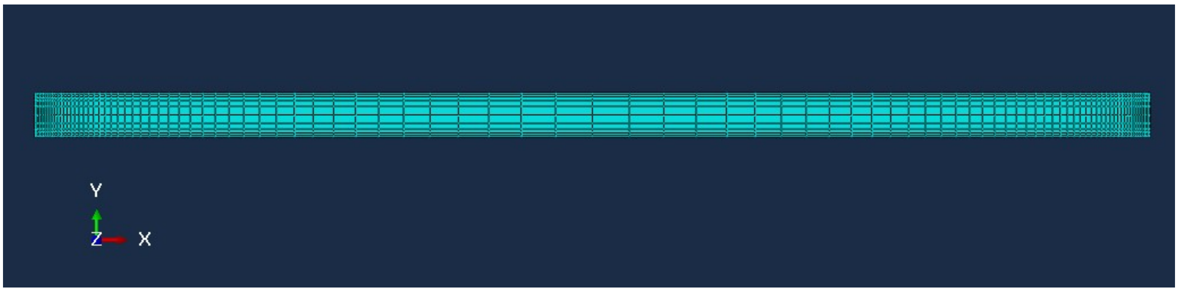

Figure B.1. The structure of mesh for the steel plate.

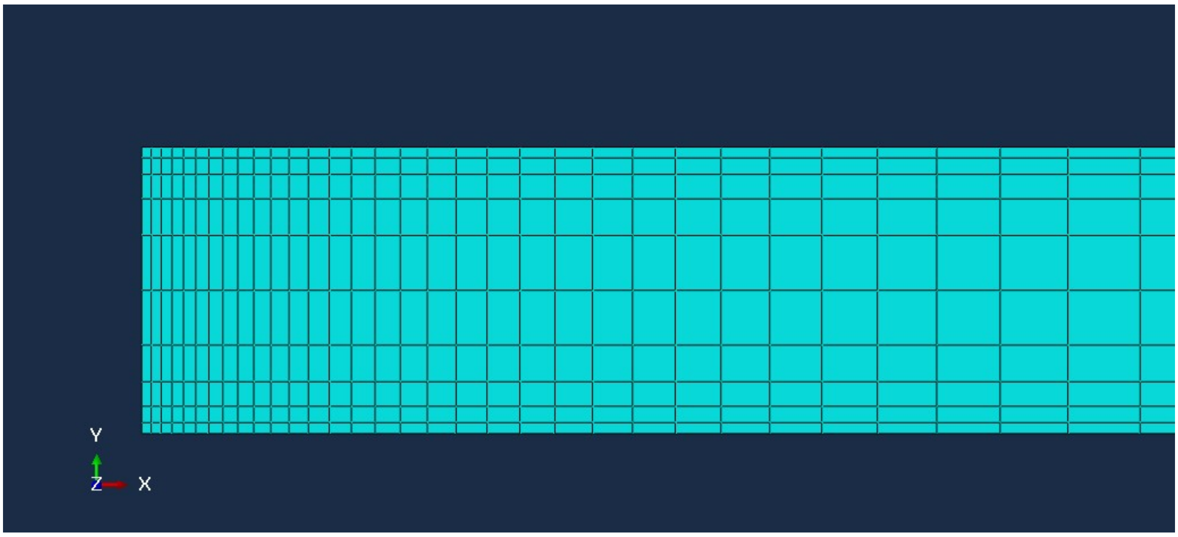

Figure B.2. The detailed view of the mesh.